



Strål
säkerhets
myndigheten

Swedish Radiation Safety Authority

Research

Effect of Neutron Irradiation on the Oxidation and Corrosion of Austenitic Stainless Steels

2022:03

Author: Anders Jenssen ¹⁾, Jiaxin Chen ¹⁾, Olof Tengstrand ¹⁾,
Daniel Jädernäs ¹⁾, Janne Pakarinen ¹⁾, Kristina Lindgren ²⁾,
Mattias Thuvander ²⁾

¹⁾ Studsvik AB, Nyköping

²⁾ Chalmers tekniska högskola, Göteborg

Report number: 2022:03

ISSN: 2000-0456

Available at: www.ssm.se

SSM perspective

Background

Reactor pressure vessel internal components of austenitic stainless steel located close to the core are subject to a high neutron flux. Irradiation by fast neutrons induces changes in the material that affect microstructure, mechanical properties and microchemistry. These changes eventually lead to an increased susceptibility to irradiation assisted stress corrosion cracking (IASCC). Neutron irradiation also affects the water environment through radiolysis, which creates oxidizing species in the water that could affect oxidation and corrosion of the material.

Flux thimble tubes that had been in service in Ringhals 2 have been studied in order to improve the understanding of the corrosion process of reactor pressure vessel core internals and to gain insight regarding the effect of neutron irradiation on the metal oxidation and initiation of irradiation assisted stress corrosion cracking.

Results

The oxides formed on stainless steel exposed in the core region of a PWR consisted of a duplex layer structure, with an outer porous layer of fine spinel grains and an inner dense layer of epitaxially grown spinel. Three dose levels, 0, 50 and 100 dpa, were examined and no significant effect of dose was observed on the oxide microstructure. Small spots were observed in the oxide near the metal oxide interface of the irradiated samples. However, it was not possible to confirm any compositional or structural differences of these features from the surrounding oxide. In addition, the presence of Ni rich metallic particles in the oxide was detected by atom probe tomography.

The Transmission Electron Microscope (TEM) lamellae of all three dose levels had one or two oxide penetrations along metal/metal grain boundaries. There were no differences in size or density of this feature among the dose levels examined, although additional examinations would be needed to verify this statement statistically. However, regions elevated in Ni were observed immediately ahead of the oxide penetrations in the irradiated samples.

Clusters or precipitates rich in Ni-Si, presumably γ' (Ni_3Si), sometimes including Mn, Cu and P, were observed in the metal of the irradiated samples. A lower cluster density was observed at grain boundaries. There was no effect of dose on the cluster size and density. The cluster size observed in this study was in agreement with literature data, while the number density was lower. Bulk silicon content, irradiation parameters such as fluence, flux and temperature, as well as differences in data evaluation are factors that can contribute to the differences observed.

The microstructure of the irradiated metal was consistent with observations reported in the open literature. Radiation induced segregation with depletion of Cr and enrichment of Ni and Si was observed in the irradiated conditions.

Cavities were observed in the irradiated samples. The number density of this feature in the sample at 50 dpa agreed with the range reported in the literature, whereas the density at 100 dpa clearly was higher. Additional examinations are suggested to confirm the observation and to determine if any dimensional changes have occurred.

Relevance

By studying flux thimble tubes irradiated for up to 34 years in Ringhals 2, valuable insight has been gained regarding the effects of neutron irradiation to very high doses on the microstructure and oxidation of austenitic stainless steel in pressurized water reactors.

Need for further research

To confirm some of the results of this study over the full range of dose, and to determine if they are general and not isolated observations, the author has identified a few areas for further study.

Project information

Contact person SSM: Elena Calota

Reference: SSM2015-4280 / 2070006-19



Strål
säkerhets
myndigheten

Swedish Radiation Safety Authority

Authors: Anders Jenssen ¹⁾, Jiaxin Chen ¹⁾, Olof Tengstrand ¹⁾, Daniel Jädernäs ¹⁾,
Janne Pakarinen ¹⁾, Kristina Lindgren ²⁾, Mattias Thuvander ²⁾

¹⁾ Studsvik AB, Nyköping

²⁾ Chalmers tekniska högskola, Göteborg

2022:03

Effect of Neutron Irradiation on the Oxidation and Corrosion of Austenitic Stainless Steels

Date: February 2022 (updated in May 2022)

Report number: 2022:03 ISSN: 2000-0456

Available at www.stralsakerhetsmyndigheten.se

This report concerns a study which has been conducted for the Swedish Radiation Safety Authority, SSM. The conclusions and viewpoints presented in the report are those of the author/authors and do not necessarily coincide with those of the SSM.

Sammanfattning

Prov för analys med transmissionselektronmikroskopi (TEM) och atomsond (APT) bereddes från rostfria (Type 316) höljerör till härdinstrumenteringen i en tryckvattenreaktor (PWR), så kallade flux thimble tubes (FTT). Doserna 0, 50 och 100 dpa (displacements per atom) studerades. Undersökning av oxidfilmen som bildats efter flera decenniers exponering i reaktormiljö visade inte på någon signifikant effekt av neutronbestrålning på oxidationen av metallen. För alla tre dosnivåer observerades lokal oxidation av korngränser (oxidpenetration) till ett djup om någon μm . Ingen skillnad i storlek eller förekomst av dessa noterades bland de olika doserna som undersöktes, vilket visar att neutronbestrålningen har ingen eller liten inverkan på bildningen och tillväxten av oxidpenetrationerna. I de bestrålade proven observerade emellertid områden med förhöjd Ni-halt omedelbart framför oxidpenetrationerna.

Mikrostrukturen hos det bestrålade rostfria stålet var i överensstämmelse med observationer rapporterade i den öppna litteraturen gällande liknade material och bestrålning. Bestrålningsinducerad segring med korngränsutarmning av Cr och anrikning av Ni och Si noterades i de bestrålade tillstånden. Vidare förekom lokal ansamling eller utskiljningar med hög halt av Ni-Si, förmodligen γ' (Ni_3Si), ibland inkluderande Mn, Cu och P, i metallen hos de bestrålade proven. Förekomsten av Ni-Si-ansamlingarna var lägre vid korngränserna och deras storlek och antal verkar inte ha påverkats av dos för de två doser som undersöktes (50 och 100 dpa).

Kaviteter observerades i det rostfria stålet hos de två bestrålade tillstånden. I provet med dosen 50 dpa var antalstätheten inom spridningen som redovisas i den öppna litteraturen, medan den vid 100 dpa var klart högre. Det rekommenderas att ytterligare undersökningar utförs för att bekräfta observationen och för att avgöra om några dimensionsförändringar skett.

Abstract

Samples for examination by TEM (discs and lamellae) and analysis by APT were prepared from flux thimble tubes at 0, 50 and 100 dpa. Examination of the oxide films showed that there was no significant effect of neutron irradiation on the oxidation behavior. All three dose levels had oxide penetrations along grain boundaries. There were no differences in size or density of this feature among the dose levels examined, which shows that irradiation has no or little effect in the formation and growth of the oxide penetrations. However, regions elevated in Ni were observed immediately ahead of the oxide penetrations in the irradiated samples.

The microstructure of the irradiated metal was consistent with observations reported in the open literature. Radiation induced segregation with grain boundary depletion of Cr and enrichment of Ni and Si was observed in the irradiated conditions. Clusters or precipitates rich in Ni-Si, presumably γ' (Ni_3Si), sometimes including Mn, Cu and P, were observed in the metal of the irradiated samples. A lower cluster density was observed at grain boundaries. There appeared to be no effect of dose on the cluster size and density.

Cavities were observed in the irradiated samples. The number density of this feature in the sample at 50 dpa agreed with the range reported in the literature, whereas the density at 100 dpa clearly was higher. Additional examinations are suggested to confirm the observation and to determine if any dimensional changes have occurred.

List of contents

1. Introduction	4
1.1. Background.....	4
1.2. Objectives.....	7
2. Materials Examined	8
2.1. Flux Thimble Tubes from Ringhals 2.....	8
2.2. Materials.....	9
2.3. Neutron Doses.....	9
3. Preparation of Samples	12
3.1. Rough Cutting.....	12
3.1.1. FTT in Core Position G7 at 0 dpa.....	12
3.1.2. FTT in Core Position L9 at ~50 dpa.....	13
3.1.3. FTT in Core Position L9 at ~100 dpa.....	13
3.2. Preparation of TEM Lamellae.....	14
3.3. Preparation of TEM Discs.....	17
3.4. Preparation of APT Samples.....	18
4. TEM Examination of Oxide Films	20
4.1. Experimental Information.....	20
4.2. Oxide Film Surface Morphology.....	20
4.3. Elemental Compositions and Crystal Structures of the Oxide Films	
.....	20
4.3.1. Sample at 0 dpa.....	20
4.3.2. Sample at 50 dpa.....	25
4.3.3. Sample at 100 dpa.....	31
5. TEM examinations of Bulk Material	38
5.1. Experimental Information.....	38
5.2. Microstructure - General.....	39
5.3. Radiation Induced Segregation.....	40
5.4. Precipitates.....	42
5.5. Cavities.....	43
5.6. Frank Loops.....	45
6. APT Analyses	47
6.1. Experimental Information.....	47
6.2. APT Results.....	47
6.2.1. Bulk.....	47
6.2.2. Grain Boundaries.....	50
6.2.3. Oxides.....	51
7. Discussion	55
7.1. Recommendations for Further Studies.....	59
8. Conclusions	60
9. References	61
Appendix A – APT Analyses of Grain Boundaries in Material at 100 dpa	
.....	1

1. Introduction

1.1. Background

Reactor pressure vessel (RPV) internal components of austenitic stainless steel located close to the core are subjected to a high neutron flux. Irradiation by fast neutrons induces changes in the material that affect microstructure, mechanical properties and micro-chemistry [e.g., 1, 2], changes that eventually lead to an increased susceptibility to stress corrosion cracking (SCC) [3, 4]. Since irradiation enhances the propensity for cracking, failures in neutron irradiated stainless steel is termed irradiation assisted stress corrosion cracking (IASCC). Neutron irradiation also affects the water environment through radiolysis [e.g. 5], which creates oxidizing species in the water that could impact oxidation and corrosion of the material.

Service failures caused by IASCC have occurred in RPV internals in boiling water reactors (BWR) as well as pressurized water reactors (PWR). Similar to conventional intergranular stress corrosion cracking (IGSCC), IASCC appears as intergranular cracks, although thermal sensitization of the grain boundaries, caused by chromium carbide precipitation, is not required for the material to become susceptible to cracking.

Although IASCC has been studied quite extensively over the past 20 years, full understanding of the mechanism controlling the phenomenon has not been established [e.g., 6]. Much of the research conducted so far has been focused on determining the effects of material factors (neutron dose, radiation hardening, various grades of steel, alloy purity, pre-irradiation processing such as cold work, etc.), water chemistry (corrosion potential, temperature, etc.), and mechanical factors (stress intensity, “threshold stress” for crack initiation, etc.) on IASCC. Radiation induced segregation (RIS) and its effect on the redistribution of alloying and impurity elements at grain boundaries has been studied quite extensively [e.g., 1, 2, 7], and models exist to explain the phenomenon [e.g., 2 and references therein]. However, only limited studies have focused on the effects of radiation (RIS, hardening, enhanced diffusivity, etc.) on the oxides formed on grain boundaries, the surface oxides and the metal/oxide interface, in particular in stainless steels at high dose, irradiated under conditions relevant to light water reactors (LWRs). For instance, studies on the oxides formed at grain boundaries of failed LWR core internal components have been performed, but these studies mainly focused on the crack tip region [8]. Irradiation induced changes affecting the grain boundary oxidation, and consequently the passive film formed on stainless steel, can be important for the initiation of IASCC.

Irradiation has been shown to accelerate corrosion of stainless steels, at least in the short-term perspective (days). Oxidation experiments performed under simultaneous proton irradiation [9-11], and exposure of pre-irradiated (protons) Type 316L coupons to PWR primary coolant [12], indicate that the oxidation kinetics are enhanced by irradiation. Raiman et al. [9] exposed samples of Type 316L in 320 °C water with 3 ppm H₂, where two samples were irradiated with protons and one was exposed outside of the proton beam. The exposures and irradiation lasted for 24 hours. An increase in water conductivity was observed during irradiation, indicating accelerated corrosion. Examination in a STEM (scanning transmission electron microscope) of oxide cross-sections prepared from the various samples showed that the passive inner layer of the

irradiated surfaces was thinner compared to unirradiated surfaces. TEM (transmission electron microscope) examination revealed that the irradiated oxides had a more porous morphology, and compositional analysis showed a significant decrease in the chromium content of the irradiated inner oxides compared to the unirradiated samples.

The enhanced corrosion kinetics observed on pre-irradiated Type 316L exposed to PWR coolant [12] indicate the microstructural changes induced by irradiation impacts corrosion. This agrees with observations made in post-test examinations of O-ring specimens (3 to 76 dpa) exposed to simulated PWR coolant [13]. These examinations showed that the inner oxide layer thickness and grain boundary oxidation depth increased with dose, suggesting oxidation is enhanced by irradiation. It was also noted that the basic oxidation process appeared to be unchanged by irradiation.

Shoji reported on results from stressed samples of Type 316L irradiated in the Halden reactor for up to 2568 hours [14]. The irradiation was carried out at 288 °C in water with 2 ppm of oxygen. It was found that localized oxidation was more pronounced under neutron irradiation; see Figure 1. In addition, the localized oxidation depth increased with time, in particular under irradiation. Figure 1 also shows that the surface state of the metal is important, as the localized oxidation depth was larger in samples with lathed surfaces compared to polished.

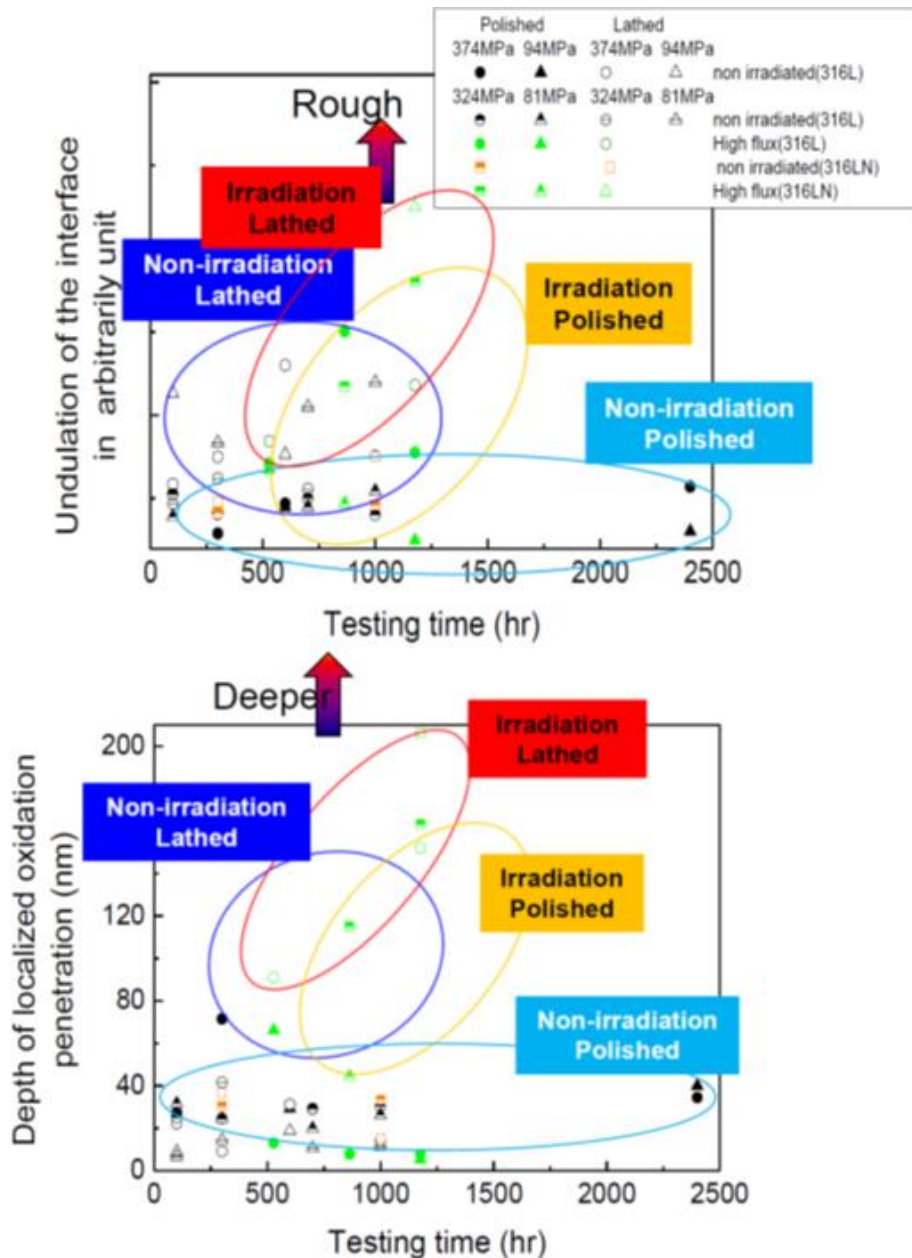


Figure 1 Localized oxidation depth and metal/oxide interface undulation of stressed samples of Type 316L exposed to 288 °C water with 2 ppm of oxygen with and without neutron irradiation [14].

Radiolysis products, such as hydrogen peroxide, may affect the processes involved in the oxide formation, and given the composition of the grain boundaries being different from the bulk metal, different oxidation rates are possible. Results indicate that hydrogen peroxide increased the corrosion rate (over oxygen) by the formation of a defect structure that increased ionic mass transport through the oxide film [15]. Other research has shown that the oxide film formed on stainless steel in the presence of hydrogen peroxide is more conducting [16]. Several short-lived radicals are also produced by radiolysis, and they may affect the oxides formed. In addition to radiolysis, corrosion may be accelerated due to enhanced diffusion caused by the elevated irradiation induced point defect concentration.

Based on the observations discussed in this section, it appears neutron irradiation, in comparison with exposure to light water reactor environment without irradiation, accelerates corrosion, produces a thinner inner oxide layer, and enhances localized oxidation in stainless steel. Furthermore, the state of the substrate, where the grain boundary composition may be different from the surface, also contributes to the character of the oxide film formed. These effects might have an impact on the initiation of IASCC. Examination by high-resolution techniques of the grain boundaries immediately below the oxidized metal surface and the oxide/metal interface of highly irradiated stainless steel from retired PWR components can provide further insight into the corrosion processes involved. This report presents and discusses the results of transmission electron microscope (TEM), and atom probe tomography (APT), examinations of samples taken from flux thimble tubes irradiated for up to 34 years in Ringhals 2.

1.2. Objectives

The objectives of the study were to improve the understanding of the corrosion process of RPV core internals, and to gain insight regarding the effect of neutron irradiation on the metal oxidation and initiation of IASCC.

2. Materials Examined

2.1. Flux Thimble Tubes from Ringhals 2

The samples examined in this study were obtained from two different bottom mounted flux thimble tubes (FTT). A flux thimble tube is a guide tube for neutron flux monitoring. While in service, the FTT extended from the top of the core to the outside of the RPV through a penetration in the RPV bottom head. FTTs are sealed by a stainless steel plug (a.k.a. bullet nose) at the end located at the top of the core. Consequently, the inside of the FTTs was dry, and the tubes served as the pressure boundary between the reactor pressure and the containment atmosphere.

Both FTTs were in service in Ringhals 2, a pressurized water reactor (PWR) of Westinghouse design that started commercial operation in 1975. While in service, the two FTTs used in this study were placed in core positions G7 and L9; see Figure 2. The FTTs were in service from the first start-up of the reactor until 2004 (core position G7) and 2009 (core position L9), i.e, for 29 and 34 years, or 168,184 and 205,891 EFPH (effective full power hours), respectively.

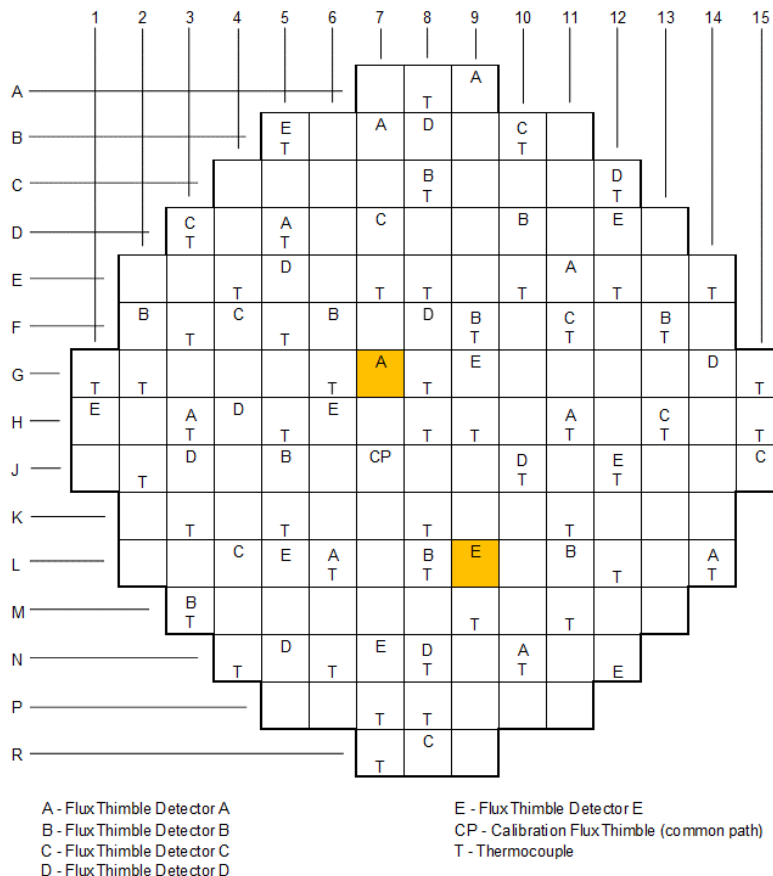


Figure 2
Core positions of the FTTs tested in this study.

Since the component extended from below the core to the top of the core, there are fluence gradients in the parts of the tubes corresponding to the core inlet and outlet. In addition, the irradiation temperature increased from approximately 287 °C at the core inlet to approximately 325 °C at the outlet.

2.2. Materials

The flux thimble tubes were made of cold drawn Type 316 stainless steel (SS). During the final stage of manufacture the wall thickness of the solution annealed tube was reduced by approximately 15%. Nominal inner and outer diameters of the tubes were 5.1 mm and 7.62, respectively.

Two different heats of material were used to manufacture the FTTs that went into service at the first start-up of Ringhals 2. No records have been found on which heat was used for a specific FTT. However, one of the heats was used to manufacture a majority of the FTTs that went into service at the first start-up. The chemical composition of one of the heats used is shown in Table 1.

Table 1

Chemical composition (wt.-%) of one of the heats used for the fabrication of FTTs.

C	Si	Mn	P	S	Cr	Ni	Mo	Co	V	Ti	Al	Sn	N
0.045	0.43	1.70	0.026	0.010	17.4	13.3	2.69	0.040	0.019	<0.005	0.008	<0.005	0.044

The process specifications for the fabrication of FTTs require that the final yield strength be between 483 and 621 MPa [17].

Tensile testing and hardness measurements of the materials in the irradiated condition were performed in previous studies. Data on the FTT in core position G7 are available in [18], whereas results from testing of the FTT in core position L9 were reported in [19].

2.3. Neutron Doses

Gamma scanning of the FTTs was performed with a Ge detector provided with a 0.5 mm collimator. Gamma spectra were obtained and analyzed at equidistant (2 mm for the FTT placed in position G7 and 0.25 mm for the FTT in position L9) positions along the FTT segments. These measurements yielded the relative axial activity distributions of Co-58, Co-60 and Mn-54 in the FTT. These nuclides arise from different neutron reactions with cross sections, σ_n , peaking at different parts of the neutron spectrum. Mn-54 and Co-58 are basically formed by fast neutron reactions, while Co-60 both arises from thermal (Co-59) and fast neutrons (Ni-60). The formation of Co-60 by thermal neutron reactions will dominate.

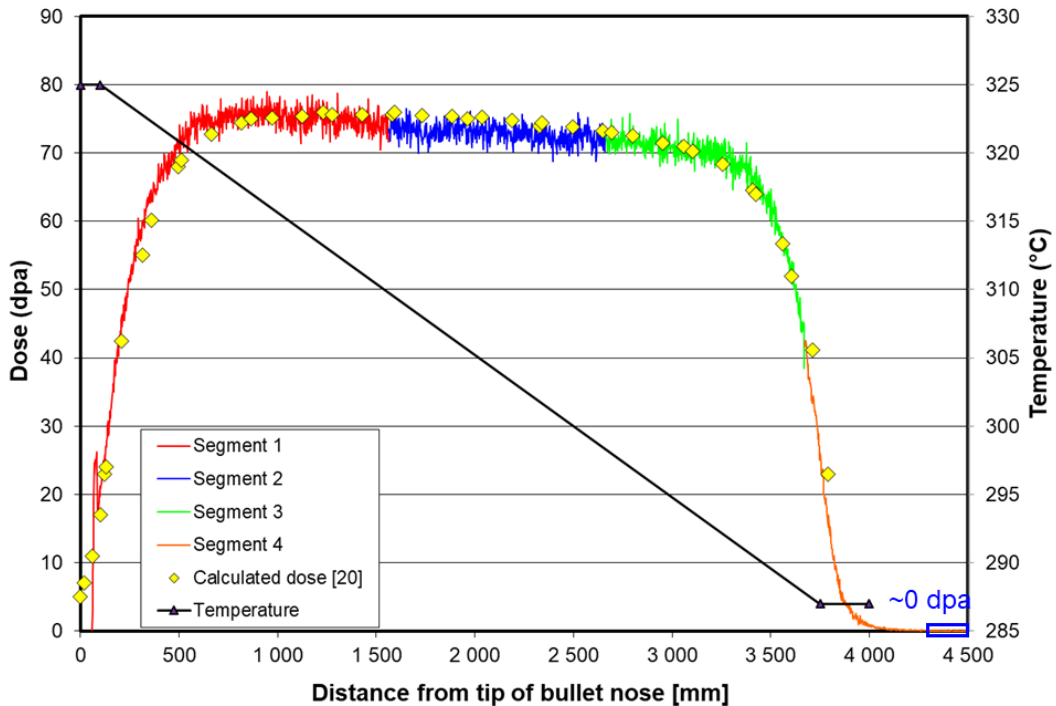


Figure 3

Dose profile based on Mn-54 activity and calculated data [20] in the FTT located in core position G7. The graph also shows the approximate coolant temperature in the axial direction of the tube. The portion of the tube used for the specimens machined for this study is indicated in the graph.

Graphs on the neutron dose as a function of the distance from the bullet nose are presented in Figure 3 and Figure 4. The data in these graphs are based on the Mn-54 activity measurements, since this nuclide reflects the fast neutron flux at the FTTs. The highest Mn-54 activity level for each FTT was assigned a dose of 76 dpa for the FTT located in core position G7, and 100 dpa for the FTT located in core position L9. Dose data at other locations of the FTTs were interpolated based on the Mn-54 activity profiles. Figure 3 also includes calculated doses for the FTT located in core position G7 [19], and these data are in excellent agreement with the dose data estimated by the Mn-54 activity measurements.

The dose profiles in Figure 3 and Figure 4 show that there are steep gradients at the locations corresponding to the core inlet and outlet, whereas the dose profile is relatively flat in the core region, with the dose peaking at approximately 800 to 900 mm from the tip of the bullet nose. Also shown in these figures is the coolant temperature, which increases essentially linearly from about 287 °C at the core inlet to 325 °C at the core outlet [21].

Figure 3 and Figure 4 indicate the locations in the FTTs of the tube sections that were used for preparing the samples examined in this study. Unirradiated material was taken from a section of the FTT with a peak dose of 76 dpa (core position G7) that was located below the lower core plate. Because the FTT with a peak dose of 100 dpa was cut above the lower core plate, no “unirradiated” material was available from that component. Material from three locations, at doses of about 50, 75 and 100 dpa, were taken from this FTT; see Figure 5.

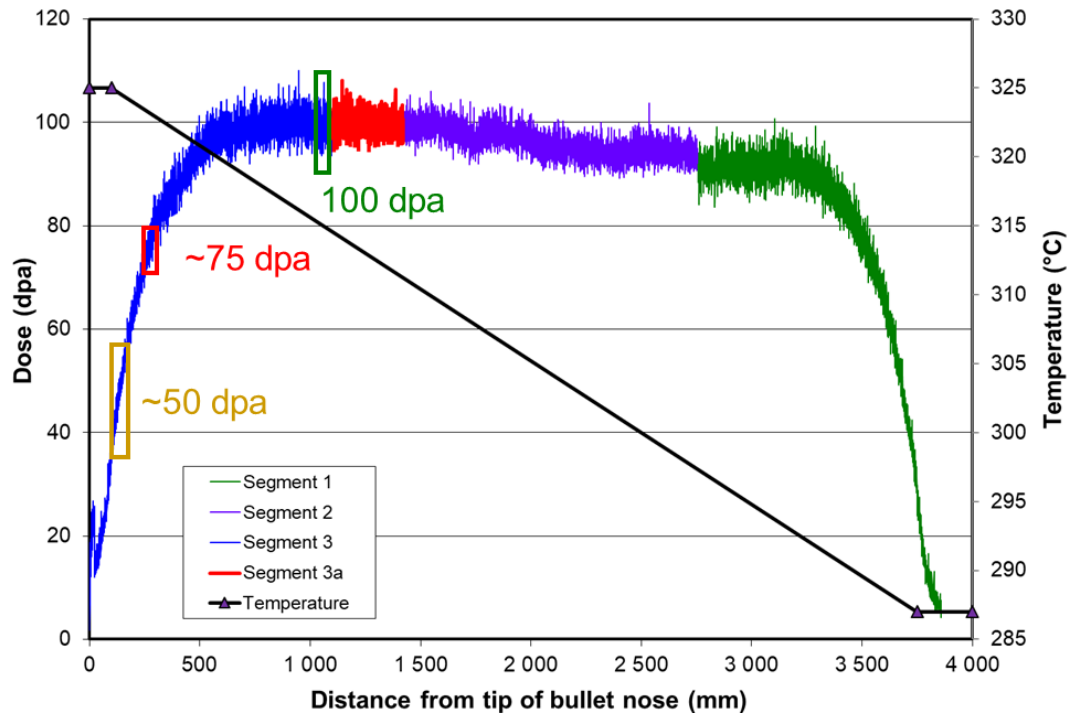


Figure 4
 Dose profile based on Mn-54 activity in the FTT located in core position L9. The graph also shows the approximate coolant temperature in the axial direction of the tube. The portions of the tube used for the specimens machined for this study are indicated in the graph.

3. Preparation of Samples

The preparation of samples for this study as well as a project run by EPRI is described in detail in [22]. A summary regarding the preparation of samples examined in this study is provided in this section.

3.1. Rough Cutting

Tube sections from the locations indicated in Figure 3 and Figure 4 were cut from each FTT using a diamond wheel cutter. Cutting plans were prepared for each tube section according to the number and dimensions of the specimens to be extracted from the designated dose level. When the blanks were cut, approximately 0.5 mm of material was lost as saw dust, which was accounted for by adding 0.5 mm per cut to the total length of tube segment needed for the number and types of blanks in question. Based on the cutting plans, blanks for specimens, in the form of rings, were prepared using a diamond wheel cutter. The reference point in these cutting plans was always the uppermost point of the component with respect to the core. Markings on tube segments and blanks were always made to indicate “up” with respect to the core.

3.1.1. FTT in Core Position G7 at 0 dpa

The cutting plan for the samples examined in this study that were taken from the FTT located in core position G7 and a dose of 0 dpa is presented in Figure 5. Cutting of blanks was made from right to left, i.e. from the end closest to the bullet nose, so excess material ended up in the “spare piece”. The cut on the right-hand side of Figure 5, and the cut separating the 77 mm long segment from the one with a length of ~128 mm, were made at the hot cell laboratory, whereas all other cuts were performed at the active metals laboratory. Due to the limited size of the cavity of the transportation flask used to transfer material between labs, the tube segment shown in Figure 5 was cut into two pieces with lengths 128 and 77 mm.

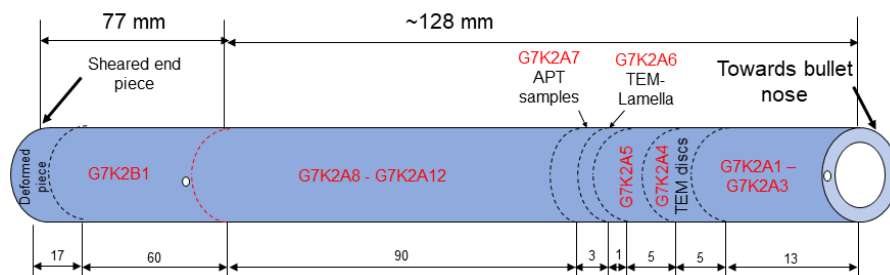


Figure 5

Cutting plan for blanks taken from the FTT located in core position G7 and a dose of 0 dpa. Not to scale.

A short description concerning what type of specimen (TEM-disc, TEM lamellae, or APT samples) each blank was intended for is provided in Figure 5. It is noted that all samples for this study were extracted from about the same region of the FTT.

3.1.2. FTT in Core Position L9 at ~50 dpa

The cutting plan for the FTT located in core position L9 and a dose of 50 dpa is presented in Figure 6. This section of the FTT had a steep gradient in dose, ranging from ~36 to ~58 dpa (Figure 6). Cutting of blanks was made from left to right in Figure 6. The TEM lamellae were taken from the end of Blank 10-FTT-D3A5 that was located closest to the bullet nose, and where the dose was about 51 dpa. APT samples and TEM discs were taken from locations where the dose was about 49 dpa and 45, respectively.

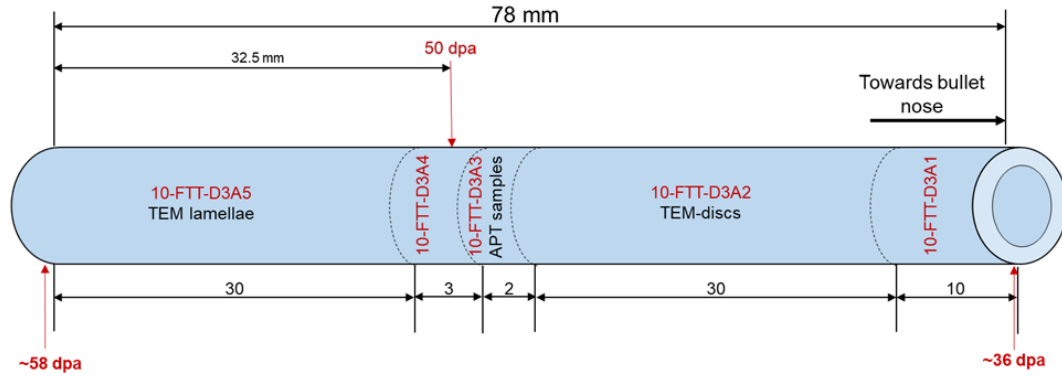


Figure 6

Cutting plan for blanks taken from the FTT located in core position L9 and a dose of 50 dpa. Not to scale.

3.1.3. FTT in Core Position L9 at ~100 dpa

The cutting plan for the FTT located in core position L9 and a dose of 100 dpa is presented in Figure 7. There was no gradient in dose in this section of the FTT. Cutting of blanks was made from right to left in Figure 7.

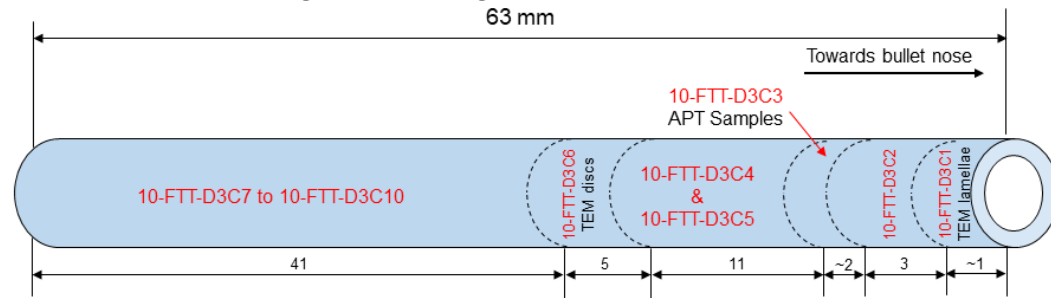


Figure 7

Cutting plan for blanks taken from the FTT located in core position L9 and a dose of 100 dpa. Not to scale.

3.2. Preparation of TEM Lamellae

Ring-shaped blanks, containing the oxide film formed in contact with reactor water during operation, were in all cases but one used for preparation of TEM-lamellae by focused ion beam (FIB) milling. To reduce the dose to personnel while producing the TEM-lamellae, a sample of each blank was cut and transferred to the microscope, see Figure 8. The sample at 50 dpa was prepared from the head of a discarded tensile specimen (Figure 9). The lamellae contained the oxide film, the oxide-metal interface and the base metal. Typically, the lamellae were 20 μm wide and 10 μm in height.



Figure 8

Ring shaped blank (10-FTT-D3C1) at 100 dpa after removal of sample for preparation of TEM lamellae (a), and sample removed from blank, including measured dose rates (b).

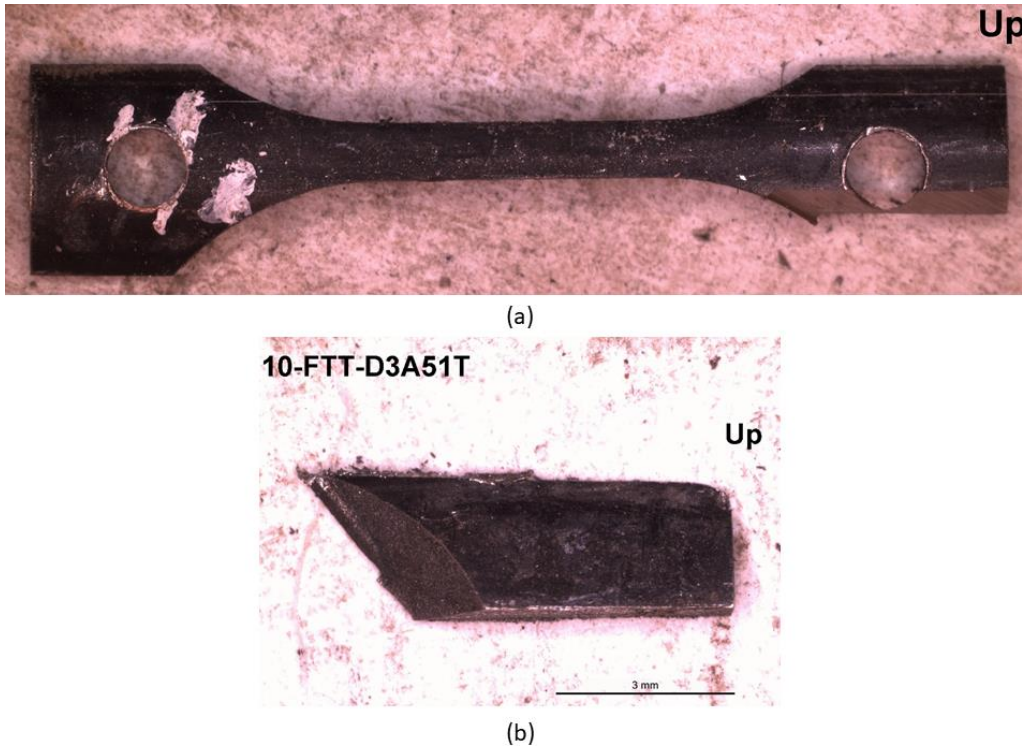


Figure 9

Discarded tensile specimen after cutting of sample for extraction of TEM-lamellae (a). Sample 10-FTT-D3A51T for extraction of TEM-lamella (b).

The equipment used for preparing the TEM-lamellae was a field emission gun (FEG) SEM (Zeiss Auriga Cross Beam) equipped with a focused ion beam (FIB) source, platinum deposition nozzle and micro manipulators.

A representative area of the sample that contained a grain boundary oxidized to a depth of 1-2 μm was chosen. A rectangular shaped strip of Pt was deposited over the chosen area and the surrounding material milled away, leaving a thin slice (lamella) of material which could be transferred to a TEM-grid. Following transfer of the lamellae to the TEM grid, they were thinned further by gentle ion beam milling to a thickness transparent for the electron beam used in a TEM. Information about the TEM lamellae prepared is summarized in Table 2, and images are presented in Figure 10 through Figure 12.

Table 2

TEM lamellae prepared from three different dose levels.

FTT	Lamella id.	Dose (dpa)	Irradiation temp. ($^{\circ}\text{C}$)
Core position G7	G7K2A6	0	287
Core position L9	10-FTT-D3A51T	51	324
Core position L9	10-FTT-D3C1	100	315

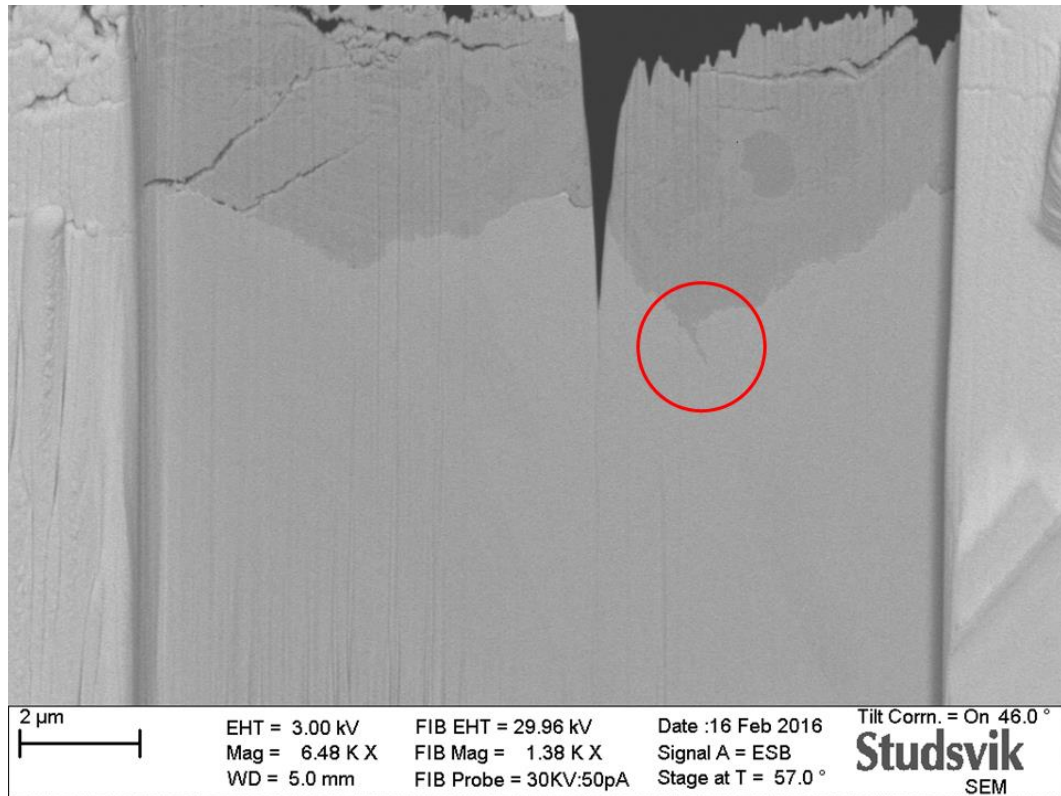


Figure 10

SEM image of the TEM lamella prepared from Blank G7K2A6 at 0 dpa before final thinning. Note the oxidized grain boundary (encircled) with a penetration depth of 0.7 μm .

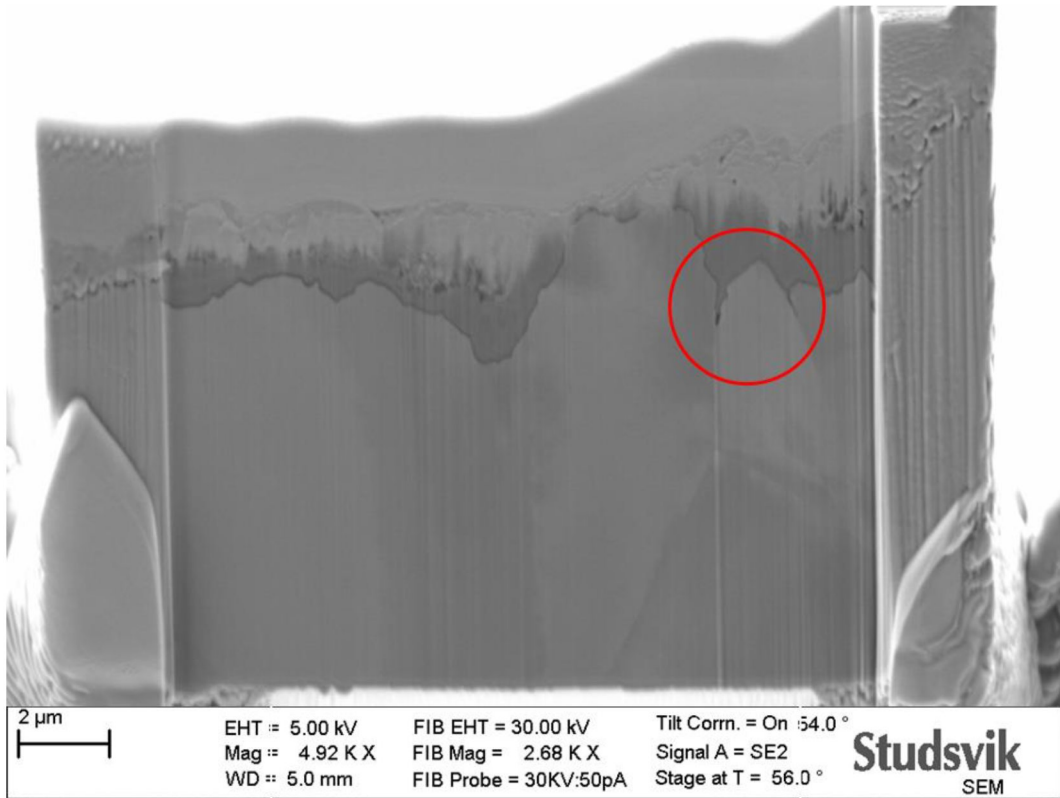


Figure 11

SEM image of the TEM lamella prepared from Blank 10-FTT-D3A51T at 51 dpa before final thinning. Note the oxidized grain boundaries (encircled) with penetration depths of 0.6 mm (right) and 0.9 mm (left).

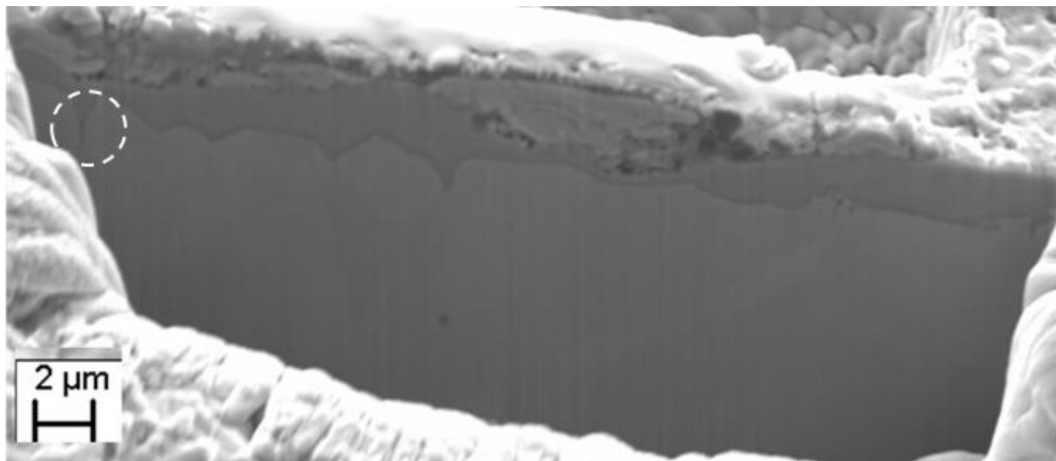


Figure 12

SEM image of the TEM lamella prepared from Blank 10-FTT-D3C1 at 100 dpa before thinning to electron transparency. Note the oxidized grain boundary (encircled) with a penetration depth of 0.8 mm.

3.3. Preparation of TEM Discs

Ring-shaped blanks were cut into smaller segments by a diamond wheel cutter. These segments were embedded in wax and then ground into rectangles which finally were polished in steps, finishing with 9 followed by 3 μm diamond suspensions. The final thickness was nominally 0.2 mm, but in most cases, it was somewhat less. The wax was removed by gentle heating and dissolution in acetone. From the polished rectangles, circular TEM-discs were punched out. Standard 3 mm diameter TEM discs were punched from the unirradiated material, while 1 mm diameter discs were punched from the irradiated material conditions to minimize gamma radiation from the sample, which otherwise could interfere with the TEM examination. The 3 mm discs were then thinned to electron transparency using electrolyte polishing. Photographs showing the segments cut from the ring-shaped blanks, the rectangular-shaped blanks following grinding and polishing, and punched out 3 mm TEM discs are presented in Figure 13.

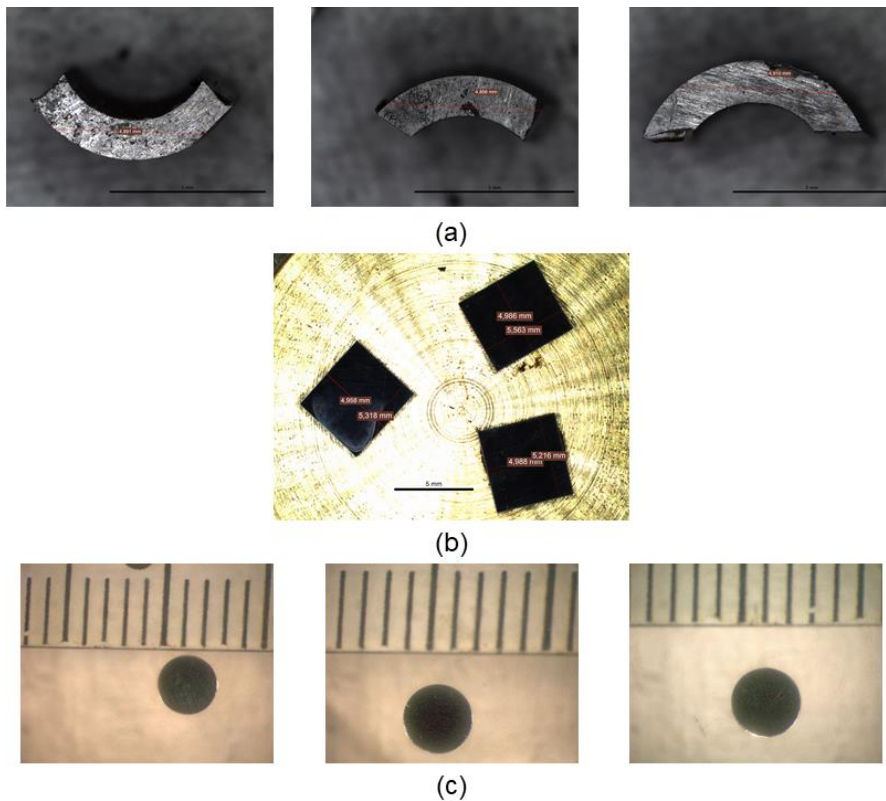


Figure 13

Sequence in the preparation of Ø 3 mm TEM discs. Sectioning of a ring-shaped blank into three pieces (a), rectangular-shaped blanks after grinding and polishing (b), finalized Ø3 mm TEM-discs discs after punching (c).

Following punching of 1 mm discs from the polished rectangles, the disc was glued with Loctite™ to a 3 mm diameter sample holder of unirradiated Type 316 SS; see Figure 14. As shown in this figure, the holder was provided with a 0.8 mm diameter hole at the center, and a 2 mm diameter recess. The recess was then filled with silver glue, and when it was dry, the entire surface was covered with Lacomite. When the Lacomite had solidified, it was mechanically removed from the irradiated 1 mm disc, so that only the irradiated portion of the composite sample was thinned during electropolishing.

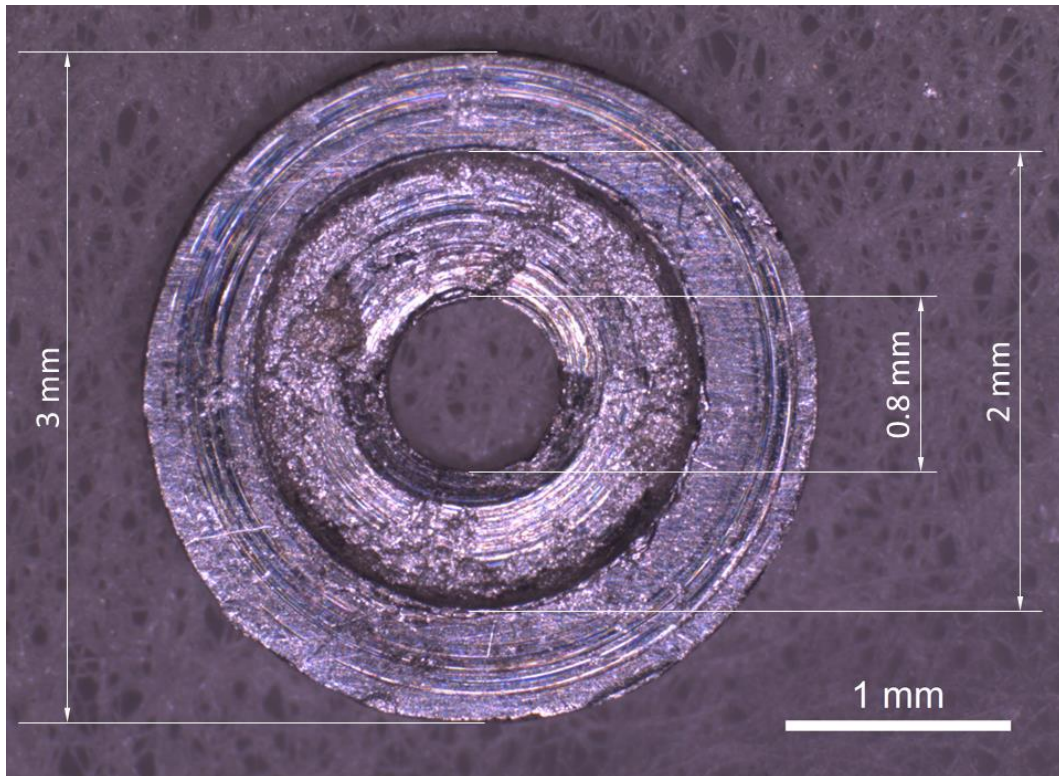


Figure 14
Photograph of a sample holder for 1 mm diameter TEM discs.

Information about the TEM discs prepared from the various dose levels is summarized in Table 3.

Table 3
TEM discs prepared from three different dose levels.

FTT	Lamella id.	Dose (dpa)	Irradiation temp. (°C)
Core position G7	G7K2A4	0	287
Core position L9	10-FTT-D3A1	45	324
Core position L9	10-FTT-D3C6	100	315

3.4. Preparation of APT Samples

APT samples were prepared in a fashion similar to the preparation of TEM lamellae; see Section 3.2. Polished cross-sections that included the oxide formed during exposure in Ringhals 2 were used for all three dose levels to prepare samples. An area of interest that included the oxide, the underlying metal, and an oxidized grain boundary was covered by a protective strip of Pt in the field emission gun FIB/SEM. The strip measured a few μm in cross-section and a few tens of μm in length. Subsequently, material adjacent to the strip was milled away using the FIB, and the Pt strip including the material of interest was welded to a micromanipulator tip. The strip was then cut in triangular prism-shaped slices that were attached to micro-posts on a Si-wafer substrate for APT analysis. About five specimens were produced from each strip. Immediately before the APT analysis, the specimens were sharpened into needles with tip radii around 50 nm.

As indicated in the previous paragraph, attempts were made to include oxidized grain boundaries and the oxide/metal interface in the sampling. Because of the small sample size and the difficulty in correctly positioning the samples, it was not possible to cover all desired regions for each dose level. Table 4 indicates what regions were captured for the three dose levels examined.

The various steps involved in the preparation of APT samples are illustrated in Figure 15. Information about the APT samples prepared from the various dose levels is summarized in Table 4.

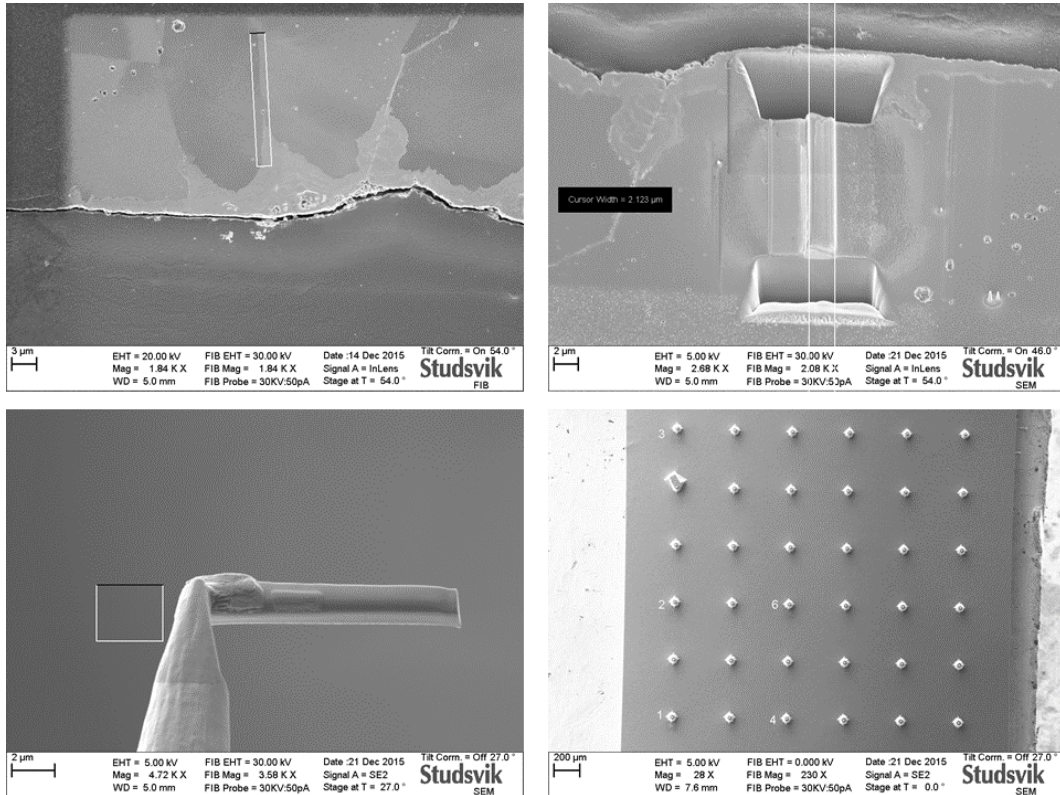


Figure 15
Illustration showing the preparation of APT samples.

Table 4
APT samples prepared from three different dose levels.

FTT	Lamella id.	Dose (dpa)	Irradiation temp. (°C)
Core position G7	G7K2A7	0 ¹⁾	287
Core position L9	10-FTT-D3A3	49 ²⁾	324
Core position L9	10-FTT-D3C3	100 ³⁾	315

- 1) The samples examined covered the metal matrix, oxide and metal/oxide interface
- 2) The samples examined covered the metal matrix, oxide and metal/oxide interface
- 3) The samples examined covered the metal matrix, grain boundaries in the metal, oxide and metal/oxide interface

4. TEM Examination of Oxide Films

4.1. Experimental Information

A field emission type TEM (JEOL, model JEM 2100F) was used to examine the microstructure of the oxide film. Operated at 200 kV, the microscope was equipped with detectors for Energy Dispersive X-ray Spectroscopy (EDS) (Oxford Instruments – X-Max^N 80 TLE), Electron Energy-Loss Spectroscopy (EELS), and bright and dark field scanning transmission electron microscopy that allowed compositional analysis and imaging. A combined analysis with Selected Area Electron Diffraction (SAED) and EDS was performed to identify phase compositions of some selected oxide grains, or some regions of interest with typical compositions.

4.2. Oxide Film Surface Morphology

SEM images of the corroded surfaces and cross sections of the oxide films on the three dose levels examined are shown in Figure 16, Figure 23 and Figure 34. Generally, at all three dose levels the oxide films had a duplex layer structure. The outer layer was relatively porous, and it contained cracks. The fine grains on the outer layer surfaces gave an impression that the corroded surfaces were smooth. During thinning of the TEM-lamellae only a small fraction of the outer layer could be preserved for TEM analysis. The inner layer, on the other hand, looked uneven in thickness but dense. The total oxide film (inner + outer oxide) thicknesses ranged from approximately ~2 to ~4 μm . At some intersections between metal/metal grain boundaries and the inner oxide, sharp oxide penetrations along the metal/metal grain boundaries can be observed (marked as white dashed circles in the figures) in all three samples. These penetrations were limited to approximately 1 μm or less in depth.

4.3. Elemental Compositions and Crystal Structures of the Oxide Films

4.3.1. Sample at 0 dpa

SEM images of the corroded surface and a cross-section of the oxide layer and the underlying metal are shown in Figure 16. This figure shows that the oxide film consisted of two layers; a porous outer layer and an inner dense layer, with thicknesses estimated by image analysis to be approximately 2.4 and 2.0 μm , respectively.

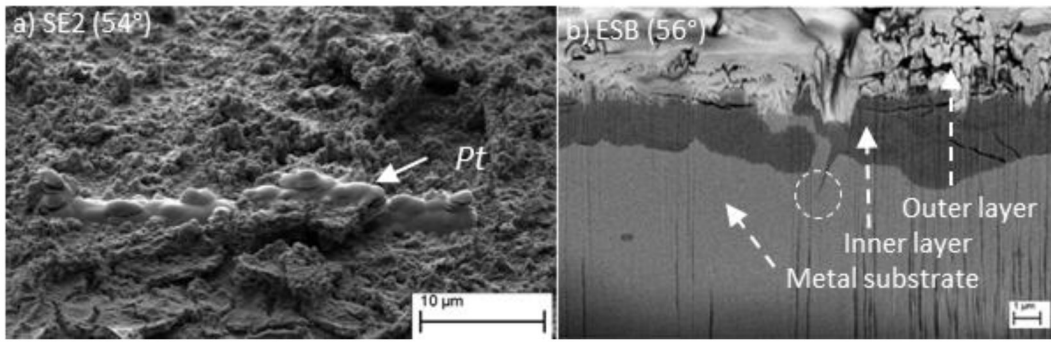


Figure 16

SEM images of the corroded surface (a) and a cross-section of the oxide film (b) of the "0 dpa" sample (G7K2A6).

Some granular oxides were seen in the upper part of TEM lamella G7K2A6. They were probably from the outer oxide layer and were retained after the final FIB thinning process. These grains had an average composition that was normalized to be $\text{Ni}_{0.8}\text{Fe}_{1.5}\text{Cr}_{0.7}\text{O}_4$, using a fixed oxygen concentration of 57 at%. The normalized average composition of the inner layer was $\text{Ni}_{0.5}\text{FeCr}_{1.5}\text{O}_4$. See Figure 17 for normalized compositions at different locations in the oxide film. In the STEM bright field (BF) mode, the inner oxide layer was not homogenous in image contrast but contained mixed bright and dark regions. Compared to oxides formed out-of-core [23], the outer oxide analyzed here was similar in composition, while the inner oxide layer had more pronounced differences in the compositions between the two different spinel phases; see comparison in Table 5.

Table 5

Comparison of oxide compositions normalized to spinel AB_2O_4 (A = Fe, Ni and B = Fe, Cr) between the "0 dpa" sample and ref [23].

Outer oxides	Inner "dark" oxides	Inner "bright" oxides	Ref
$\text{Ni}_{0.8}\text{Fe}_{1.5}\text{Cr}_{0.7}\text{O}_4$	$\text{Ni}_{0.6}\text{Fe}_{1.0}\text{Cr}_{1.4}\text{O}_4$	$\text{Ni}_{0.5}\text{Fe}_{1.0}\text{Cr}_{1.5}\text{O}_4$	This study
$\text{Ni}_{0.7}\text{Fe}_{1.5}\text{Cr}_{0.8}\text{O}_4$	$\text{Ni}_{0.3}\text{Fe}_{0.9}\text{Cr}_{1.8}\text{O}_4$	$\text{Ni}_{0.7}\text{Fe}_{1.2}\text{Cr}_{1.2}\text{O}_4$	[23]

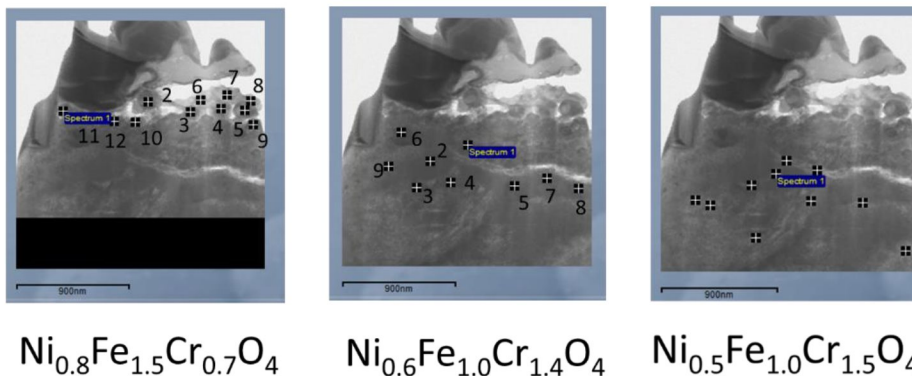


Figure 17

Average compositions of oxides at different depths of the oxide layer, which were normalized to spinel AB_2O_4 composition (A = Fe, Ni and B = Fe, Cr). The "0 dpa" sample.

The results of EDS mapping of two regions of the specimen are presented in Figure 18 and Figure 19. Each region analyzed contained the oxide film as well as the metal substrate. Several colors representing atomic percentages of a selected element were used to illustrate compositional differences in each region. Note, however, that the quantification of the elemental compositions did not take into account possible variations in lamella thicknesses and porosity of the analyzed region. The elemental concentration gradient, as observed at the oxide/metal boundary region, could be a result of an uneven oxide/metal boundary hit by the electron beam. In addition, the oxide compositions were in this case not normalized by the use of a fixed oxygen concentration of 57 at% for a spinel phase. Therefore, the oxygen concentrations at different locations of the oxide layer do not appear to be constant and, at most locations, it was greater than 57 at%. Accordingly, the concentrations of other elements in the same spinel phase would be under-estimated.

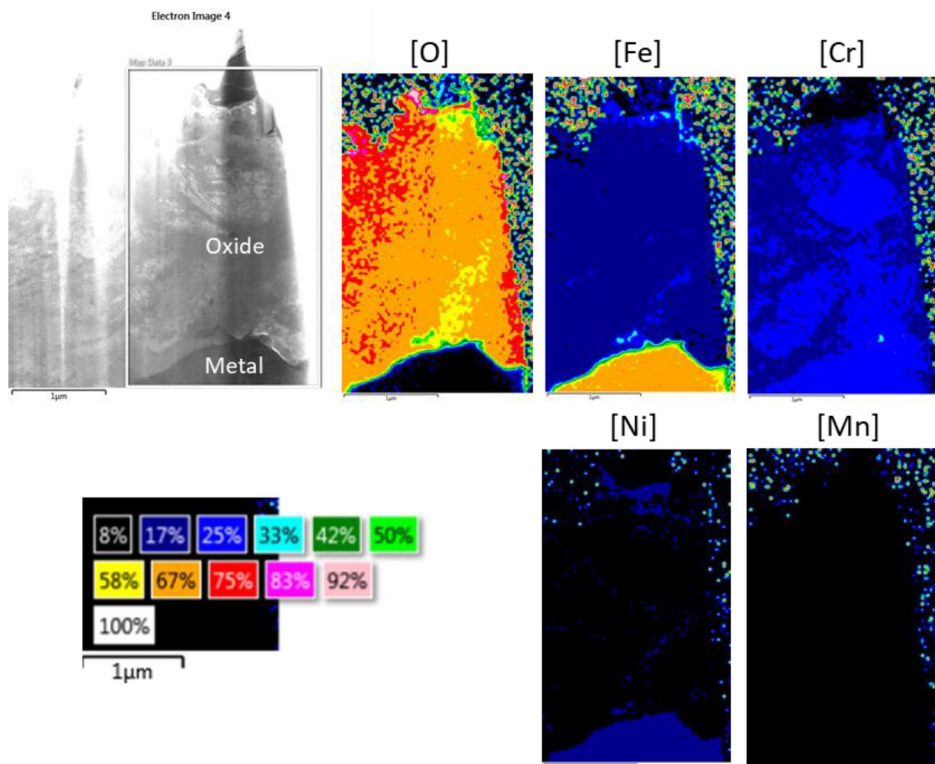


Figure 18
EDS mapping of the main elemental compositions (in at%) in the region of the TEM lamella indicated in the top left image. The "0 dpa" sample.

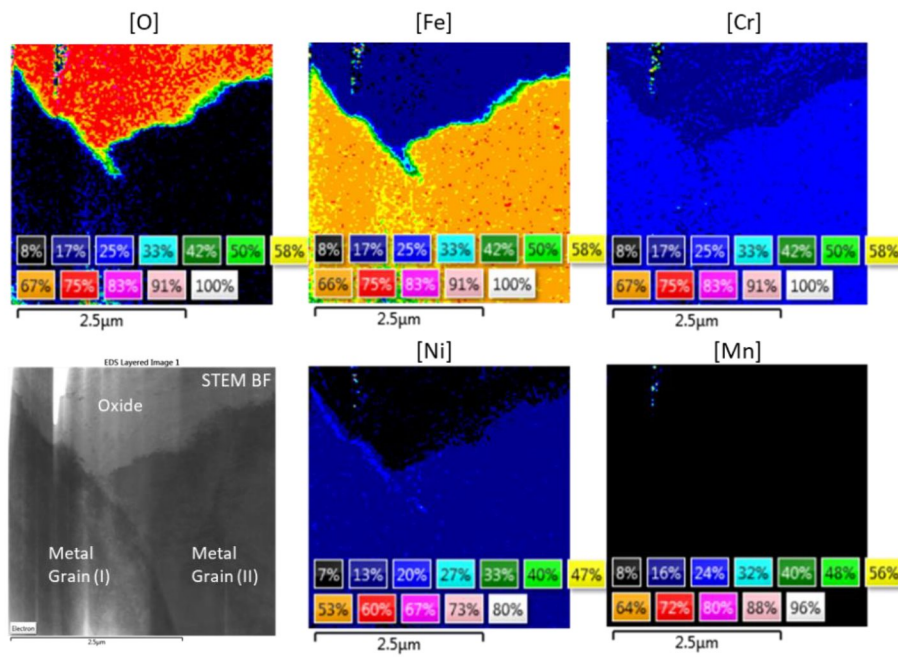


Figure 19
EDS mapping of the main elemental compositions (in at%) at the oxide/metal boundary region. The “0 dpa” sample.

An electron diffraction tilt experiment showed that the inner layer had epitaxial film characteristics (see the electron diffraction patterns in the insets of Figure 20 and FFT images of the insets of an HRTEM image in Figure 21). The metal and oxide can be indexed using FCC austenite and a spinel oxide Me_3O_4 , respectively.

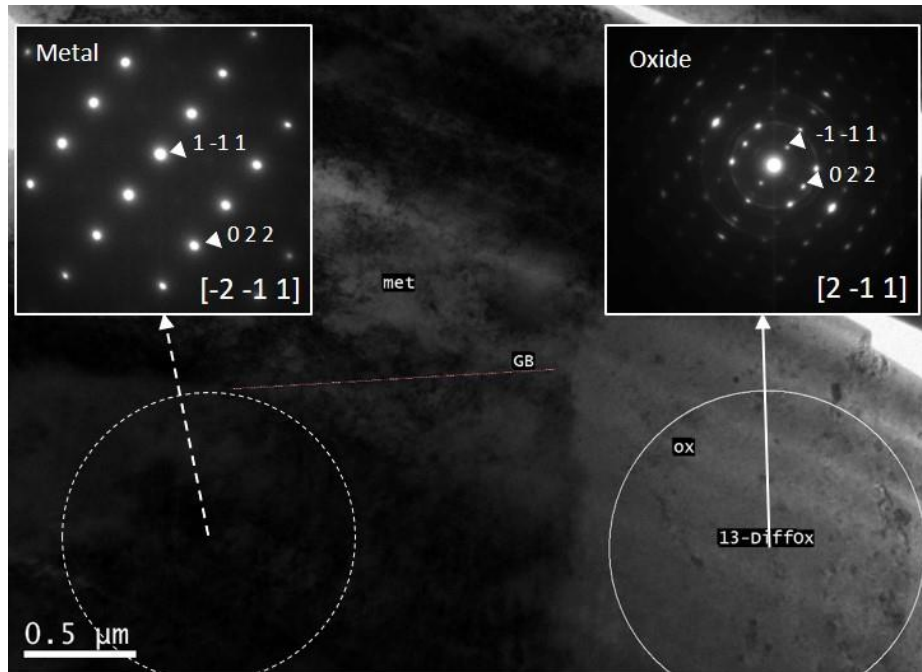


Figure 20

TEM image of a metal/oxide interface region and electron diffraction patterns in the metal and oxide shown in the insets. The initial zone axes, before rotating around $\langle 111 \rangle$ -fcc 9.8 degrees, were $[-3; -1; 2]$ and $[3; -1; 2]$, respectively, for the metal grain and the spinel grain. The "0 dpa" sample.

Compositional information of the main elements measured with EDS at three locations across the metal/metal grain boundary shown in Figure 19 is presented in Figure 22. At each point, a measurement time of 60 seconds was used. A slight enrichment of Cr and Mo and slight depletion of Ni at the boundary can be observed.

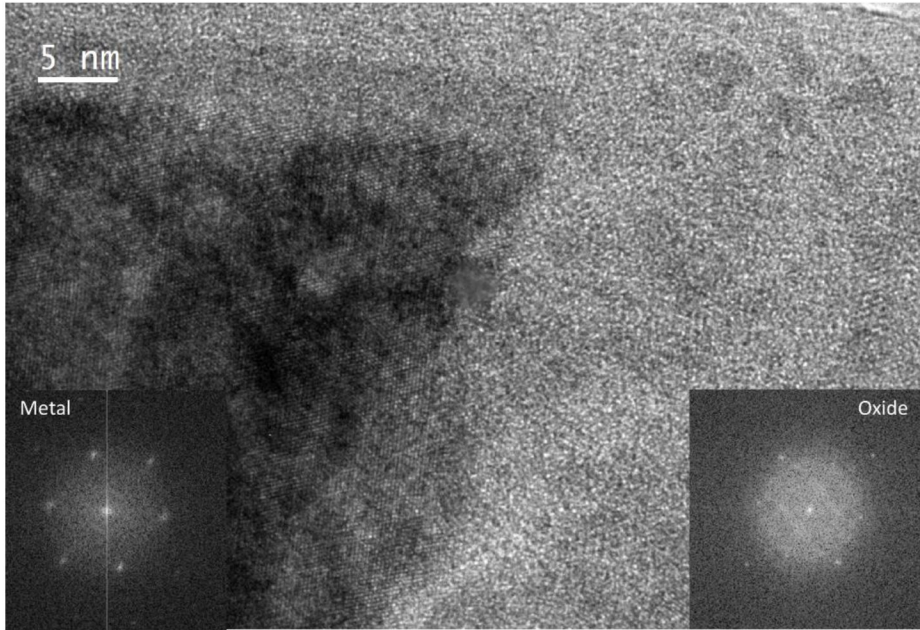


Figure 21
HRTEM image of a metal/oxide interface region. The insets are FFT images for the metal and oxide parts, respectively. The “0 dpa” sample.

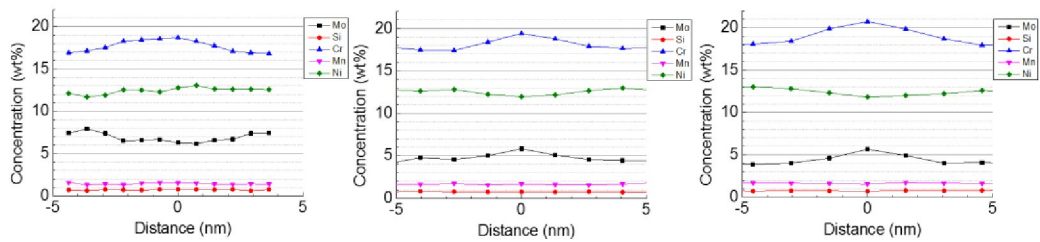


Figure 22
Elemental compositions at three locations across the metal/metal grain boundary shown in Figure 19. The X axis relate to the distance from the grain boundary, where “0” is at the boundary. The measurements were made normal to the grain boundary plane. The “0 dpa” sample.

4.3.2. Sample at 50 dpa

SEM images of the corroded surface and its cross-section are shown in Figure 23. One can see that the oxide film also consisted of two layers, a porous outer layer and an inner dense layer. The thicknesses of the outer and inner oxide layers were approximately 2.2 and 1.1 μm , respectively.

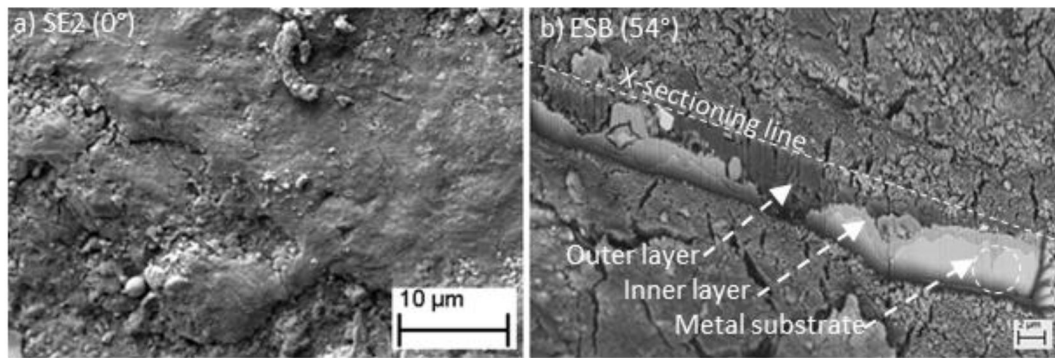


Figure 23

SEM images of the corroded surface (a) and the cross section of the oxide film (b). The “50 dpa” sample.

In the TEM-lamella (10-FTT-D3A51T), little oxide from the porous outer layer remained after the final FIB thinning process. Platinum, which was deposited onto the outer oxide layer to protect it from the ion beam damage during FIB milling, was found to be a dominant element of the outer layer. It even filled some places of the inner oxide layer, which probably were cracks or voids; see Figure 24. These outer oxide grains had an average composition that could be normalized to $\text{Ni}_{0.6}\text{Fe}_{1.6}\text{Cr}_{0.7}\text{O}_4$, using a fixed oxygen concentration of 57 at% for a spinel phase. Similarly, the average composition of the inner layer could be normalized to $\text{Ni}_{0.7}\text{Fe}_{1.1}\text{Cr}_{1.2}\text{O}_4$.

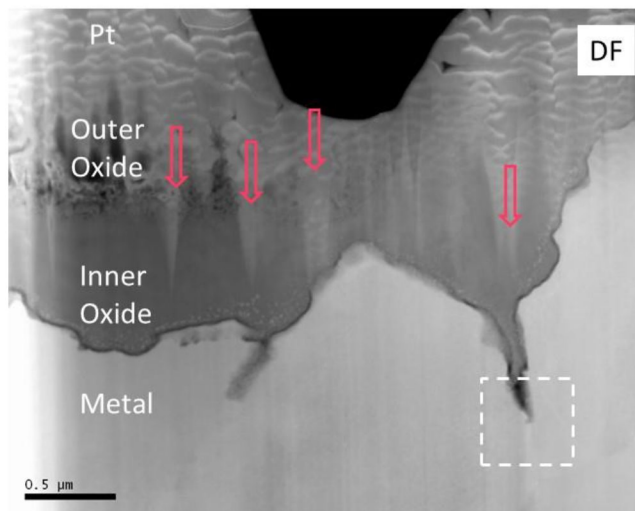


Figure 24

STEM dark field image showing traces of deposited Pt (arrowed bright regions) in the inner oxide layer. The “50 dpa” sample.

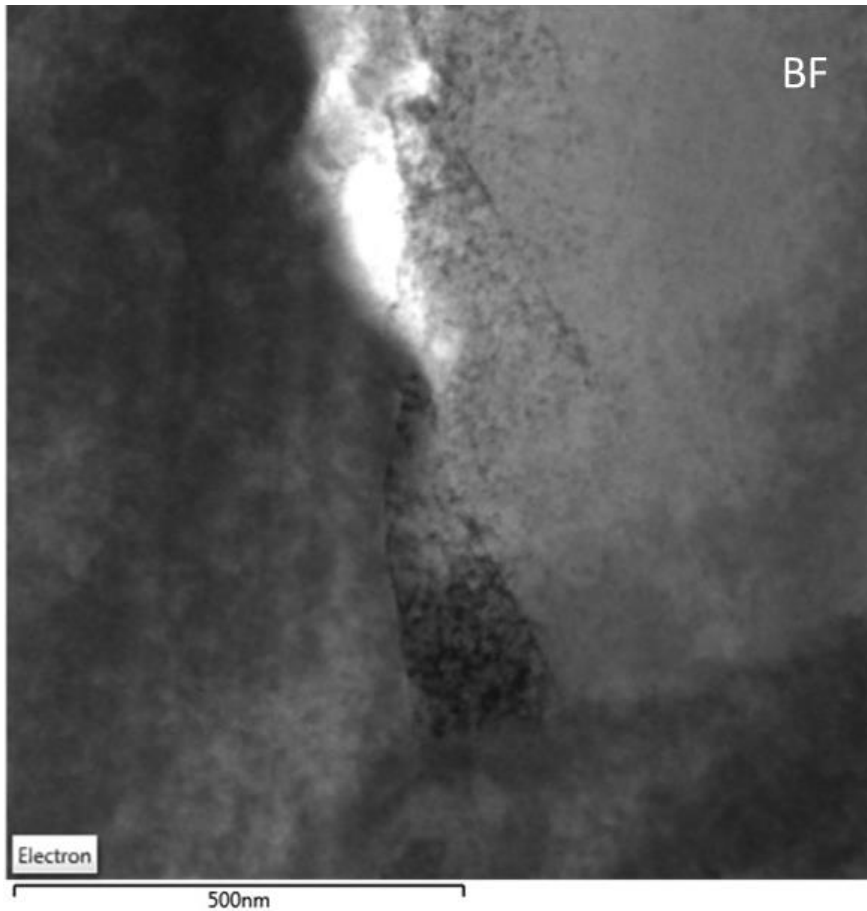


Figure 25

TEM bright field image showing the region with deeply penetrating oxide pocket (the dashed rectangle in Figure 24). The “50 dpa” sample.

A narrow, oxidized metal/metal grain boundary is highlighted by a dashed rectangle in Figure 24. Figure 25 is a TEM BF image (the lamella was slightly tilted from the imaging position used in Figure 24) of this region, and results of EDS mapping at this location are presented in Figure 26. The oxides inside the pocket had an average normalized composition of $\text{Ni}_{0.7}\text{Fe}_{1.1}\text{Cr}_{1.2}\text{O}_4$. It is noted that at the metal/metal grain boundary near, but ahead of, the oxide pocket, no elevated oxygen concentration was detected. At the tip of the oxide pocket, a small concentration of chlorine was also detected; see Figure 26. Immediately ahead of the oxide pocket, a metal grain with elevated Ni content (and associated reduction of Fe and depletion of Cr) was observed; see the elongated pink area on the Ni map in Figure 26. Based on EDS point analysis, the Ni content in this metal grain was ~19% while it was ~12% in the adjacent grains.

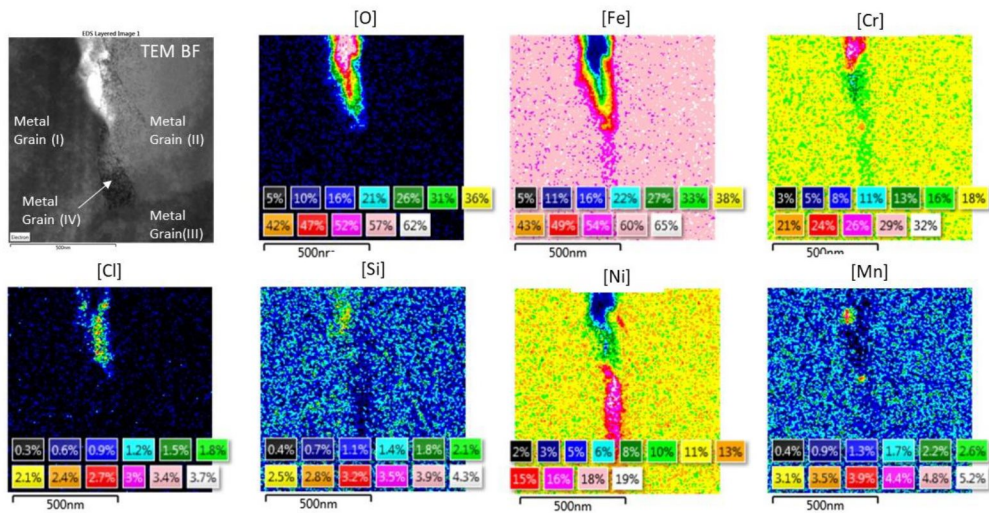


Figure 26

EDS mapping of the main elemental compositions (in at%) of the oxide pocket region of Figure 25. The “50 dpa” sample.

Figure 27 shows results from EDS mapping obtained at an oxide/metal interface region outside of the oxide pocket. Unlike iron, chromium appeared to be enriched more broadly at the oxide/metal boundary. From the nickel map and Figure 28, one can see that the oxide consisted of two regions having different nickel concentrations. The largest difference in nickel content was approximately 6 percentage points (at%). As noted in the previous paragraph in relation to Figure 26, similar nickel concentration heterogeneity can also be found in different metal grains.

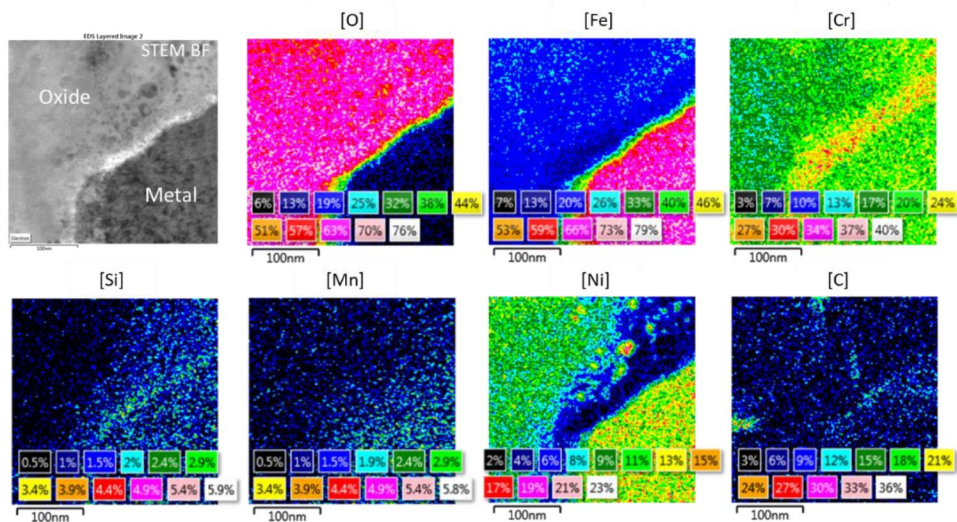


Figure 27

EDS mapping of the main elemental compositions (in at%) in an oxide/metal interface region. The “50 dpa” sample.

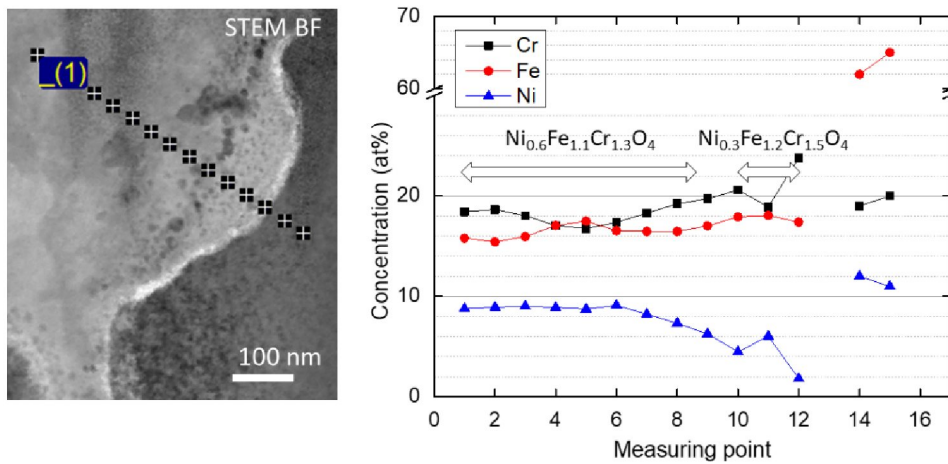


Figure 28
Composition profiles of some elements in an oxide/metal interface region (similar region as shown in Figure 27). The “50 dpa” sample.

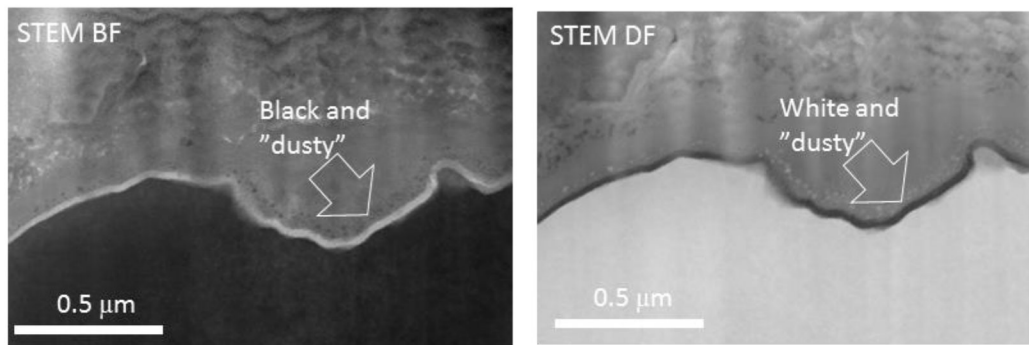


Figure 29
STEM cross section images of a metal/oxide interface region where some tiny “dusty” spots (ar-rowed) appeared. The “50 dpa” sample.

In Figure 29 one can see some tiny spots in the oxide layer, near the oxide/metal interface region. Similar features were absent in the 0 dpa sample. The EDS measurements of these spots were unable to detect any difference in composition relative to the adjacent oxide; see also discussion in Section 7.

Figure 30 shows a STEM image of the same oxide pocket location as above, but with the image rotated 90 degrees clockwise. The electron diffraction patterns from four oxide locations and two metal grains (white circles in the image) are shown as figure insets. The diffraction patterns from two oxide locations (Images No. 03 and 06) had crystal orientations similar to the underlying metal grain (“Metal 1”). The diffraction patterns from the deep oxide pocket (Images No. 01 and 02) exhibit mainly diffraction spots from the metal. Note that the two metal grains had fcc (denoted “Metal 1”) and bcc (“Metal 2”) crystal structures, respectively. On each metal grain the oxide crystal appeared to follow the same crystal orientation; see Figure 31. As elsewhere in the oxide, it was crystalline in the region close to metal/oxide interface (see Figure 32 for a HRTEM image and FFT images).

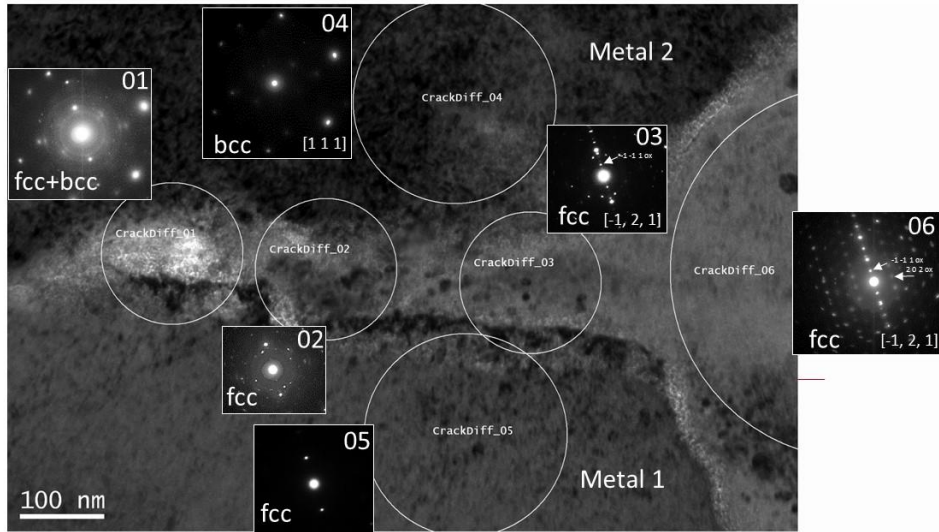


Figure 30

STEM bright field image at the metal/oxide interface region where the oxide appeared to have grown epitaxially in between the two metal grains. Electron diffraction patterns from both metal grains and four oxide locations are also displayed. The “50 dpa” sample.

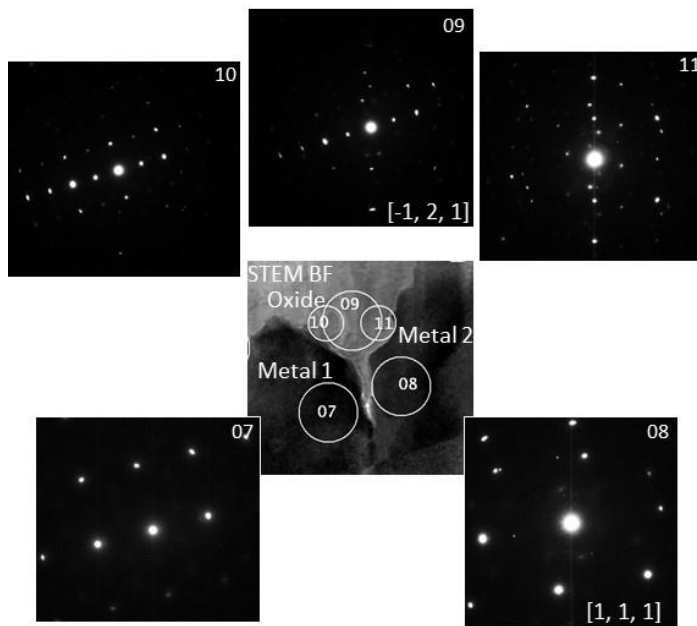


Figure 31

Electron diffraction patterns from two metal grains (pictures No. 07 and 08) and three oxide locations (pictures No. 09, 10, and 11). The “50 dpa” sample.

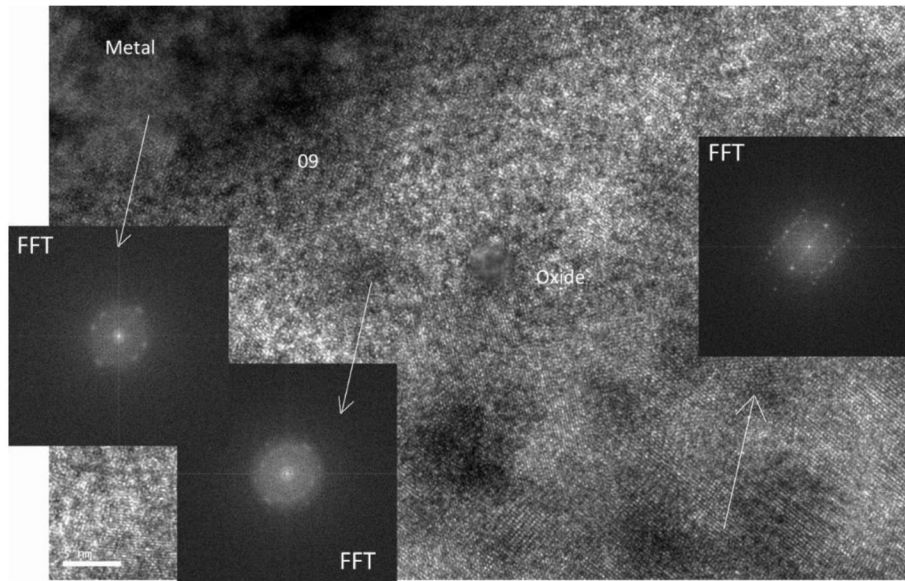


Figure 32
HRTEM image of an oxide/metal interface region where three figure insets are FFT images from the arrowed locations. The “50 dpa” sample.

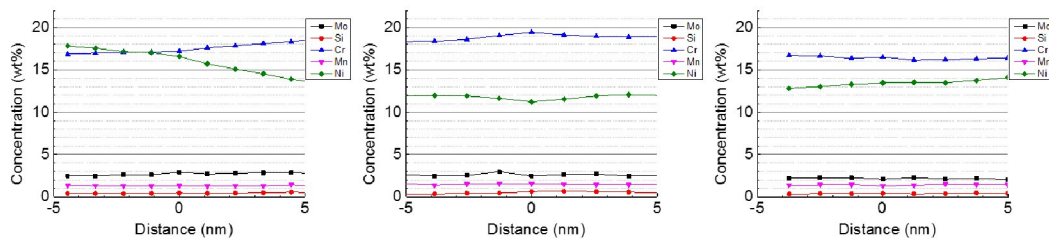


Figure 33
Elemental compositions at three locations across the metal/metal grain boundary shown in Figure 26. The X axis relate to the distance from the grain boundary, where “0” is at the boundary. The measurements were made normal to the grain boundary plane. The “50 dpa” sample.

Figure 33 shows the main elemental compositions determined with EDS at three locations along the metal/metal grain boundary shown in the TEM BF image Figure 26. In one of three cases (center graph in Figure 33), Cr and Mo were slightly enriched on the grain boundary while nickel was slightly depleted.

4.3.3. Sample at 100 dpa

SEM images of the corroded surface and its cross-section are shown in Figure 34. This figure shows that the oxide film consisted of two layers, a porous outer layer and an inner dense layer. The thicknesses of the outer and inner oxide layers were approximately 1.6 and 1.4 μm , respectively.

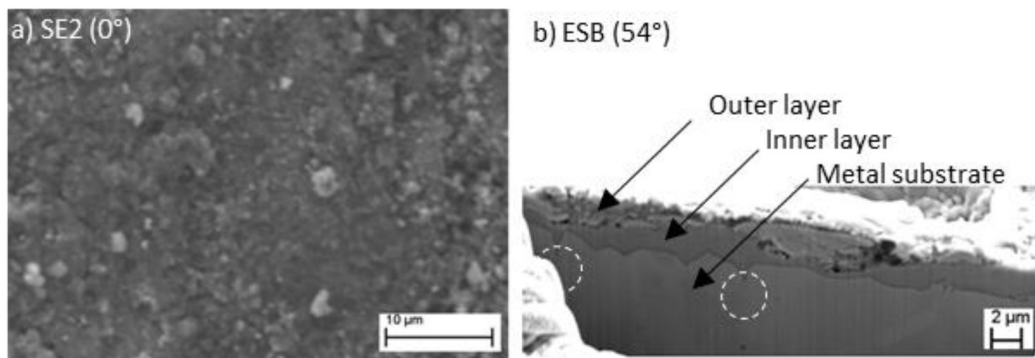


Figure 34
SEM images of the corroded surface (a) and the cross section of the oxide film (b). The “100 dpa” sample.

A montage of STEM images of TEM-lamella “10-FTT-D3C1” with associated electron diffraction patterns for the outer and inner layers, as well as their respective oxide compositions, are shown in Figure 35. Similar to Samples G7K2A6 (~0 dpa) and 10-FTT-D3A51T (50 dpa), the outer layer consisted of a mixed spinel with an average normalized composition of $\text{Ni}_{0.8}\text{Fe}_{1.2}\text{Cr}_{1.0}\text{O}_4$, while the inner layer was a spinel phase with an average composition normalized to $\text{Ni}_{0.7}\text{Fe}_{1.0}\text{Cr}_{1.3}\text{O}_4$. The inner layer also showed epitaxial film characteristics and it could be indexed with spinel oxide Me_3O_4 (see diffraction pattern from the dashed circle of Figure 35). Figure 36 shows the result of element mapping in a region near an oxide pocket, where oxide penetrated about one micrometer along a metal/metal grain boundary. The as-measured elemental compositions inside and around the oxide pocket are shown in Figure 37, whereas oxide compositions, normalized as a mixed spinel Me_3O_4 (Me=Fe, Ni, Cr), are shown in Figure 38. Note that a low oxygen content of 22 at% was detected by EDS at Location S9. The location was probably a mixture of metal and oxide.

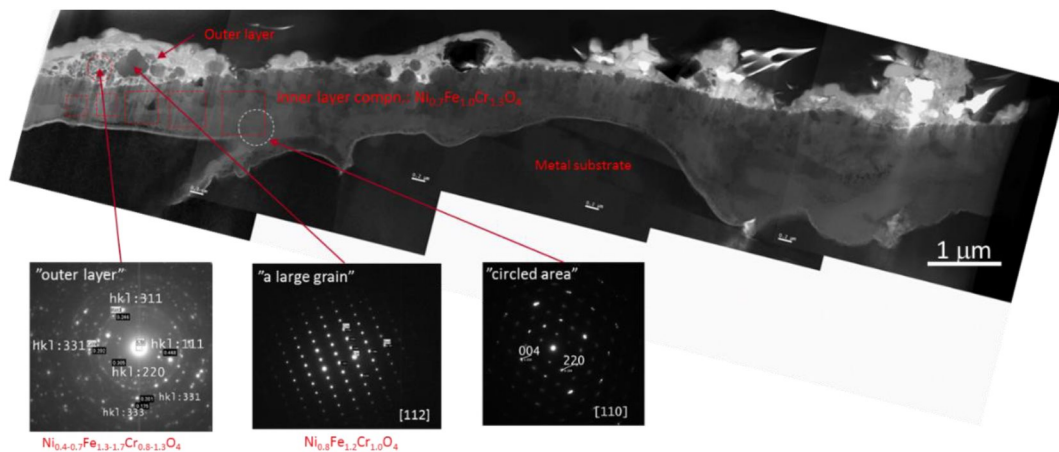


Figure 35
STEM cross section bright field image of the oxide films and diffraction patterns for the oxides in the outer and inner layers, and their approximate elemental compositions. The “100 dpa” sample.

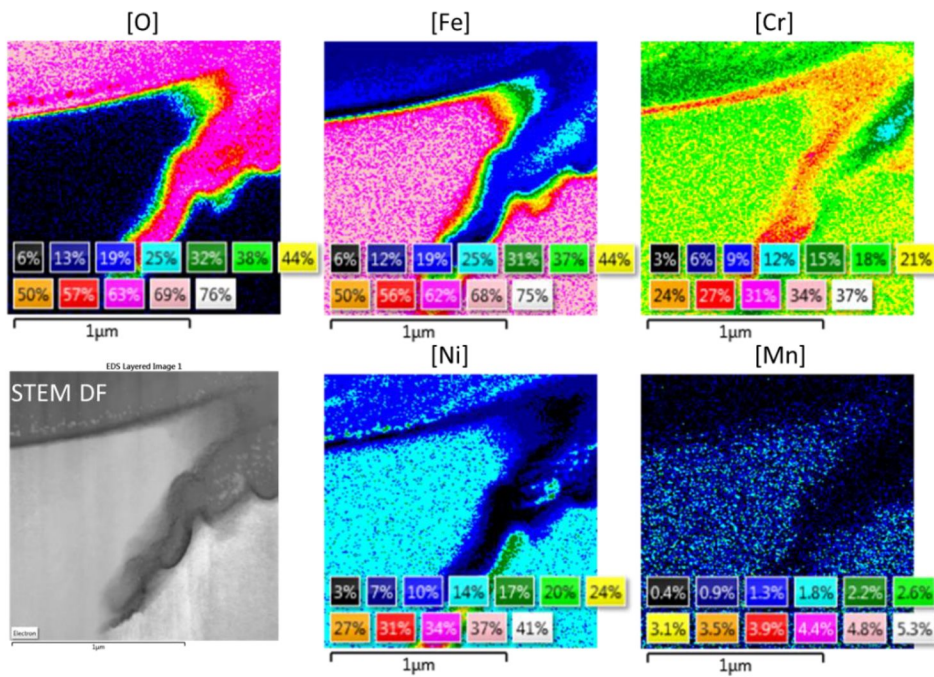


Figure 36
EDS mapping of the main elemental constituents (in at%) in the region where oxide had penetrated along a metal/metal grain boundary. The “100 dpa” sample.

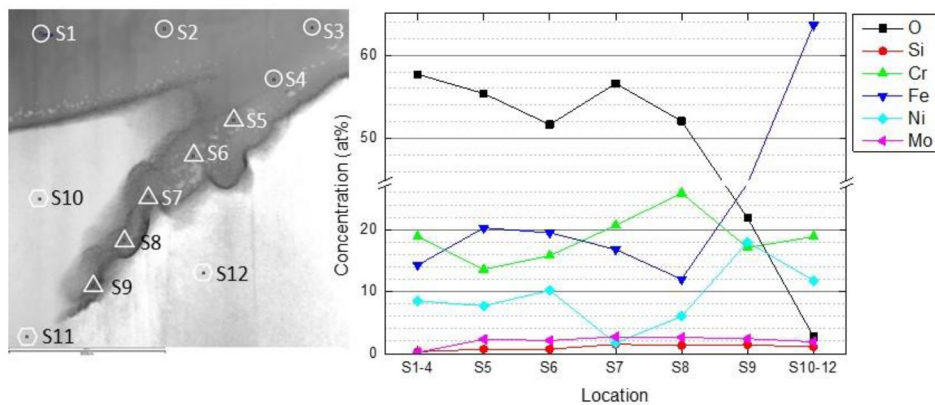


Figure 37
Elemental compositions at selected locations as measured by EDS point analysis. The displayed concentrations for Locations S1-S4 and S10-S12 are averaged values. The “100 dpa” sample.

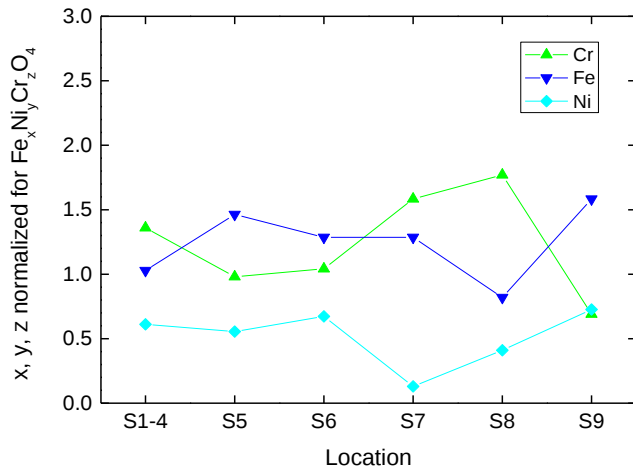


Figure 38
 Compositional variation inside the oxide pocket in Figure 37. All compositions are normalized using a mixed spinel $\text{Fe}_x\text{Ni}_y\text{Cr}_z\text{O}_4$ ($x+y+z=3$).

Elemental composition profiles taken at and in the vicinity of the oxide penetration shown in Figure 36 are presented in Figure 39. On the right-hand side of the oxide penetration, the metal was elevated in nickel and depleted in iron. The region with compositional variation is highlighted with a dotted line in Figure 39, and it can be seen that this region extends ahead of the oxide penetration.

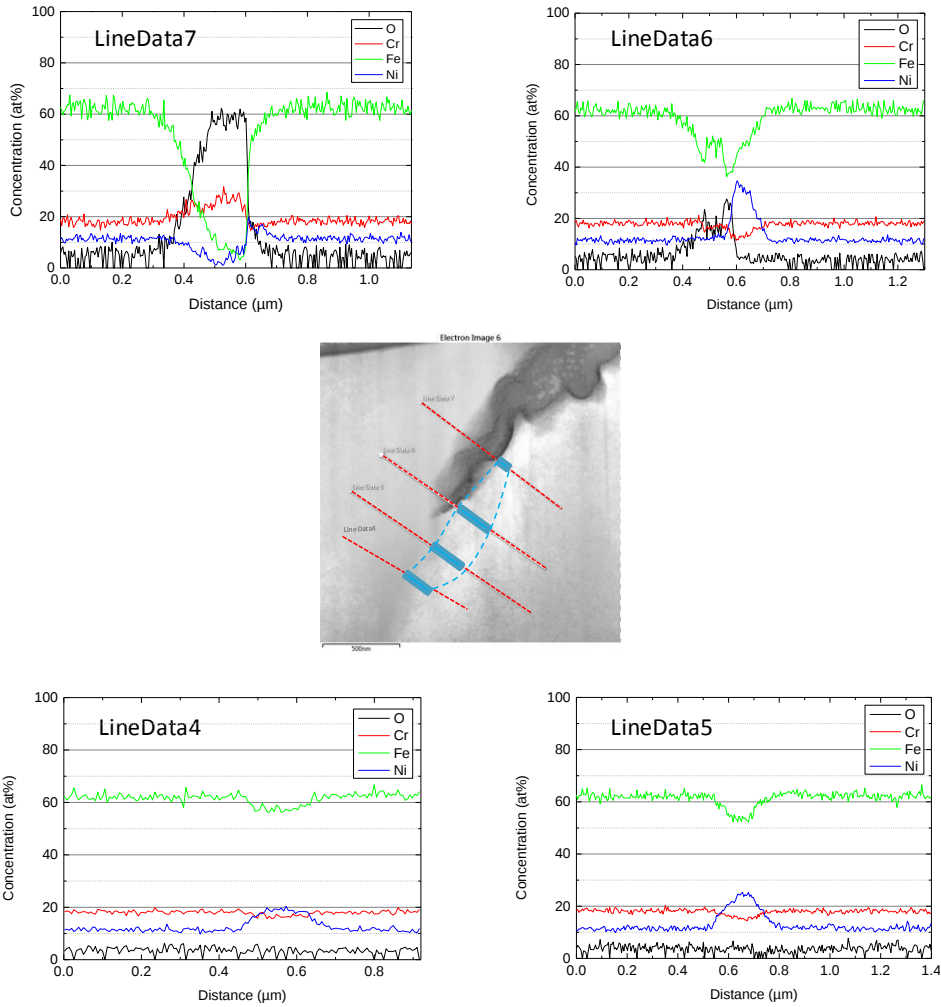


Figure 39
Elemental composition profiles at some selected locations in and ahead of the oxide penetration shown in Figure 36.

Similar to the 50 dpa specimen, tiny spots in the inner oxide layer near the metal/oxide interface was observed in the 100 dpa sample (Figure 40). HRTEM images, taken in a very thin part of the TEM lamella, showed that such spots had a round shape with a diameter of 10~20 nm (see Figure 41). The EDS analyses were, however, unable to detect any compositional difference between these spots and the surrounding matrix. The origin of the phase contrast and the possible crystal structure of these features remain unresolved at present.

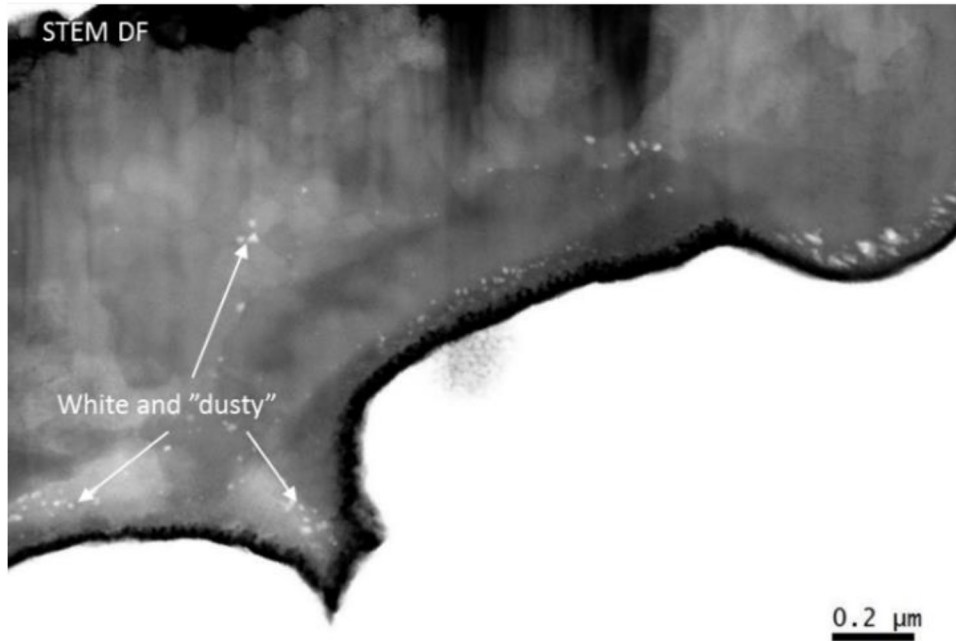


Figure 40
STEM cross-section micrograph at the metal/oxide interface showing the presence of tiny "dusty" spots (arrowed). The "100 dpa" sample.

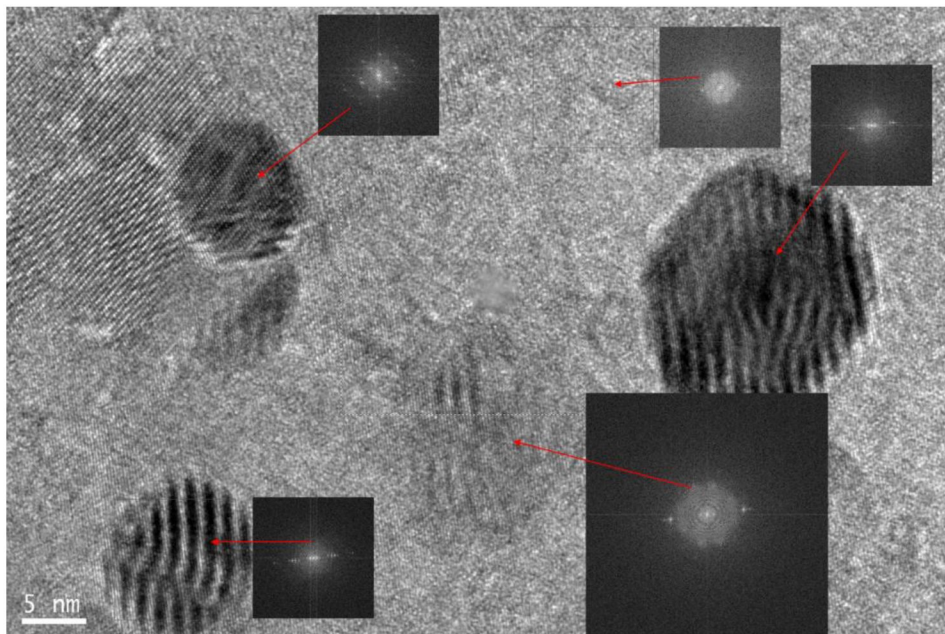


Figure 41
HRTEM image showing the "dusty" spots and their FFT patterns. The "100 dpa" sample.

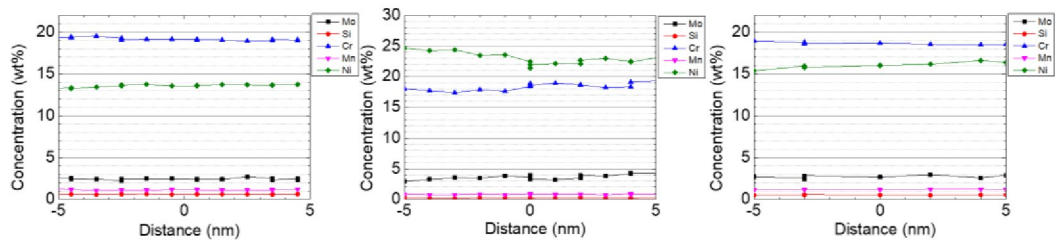


Figure 42

Elemental compositions at three locations across the metal/metal grain boundary shown in Figure 35. The X axis relate to the distance from the grain boundary, where “0” is at the boundary. The measurements were made normal to the grain boundary plane. The “100 dpa” sample.

The concentrations of the main alloying elements were determined with EDS at three locations along the metal/metal grain boundary shown in the TEM BF image of Figure 35. As shown in Figure 42, there was no detectable metal concentration change across the metal/metal grain boundaries.

5. TEM examinations of Bulk Material

5.1. Experimental Information

TEM bright- and darkfield images together with diffraction patterns were obtained with a field emission type TEM (JEOL, model JEM 2100F) operated at an acceleration voltage of 200 kV. Various tilting and focus settings were used to get the best conditions to examine different defects such as cavities, Frank loops, and radiation-induced γ' precipitates. Sample thicknesses were measured by EELS.

Point measurements of the chemical composition along lines across grain boundaries (GBs) were acquired with an energy dispersive X-ray spectroscopy (EDS) detector (Oxford Instruments – X-Max^N 80 TLE). During the scans, the microscope was operated in scanning TEM (STEM) mode to ensure a small probe size (0.5-1 nm in diameter). Thereby the composition is measured very locally since the interaction volume between the electron-beam and the material generating characteristic inner-shell transition X-rays is small. The grain boundaries were aligned edge-on with the electron beam in order to get a clear transition in the measured line-scan. For radioactive samples, the EDS detector will be affected by γ -radiation. Co-60 and Mn-54 will give a large low-energy tail, while decay of Fe-55 results in a significant contribution to the Mn-K α X-ray peak. Correction for background radiation was therefore made when necessary by acquiring spectra with the beam off using the same dead- and acquisition times as for the actual measurement. In addition to the grain boundary chemical composition, the matrix composition of the grains was also measured at a distance around 50 nm from the grain boundary.

Both electropolished TEM discs and FIB milled lamellae were used to investigate the FTT material at different dose levels. The preparation of these samples is described in Sections 3.2 and 3.3. Regarding 0 and 100 dpa, TEM discs were used to investigate the material. In addition, the metal part of the FIB lamella used for the metal/oxide interface investigations described in Section 4.3.3 was also examined in this part of the study. For the 50 dpa sample, FIB lamellae were taken from the bulk part of the material from a polished surface.

5.2. Microstructure - General

Figure 43 shows an overview of the microstructure of the 0 dpa material using both bright field (left) and dark field (right) imaging. Parts of several grains can be seen in the images. Selected area electron diffractions from the grains (not shown) confirm an austenitic structure. Very few precipitates, likely Cr-carbides, were found. The absolute composition, however, could not be determined due to x-ray contribution from the matrix.

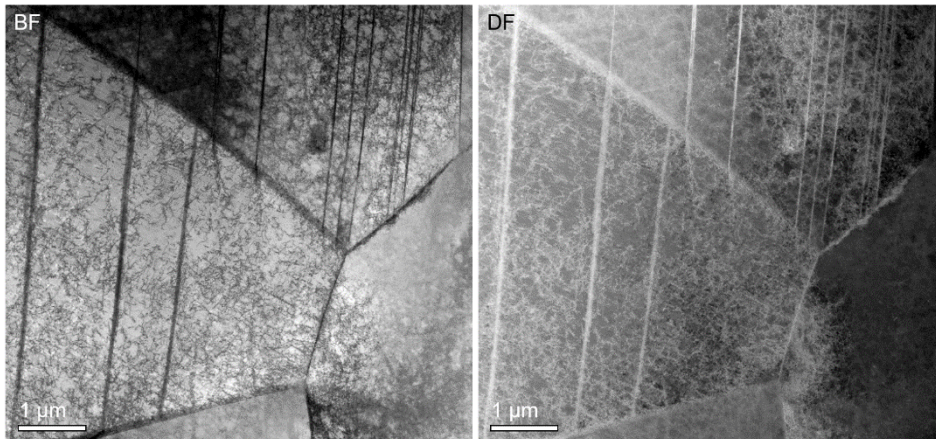


Figure 43

STEM bright field (left) and dark field (right) images of the structure of the unirradiated material.

Within the grains of the 0 dpa material, features such as twinning is seen together with a tangled dislocation network. This is consistent with the original structure of the cold drawn stainless steel and shows the stability of the dislocation network against thermally induced relaxation at 287 °C for 29 years. After irradiation to 50 and 100 dpa, it was noted during the examination (not documented by images) that the original dislocation network was gone while the twinning remained. Based on other investigations of PWR thimble tubes, this is an expected result. At about the same temperature as the unirradiated material (290 °C), loss of the original dislocation network was seen at 33 dpa [24] (lowest dpa investigated in that study), whereas at a higher temperature (323 °C), the original dislocation network disappeared at doses above 4 dpa [25].

5.3. Radiation Induced Segregation

To quantify the extent of radiation induced segregation (RIS), EDS point measurements were made across several grain boundaries for each dose level.

The measured matrix composition of the unirradiated material is shown in Table 6. With exception of Cr that is slightly overestimated, the measured composition correlates well with the expected.

Table 6

Chemical composition measured with EDS at grain boundaries compared to the composition measured in the bulk.

Element	Expected 0 dpa ¹⁾ (wt%)	0 dpa (wt%) ²⁾		50 dpa (wt%) ²⁾		100 dpa (wt%) ³⁾		100 dpa (wt%) ⁴⁾	
		bulk	GB	bulk	GB	bulk	GB	bulk	GB
Cr	17.4	19.0	20.6	18.2	16.1	15.2	12.3	19.5	17.7
Ni	13.3	12.6	11.1	10.8	15.8	11.4	15.9	11.4	16.3
Mo	2.69	2.6	4.7	3.7	2.1	2.5	1.2	2.4	2.6
Si	0.43	0.6	0.6	0.5	2.0	0.4	1.7	0.6	2.1
Mn	1.70	1.7	1.7	1.3	0.8	1.1	0.9	1.4	1.0

- 1) Chemical composition of one of the heats (see Table 1)
- 2) Data in graphical form provided in Figure 44 and Figure 45.
- 3) Data in graphical form provided in Figure 46
- 4) Data in graphical form provided in Figure 47

Two out of three investigated grain boundaries of the material at 0 dpa showed evidence of segregation. Figure 44 shows an example of a grain boundary where segregation was observed, while data in tabular form are shown in Table 6. A STEM DF image of the investigated grain boundary, with the position of the EDS line scan indicated, is shown in the figure, while the EDS results are shown in two plots. The plots show segregation is taking place in an 8-10 nm wide region around the grain boundary. While the Mo and Cr contents are enhanced at the grain boundary, Ni is depleted. This observation is in line with non-equilibrium segregation observed in a solution annealed Type 316, although the magnitude of the segregation was not as pronounced in this case [26]. Grain boundary segregation has also been observed in unirradiated Type 316 SS from thimble tubes [25, 27].

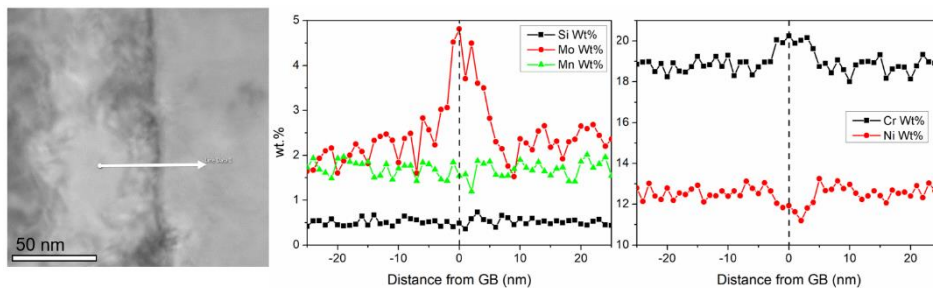


Figure 44

STEM DF image of the unirradiated material with the location of an EDS line scan indicated, and graphs showing the composition across the grain boundary.

The irradiated samples showed clear evidence of RIS, as can be seen in Figure 45, Figure 46 and Figure 47. These figures show grain boundary enrichment of Ni and Si and depletion of Mo and Cr. On either side of the grain boundary, the composition fluctuates, likely due to secondary phase particles. For example, Ni and Si are elevated at a location 15 nm from the grain boundary in Figure 45, which is in agreement with the APT results presented in Section 6.2.1; see also the discussion in Section 7. Grain boundary data in tabular form for all dose levels examined are presented in Table 6. The grain boundary compositional data obtained in this study are also consistent with literature data [27-30].

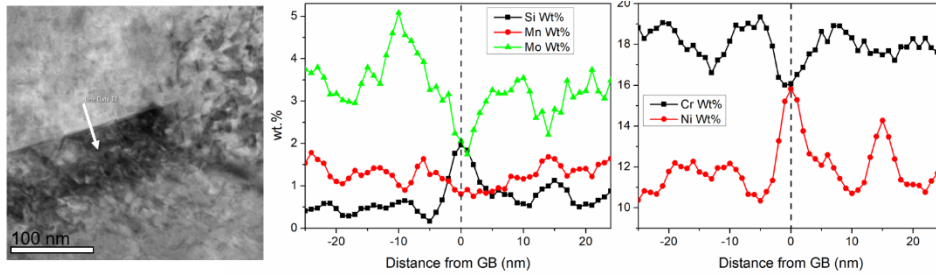


Figure 45
STEM DF image with the location of an EDS line scan indicated and graphs showing radiation induced segregation in the material irradiated to 50 dpa.

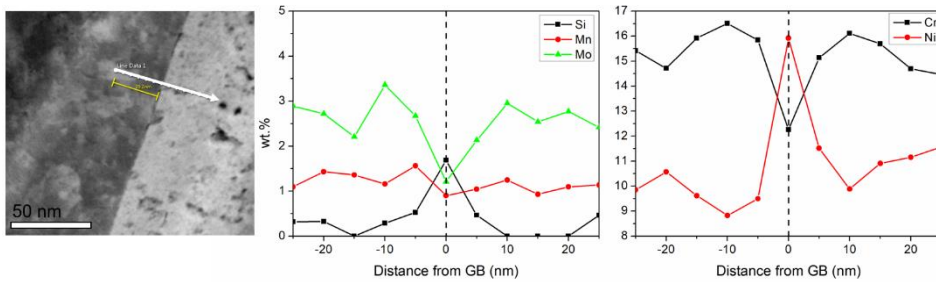


Figure 46
STEM DF image with the location of an EDS line scan indicated and graphs showing radiation induced segregation in the material irradiated to 100 dpa.

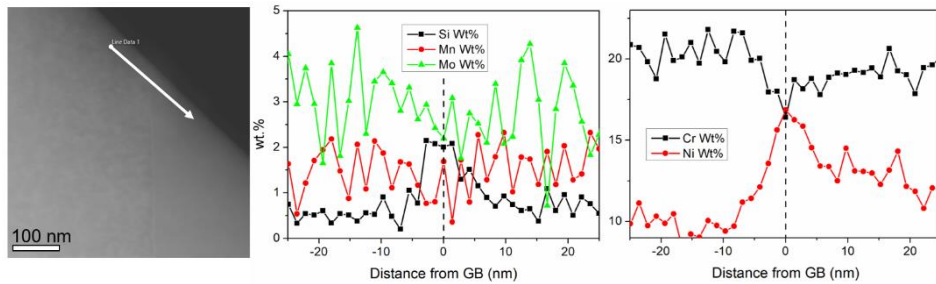
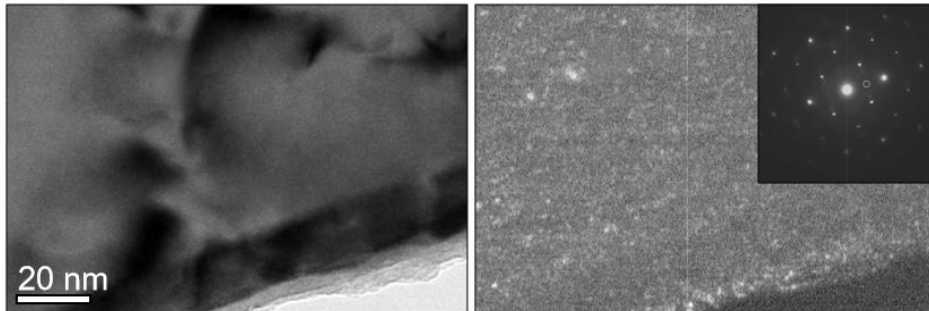


Figure 47
STEM DF image with the location of an EDS line scan indicated and graphs showing radiation induced segregation in the material irradiated to 100 dpa.

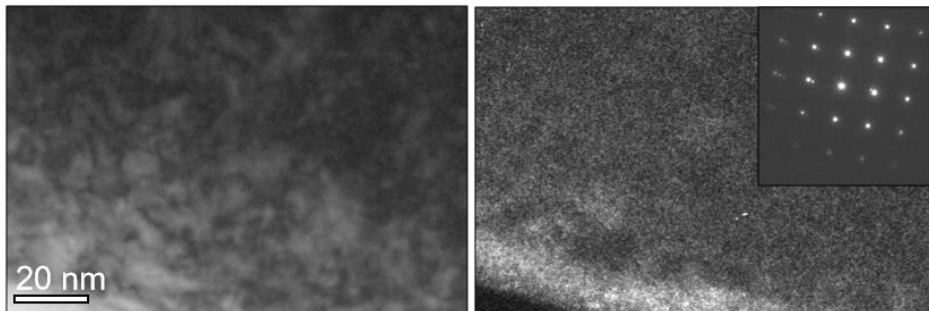
5.4. Precipitates

In search for γ' precipitates, the diffraction patterns of grains tilted to an $\langle 100 \rangle$ zone axis orientation was used. If present, the precipitates then show up as superlattice reflections. However, as seen on the top row of Figure 48, no clear diffraction spots from γ' precipitates could be found in the 0 dpa sample, which is expected for an unirradiated austenitic stainless steel. If the objective aperture (as marked with a circle in the diffraction pattern) is used to produce darkfield images at the position of the expected precipitates some vague dots appear. However, these were mainly observed close to the edge of the sample and most likely they were caused by contamination and/or artefacts.

0 dpa



50 dpa



100 dpa

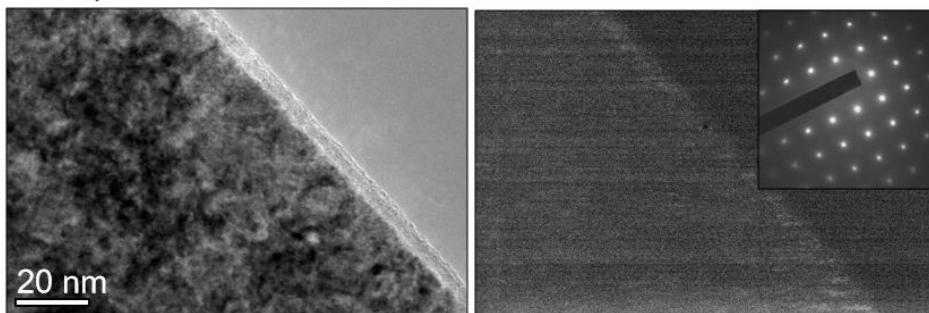


Figure 48

TEM images of the 0 dpa (top), 50 dpa (middle) and 100 dpa (bottom) samples showing the absence of γ' precipitates.

Also, the TEM images and diffraction patterns regarding the 50 and 100 dpa samples in Figure 48 show no or little evidence of γ' . Earlier observations in neutron irradiated austenitic stainless steels show that, in some cases, the formation of γ' can be delayed until > 50 dpa, while in other cases the precipitates form at a few dpa and later dissolve at 20-40 dpa [31]. Another parameter that could affect γ' precipitation is temperature. Although γ'

precipitates have been seen to form at temperatures as low as 270°C, this phase is not regularly observed in austenitic stainless steels below 400°C [29].

Edwards et al. examined material from a thimble tube, and they did not observe any γ' precipitates at 33 dpa, while some evidence of a low density of Ni and Si rich precipitates around 10 nm in size was observed in the material irradiated to 70 dpa [24, 32]. It is noted that the precipitates were observed in bright-field images, and that they did not produce any visible diffraction spots. This is somewhat in line with the observations in this study. It was noted that the irradiation temperature was lower for the 33 dpa sample (290°C) compared to the one at 70 dpa (315°C). They concluded that γ' precipitation is sensitive to temperature and that it occurs very slowly below 320°C. Fukuya and coworkers [25] studied material from thimble tubes at doses ranging from 1 to 73 dpa. They found that γ' was present in material with a dose of 4 dpa or higher, and that the precipitate density increased with dose. The average diameter of the precipitates was in this case roughly around 4 nm for all dose levels examined. The irradiation temperature was around 290°C for material with doses up to 4 dpa, between 313-323°C for doses ranging from 4 to 35 dpa, and around 300°C above 35 dpa.

5.5. Cavities

Fresnel contrast arise from differences in the refractive index between the structure adjacent to, e.g., cavities and the surrounding matrix. Using off-focus image conditions enhance the Fresnel fringes around cavities. A series of through focus images was therefore made to study the possible presence of cavities at the different dose levels.

Under-focused (500 nm) images of the material at different dose levels are shown in Figure 49. As expected, no cavities were present in the unirradiated material. The cavity density then increased with dose from $3.9 (\pm 1.7) \times 10^{23} \text{ m}^{-3}$ at 50 dpa, to $24 (\pm 2) \times 10^{23} \text{ m}^{-3}$ at 100 dpa. The size of the cavities, however, remained unchanged with dose and they ranged from 1 to 2 nm.

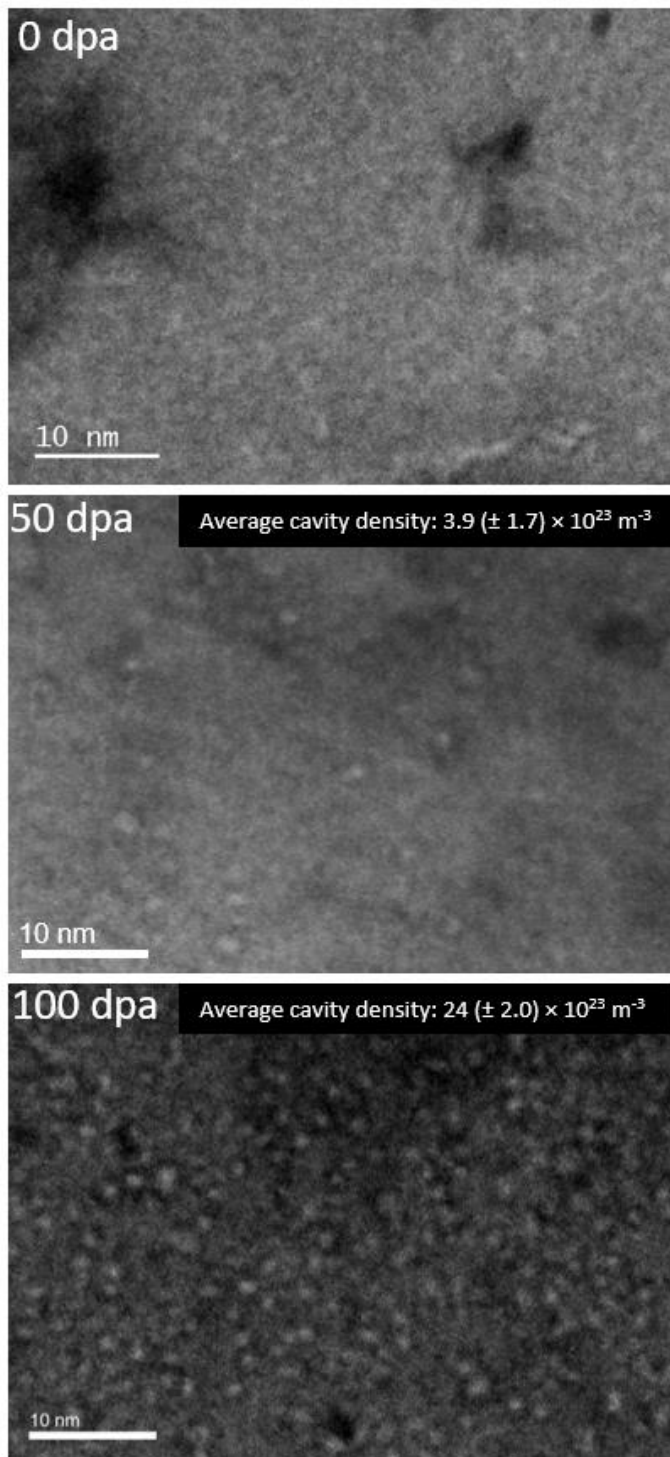


Figure 49
Under-focused BF TEM images showing cavities in the material at 0 (top), 50 (middle), and 100 (bottom) dpa.

5.6. Frank Loops

In principle, all faulted loops formed in austenitic steels are interstitial Frank loops lying on {111} planes [31]. The Frank loops consist of a stacking fault and form so called relrod streaks in the diffraction pattern when viewed edge on. This is normally done in TEM by tilting a grain into a two-beam condition ($g=[311]$) close to a $\langle 110 \rangle$ type zone axis. A small objective aperture placed over a relrod streak will produce a darkfield image with the loops showing up as bright lines perpendicular to the streak. To determine the total number of loops, the number of loops observed should be multiplied by four since Frank loops from only two out of the eight variants of the {111} are captured by the position of the objective aperture. Regarding quantification of loop density, the thickness of the sample was measured with EELS at the center of the used images.

Figure 50 shows the possible presence of Frank loops in the material at 0 dpa. Further examination would be needed to verify that the features observed are Frank loops. In the inverted electron diffraction pattern (inset in the upper left corner), a beam stopper has been used to stop the directly transmitted beam and allow a longer exposure time. A weak relrod reflection is circled in the diffraction pattern. The circle also indicates the position of the objective aperture used for the dark field image. The density of possible Frank loops is low with a size distribution ranging from 4 to 29 nm. Because of too few Frank loops present in the samples, it was not possible to reliably quantify the density nor their size distribution. The presence of Frank loops in the 0 dpa sample would suggest that it is not completely unirradiated. As shown in Figure 3, the 0 dpa samples were taken from a location not far from the active fuel, so it is possible a few neutrons have reached that position.

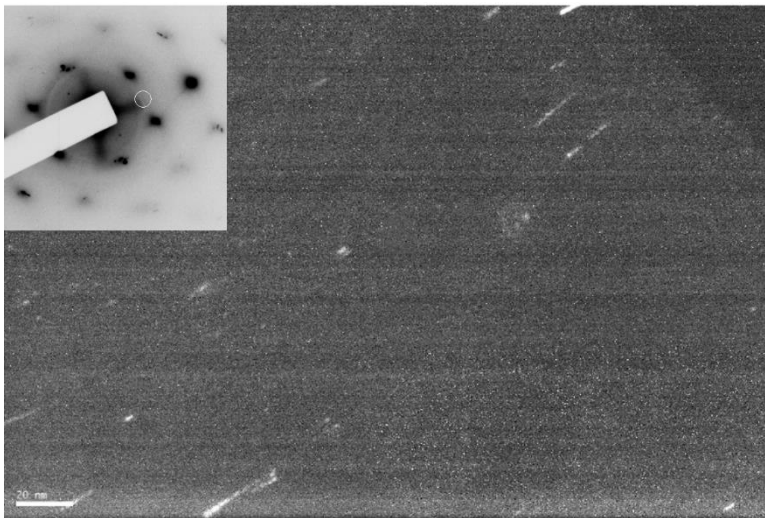


Figure 50

Dark field image of possible Frank loops at 0 dpa. Objective aperture position is indicated on the electron diffraction inset.

Although there were some difference in sample thickness, it can be seen in Figure 51 and Figure 52 that the number of Frank loops is, as expected, larger in the 50 and 100 dpa samples than in the sample at 0 dpa. (Figure 50). These figures also show that the Frank loop size distribution in the 50 dpa sample is almost identical to the 100 dpa sample. The measured loop density for the 50 dpa sample ($2.7 \pm 0.5 \times 10^{22} \text{ m}^{-3}$) is overlapping with that of the 100 dpa sample ($3.7 \pm 1.4 \times 10^{22} \text{ m}^{-3}$), while the average loop sizes of, respectively, 10 and 11 nm for the 50 and 100 dpa samples are very similar.

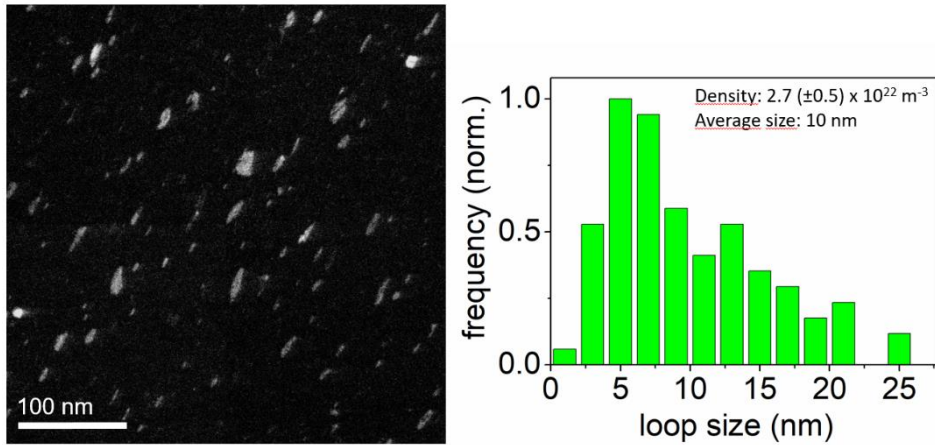


Figure 51
Dark field image of Frank loops in the sample at 50 dpa.

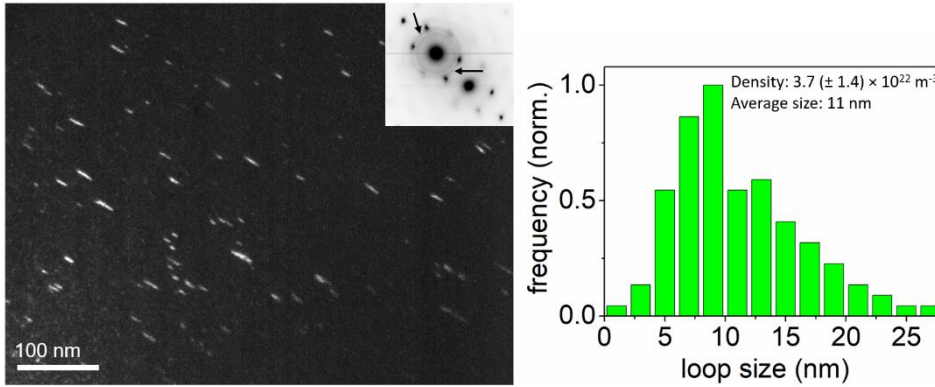


Figure 52
Dark field image of Frank loops in the sample at 100 dpa. The insert of electron diffraction pattern shows rel-rods marked with arrows.

6. APT Analyses

6.1. Experimental Information

The APT analyses were performed in a LEAP 3000X HR, with a laser energy of 0.4 nJ (as there were background issues with 0.3 nJ), 30-70K (mostly 30 K, 70 K when oxides were assumed to be in the analysis), 200 kHz, and target evaporation rate of 0.1-0.5% (mostly 0.2%).

6.2. APT Results

First, results from analysis of the bulk of the material is shown, then the grain boundaries that were successfully analyzed and then oxides and metal-oxide interfaces.

6.2.1. Bulk

In the 0 dpa material the distribution of elements in the bulk of the metal was found to be random, as expected for an austenitic solid solution. The composition can be seen in Table 7, where the error given is the standard deviation for the three analyses used to determine the composition, as the difference between the analyses usually are larger than the counting error within one analysis. Most of the elements are in relatively good agreement with the expected composition. V is an exception, with one order of magnitude larger content in the APT measurement than expected. V has one main naturally occurring isotope, but the only possible spectrum overlap expected is CrH, that was taken into account. However, this did not significantly change the V content, and the isotope signal of CrH⁺⁺, Cr⁺⁺, Fe⁺⁺, Mn⁺⁺, and Ni⁺⁺ were as expected, indicating that the high V content is real.

The S content could not be measured, as the mass-to-charge ratio overlaps with O₂ at a mass-to-charge ratio of 32 Da (0.02-0.05 at%, that is excluded from the content as the small O₂ is not expected to originate from the specimen itself). Thus, the information gained from the APT analyses is that the total amount of S at least should be lower than 0.05 at%.

At the estimated field during the evaporation (around 20 V/nm, considering the Ni⁺/Ni⁺⁺, Fe⁺/Fe⁺⁺ and Cr⁺/Cr⁺⁺ ratios), Al is expected to evaporate as Al⁺ at 27 Da, thus overlapping with isotopes of both Cr and Fe, that mainly evaporate as ⁺⁺ ions. The decomposition of the peaks gives poor results concerning Al as there is considerably more Fe and Cr in the material. In some analyses, peaks were found at 21.5 Da, possibly matching AlO⁺⁺. However, the probability of the peak being AlO⁺⁺ is estimated to be small due to the small total Al content, as it would only contain a fraction of the total Al ions. Thus, the Al content could not be estimated, although there is possibly some smaller amounts of Al in the material.

Ti is expected to evaporate as ⁺⁺ ions. At 24 Da in the spectrum, where the most abundant isotope peak of Ti⁺⁺ should be located, one peak was found. This peak was, however, assigned to C₂, that was found to match the mass-to-charge ratio better, see Figure A.5 in Appendix A. The total content of C₂ was found to be 0.009 at%, and as seen in the

figure, an amount of Ti smaller than this should be possible to detect. Thus, it is reasonable to estimate that the APT results support the expected less than 0.005 at% Ti.

Sn is expected to evaporate as Sn⁺⁺. Some of the Sn⁺⁺ ions thus overlap with Ni⁺. The Ni also have thermal tails, increasing the background in this part of the spectrum and making the detection of small amounts of Sn impossible.

In the analysis, B and Cu were also detected, although not present in the expected composition. Cu is common in steels as an impurity.

Table 7

Average composition of the metal, based on three of the analyses, including the expected composition from Table 1 for comparison.

Element	Content (at%)	Std. dev (at%)	Content (wt%)	Std. dev (wt%)	Expected (wt%)
C	0.13	0.04	0.03	0.01	0.045
Si	1.27	0.01	0.64	0.01	0.43
Mn	1.37	0.07	1.36	0.07	1.70
P	0.015	0.002	0.008	0.001	0.026
S	<0.05	-	<0.03	-	0.01
Cr	18.21	0.06	17.11	0.06	17.4
Ni	11.72	0.26	12.43	0.27	13.30
Mo	1.11	0.13	1.93	0.22	2.69
Co	0.003	0.005	0.003	0.005	0.04
V	0.25	0.05	0.23	0.05	0.019
Ti	< 0.005	-	< 0.004	-	< 0.005
Al	-	-	-	-	0.008
Sn	-	-	-	-	< 0.005
N	0.30	0.12	0.08	0.03	0.044
Fe	65.46	0.49	66.00	0.49	64.28
B	0.003	0.001	0.0007	0.0002	-
Cu	0.16	0.02	0.18	0.02	-

In the irradiated materials, Ni-Si precipitates were found. In Figure 53, precipitates in the 50 dpa sample are shown. These are presumably γ' (Ni₃Si) or precursors to this phase. There was some Mn in some of the precipitates, but Mn was found to be depleted in the precipitates in other analyses. In some cases, Mn appears to be enriched in the center of the precipitate, but not closer to the surface. Fe, Cr, and Mo were all found to be depleted in the precipitates, which however were enriched in Cu. Phosphorus was found segregated to the surface of the same precipitates. The average Ni/Si ratio in the precipitates was found to vary between 1.2 and 2.0 in the material irradiated to 50 dpa. In the 100 dpa material, the Ni/Si ratios were between 2.2 and 3.1 (one analysis with ratio above 3, four analyses with 2.2-2.5). The Ni and Si distribution fluctuates outside iso-concentration surfaces as well, see Figure 54, and thus the best threshold for defining precipitates is hard to determine (the threshold Ni+Si=30% was used for number density measurements). This might be a result of the presence of dislocation loops that are enriched in Ni and Si. The

precipitate number density varied between 0.7 and $1.2 \times 10^{23}/\text{m}^3$ after irradiation to 50 and 100 dpa, but no systematic difference was observed between the two doses examined. The size of the Ni-Si precipitates ranged from 2 to 8 nm in diameter if a spherical shape is assumed, with most precipitates around 4-5 nm (using the maximum separation method, MSM [33], with solute element Si, $N_{\min}=20$, $d_{\max}=L=e=0.7$ nm, 8th order, assuming only Ni and Si contributing to the size) in both 50 and 100 dpa materials. It was not possible to detect any difference between the material irradiated to 50 and 100 dpa.

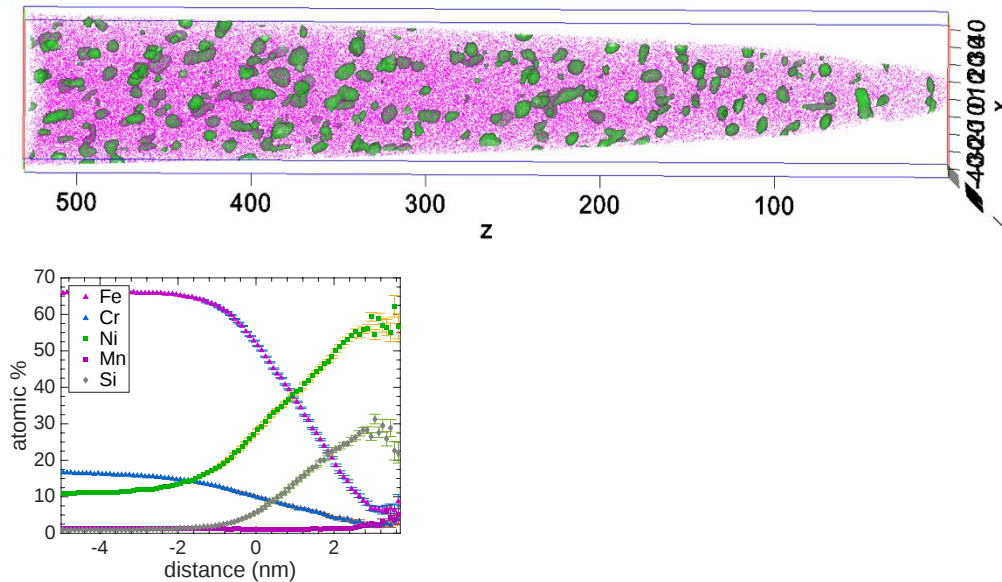


Figure 53

Ni-Si precipitates in the material irradiated to 50 dpa. Fe atoms are pink, green isosurfaces correspond to Ni+Si 31.4 at.%. The proxigram corresponding to the isoconcentration surfaces is shown below the reconstruction. Scale in nm.

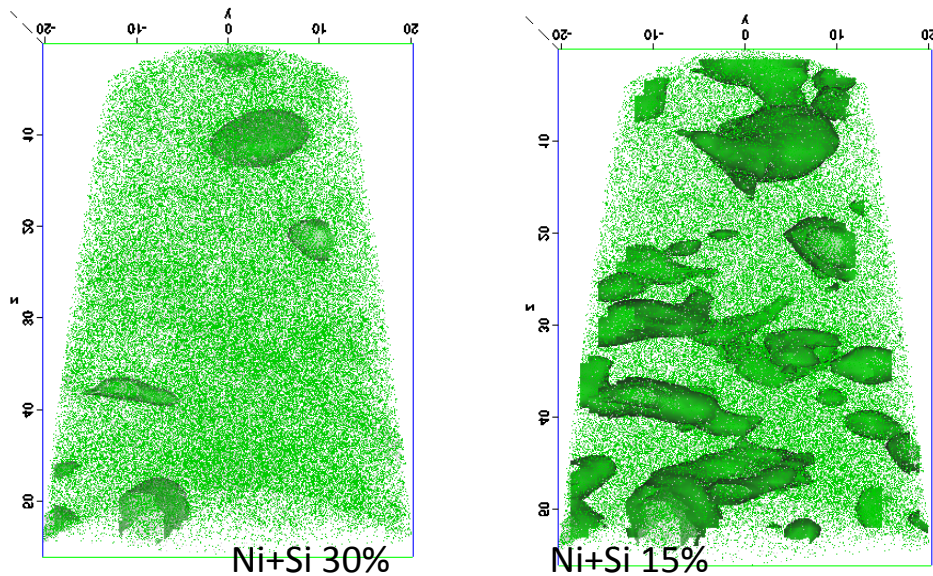


Figure 54

Ni-Si precipitates in the material irradiated to 50 dpa. Different thresholds for iso-concentration surfaces are shown, Ni-Si precipitates appear connected when lowering the threshold.

6.2.2. Grain Boundaries

Due to the difficulty of specimen preparation, only three grain boundaries in material irradiated to 100 dpa were successfully analyzed. No grain boundaries could be analyzed in the 0 and 50 dpa materials, although four and ten attempts to analyze the grain boundaries in these materials were made, respectively. Results for one grain boundary are presented here, while data for two other grain boundaries are provided in Appendix A.

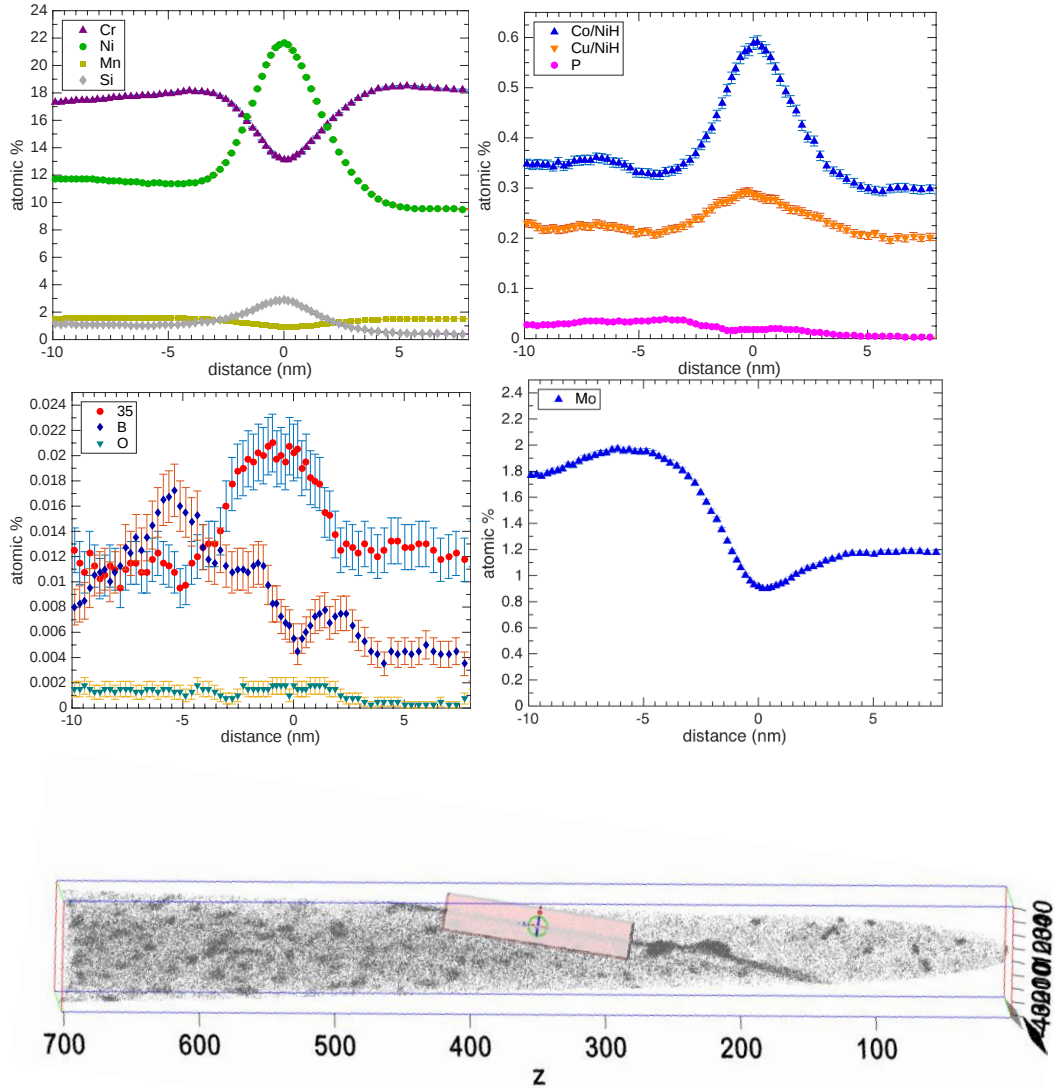


Figure 55

Grain boundary around 2 μm from the oxide in the material irradiated to 100 dpa. Si atoms are shown in grey. The box is used for compositional profiles taken across the grain boundary shown above the reconstruction.

In Figure 55, a grain boundary located around 2 μm from the oxide is shown. The number density of Ni-Si precipitates is lower close to the grain boundary (like a precipitate free zone (PFZ)). Close to the boundary the Ni and Si atoms have segregated to the boundary instead of forming precipitates. A few Ni-Si precipitates were also found nucleated on the grain boundary (with composition 60 Ni-25 Si-10 Fe-1 Cr). Other Ni-Si particles in this

analysis were found to be 53 Ni-24 Si-14 Fe-3.5 Cr, i.e. the Ni/Si ratio was similar (2.2 - 2.4), and Fe and Cr were depleted more in the grain boundary precipitates than in the bulk precipitates. This is expected as the trajectory effects during field evaporation affect the composition of the precipitates, and the effect is more prominent in smaller precipitates. The Ni-Si precipitates on the grain boundary were larger than the ones in the matrix. In Figure 55, the two precipitates on the boundary are estimated to have diameters of around 13 nm. The grain boundary itself is depleted in Cr and Mo and enriched in Ni, Si, B, and possibly slightly in Cu. The latter element is probably NiH that is overlapping in the mass spectrum. The indicated enrichment of Co is most probably also the overlapping NiH, as Co is not expected to segregate and the relative enrichment of Co/NiH is the same as for Ni. No clear traces of O were found at the grain boundary.

One unidentified enrichment (0.02 at.%) with a mass-to-charge ratio of 35 Da was found, that could possibly be Al_2O^{++} . Another possibility is that this peak is the largest isotope of Cl^+ . If it was Cl in the grain boundary, this would be highly interesting as it would affect the corrosion properties. Cl also have an isotope at 37 Da (natural abundance 25%), that is present in the spectrum at roughly the right size, but as one of many equally small, hard-to-identify peaks. The number of atoms in the 37 Da peak is too small to locate to the boundary. Comparing the spectrum at and close to the grain boundary with the spectrum in the bulk of the grains, it is found that there are ions from both 35 and 37 Da peaks inside the grains as well as at the boundary. Cl is, however, expected to only occur at the grain boundary, if present at all. The enrichment of 35 Da was very small, only reaching about 0.02 at.%; see the profile in Figure 55.

In the grain boundaries 15-20 μm from the oxide, no $m/n=35$ Da peak was found. The concentrations of the other elements were similar to the grain boundary described above. The profiles, similar to those in Figure 55, can be seen in Appendix A.

6.2.3. Oxides

Oxides of varying compositions were analyzed. In the oxides analyzed, the distribution of the elements was, in most cases, random. The oxides contain mainly Fe and Cr as metallic atoms, but also varying amounts of Ni, see Table 8, where the main composition of three different oxides are given. It should be noted that the oxygen content of oxides measured with APT is not very accurate, so it is delicate to determine which type of oxide it is.

Table 8
Oxide compositions for some of the analyses.

Dose level	O (at.%)	Fe (at.%)	Cr (at.%)	Ni (at.%)
50 dpa	51	20	19	7.7
50 dpa	45	22	25	5
100 dpa	46	14	33	1.9

In some analyses, the oxide-metal interface was analyzed. In the material that was not irradiated, 0 dpa, an oxide-metal interface was analyzed around 2-5 μm from the oxidized grain boundary; see Figure 56 and Figure 57. The oxide contains mainly Fe and Cr. The interface is not straight, but very complex in shape. The Ni content appears to be high close to the oxide-metal interface.

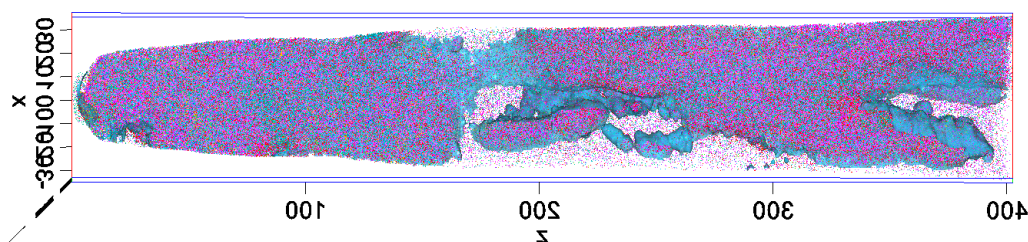


Figure 56
Oxide-metal interface in the unirradiated material. The oxides are marked, whereas the empty regions are metal.

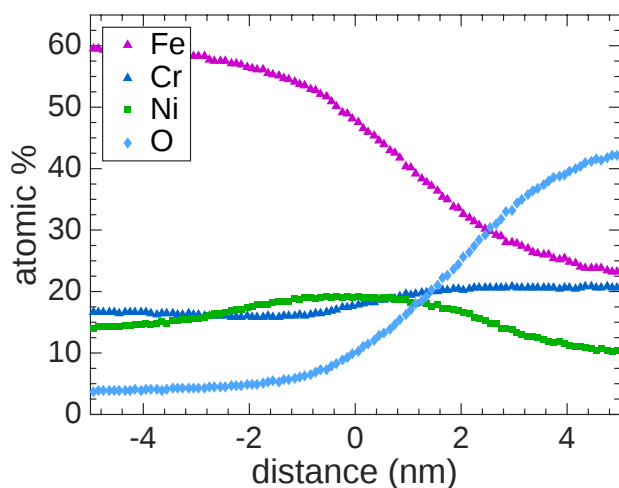


Figure 57
Proxigram of the oxide-metal interface in Figure 56.

In Figure 58, an example of an oxide-metal interface in the material irradiated to 50 dpa is shown. Inside the oxide, Ni-rich metallic precipitates were found. The proxigram of these can be seen in Figure 59. Close to the metal, small fractures took place during analysis (explaining the somewhat irregular shape in the oxide) and thus, the exact distance from the metal to the Ni-rich particles is unknown (likely <100 nm). Interesting to observe in Figure 58 is that O is present, as small particles, inside the metal. This analysis is the only case where many oxide particles were observed in the metal. The total concentration of O in the metal is decreasing, from 2.4 at.% close to the oxide interface to 1.2 at.% in the end of the analysis (around 150 nm from the interface).

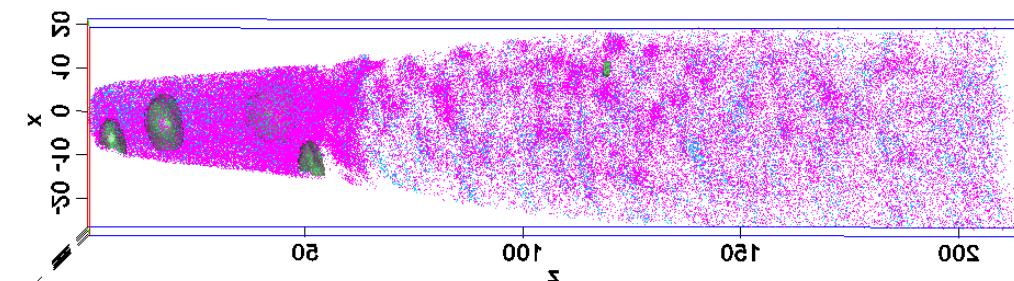


Figure 58
Oxide with Ni-rich particles and the oxide-metal interface in the material irradiated to 50 dpa. CrO ions are shown in magenta, O in blue. Green surfaces are 35 at.% Ni.

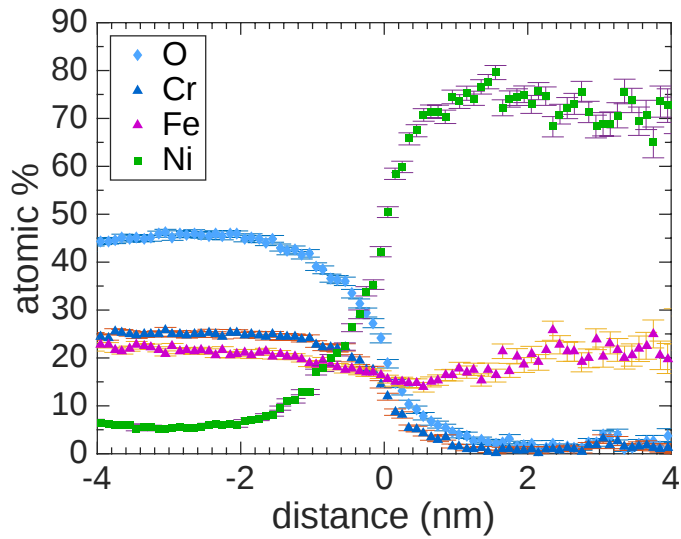


Figure 59
Proxigram for the Ni-rich particles in Figure 58.

In the material irradiated to 100 dpa, the oxide-metal interface was captured in two analyses. The first one, which was a very short run with somewhat uneven evaporation, can be seen in Figure 60. The analysis is from a volume into or very close to a grain boundary in the metal. The corresponding proxigram is shown in Figure 61.

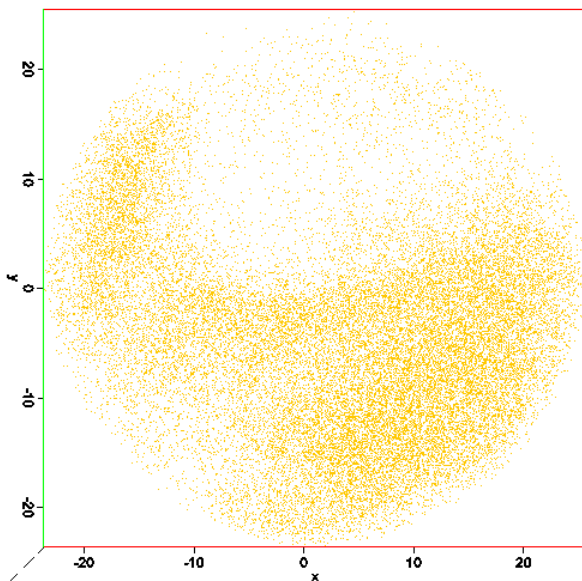


Figure 60
Oxide and metal (seen as holes in oxide) in the material irradiated to 100 dpa. CrO ions are shown in yellow. The analyzed volume is viewed parallel to the sample axis, as the run was very short.

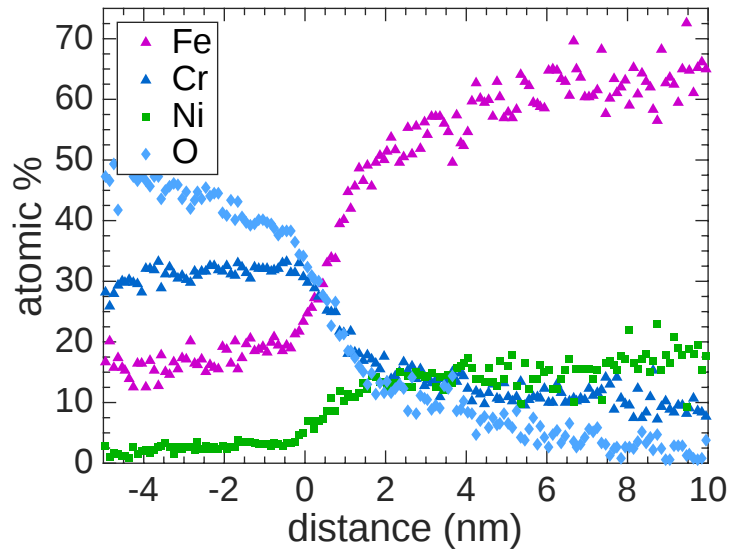


Figure 61
Proxigram of the interface in Figure 60, metal/oxide interface.

Another analysis of the material irradiated to 100 dpa can be seen in Figure 62. The analysis is into or close to an oxidized grain boundary. The composition of the oxide is uncertain as the oxide volume is small and the interface is diffuse due to the evaporation process during APT analysis. Some oxide appears inside the metal, but in a more uneven way than in Figure 58, and it is possible that this is the uneven oxide/metal boundary rather than oxide particles in the metal.

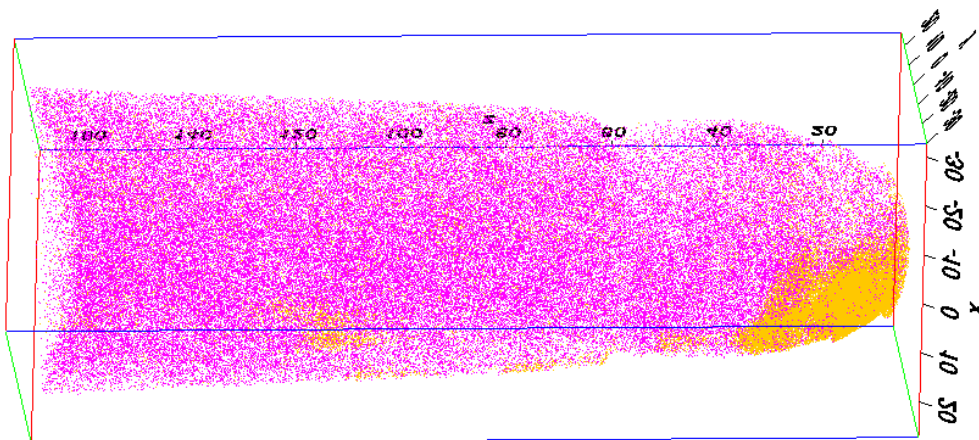


Figure 62
Metal and oxide in the material irradiated to 100 dpa. Fe atoms are shown in pink, orange is CrO ions.

7. Discussion

Examination of oxide films at three different dose levels, formed during operation in Ringhals 2, shows that they are largely similar in terms of film thickness, as well as elemental and phase compositions. The duplex layer structure and other aspects of the oxide films were consistent with other observations of oxides formed on FTTs [34], and they were not very different from what is known for stainless steel corroded under similar water coolant conditions, but without irradiation [23]. In addition, the inner oxide of the sample at 0 dpa examined in this study, and the oxide formed without irradiation [23], consisted of bright and dark phases, although the compositions of these phases differed between the two oxide films. It was confirmed by electron diffraction tilt experiments that the inner oxide layer grew epitaxially on the metal and that film thickness was not affected by irradiation. The observations made in this study suggest that the differences in oxidation behavior between samples exposed for 24 hours to water with and without irradiation [9-11], or between irradiated and unirradiated samples exposed to PWR primary coolant [12], do not persist after several decades of operation in a PWR core.

Even though the oxide film characteristics among the three dose levels examined were similar, the corrosion rates can be different [35, 36]. However, the results of dimensional measurements of flux thimble tubes do not suggest the corrosion rates at the locations investigated in this study are significantly different, i.e., dimensional variations (resolution $\sim 1 \mu\text{m}$) do not correlate with neutron dose [37, 38].

Oxidized grain boundaries were observed at all three dose levels examined. Although the number and size of these features were not quantified, there appeared to be no difference among the three doses examined. In addition, the composition of the oxide in the penetration of the sample at 50 dpa was not different from the inner oxide on the bare surface, which indicates that the conditions under which the oxides formed were similar at the two locations. However, the oxide composition in the penetration of the sample at 100 dpa varied, with Ni peaking close to the tip of the penetration and Cr being enriched closer to the mouth. This observation is qualitatively consistent with other observations of oxide penetrations/cracks in specimens fabricated from FTTs [13], and stress corrosion cracks in a baffle former bolt [28]. Thomas et al. also noted a large variability in oxide composition at crack tips, where in some cases Ni was enhanced near the tip, while the composition was uniform in others [28]. This observation might explain why Ni was elevated only in the oxide penetration of the sample at 100 dpa. Other work indicates that the basic mechanism for grain boundary oxidation is not changed due to irradiation up to 73 dpa [13].

In the irradiated samples, regions elevated in Ni were observed immediately ahead of the oxidized grain boundary. Similar observations were made at oxide penetrations/cracks in specimens fabricated from FTTs [13], and at cracks in a baffle former bolt, although Ni was not enriched ahead of all cracks examined [28]. Fukumura et al. noted that there appeared to be no correlation between tensile stress and grain boundary oxidation depth [13]. The observations made in this study show that oxide penetrations along grain boundaries can form on stainless steel surfaces exposed to PWR primary water, and that irradiation is not a necessary condition for these features to form. Considering the material heterogeneity and the tiny volumes examined, the observations made on the three TEM lamellae are too few to draw a more general conclusion. Additional examination of

oxide penetrations of all three dose levels would be needed to better understand the effects of irradiation on the oxide penetrations. It is possible the oxide penetrations could act as locations for initiation of SCC if they were to be subjected to tensile stress.

Tiny spots in the inner oxide layer near the metal/oxide interface were observed in the irradiated samples only. These features were circular in shape with a diameter of 10~20 nm, but the origin of the phase contrast was not determined. The EDS measurements did not detect any compositional difference between the spots and the surrounding oxide, and this is probably because the volume of a spot is very small relative to the total oxide volume hit by the electron beam. Thus, the spots observed by TEM may or may not be different from the Ni-rich metallic precipitates observed in the oxide by APT (Figure 58). Other studies focusing on the oxides formed on stainless steels under irradiation have not used APT, which might explain why Ni-rich metallic particles in the oxide have not been observed previously. Analyses of additional samples would be needed to determine the size distribution and density of these features as a function of dose.

The APT analyses detected oxide particles in the metal close to the oxidized surface. The concentration of oxygen was the highest at the metal/oxide interface and it decreased with distance from the interface. It has been suggested that the inner oxide layer grows inward by solid diffusion of O^{2-} anions to the metal, and solid diffusion of Fe^{2+} cations from the metal through the inner layer [34], which is consistent with the oxide particles observed in this study. However, as this observation was limited to one sample (50 dpa), analysis of additional samples would be needed to confirm that it is not an isolated observation. In this context, it should be noted that the corrosion front is not uniform, and higher corrosion rates will occur at locations in the metal grain where the corrosion resistance is lower. Sometimes the corrosion attack becomes deep locally, giving the impression that some metal grains were inside the oxide layer and remained as unoxidized metal grains. Clusters or precipitates rich in Ni-Si, presumably γ' (Ni_3Si) or precursors to this phase, were observed in the metal of the irradiated samples by APT analysis. Unsuccessful attempts to image this phase by TEM were made; see discussion in Section 5.4. However, compositional variations adjacent to grain boundaries were consistent with γ' precipitation (Section 5.3). It was noted from the APT analyses that the number density of clusters was lower at the grain boundary, which is in line with other observations on highly irradiated Type 316, although in this case the grain boundary was free of clusters [39]. Manganese was present in some of the precipitates, while this element was absent in others. Segregation of Cu and P to some precipitates was noted. Solute clusters rich in Ni and Si, sometimes together with other elements such as Mn, P and Cu, have been observed by APT analyses in irradiated Types 304, 304L, 316 and 316L [e.g., 39 and 40]. Fujii and Fukaya [39] found that most clusters formed in a Type 316 from a flux thimble tube at 74 dpa had a diameter smaller than 5 nm, with an average of about 4 nm. The clusters larger than 5 nm (max 11 nm) were of two types that either contained or did not contain Mn. The authors proposed that the Mn containing clusters were precursors to G phase ($M_6N_{16}Si_7$, $M=Mn, Mo$) precipitates where the formation of this phase was related to a thermally activated process and not radiation-induced.

The Ni/Si ratios of the clusters ranged from 1.2 to 2.0 in the 50 dpa sample and from 2.2 to 2.5 in the sample at 100 dpa. Chou et al. found that the Ni/Si ratio for Types 304 and 304L decreased with dose from 6 to 3 for doses in the range 3.6 to 13 dpa [40]. The Ni/Si ratio of the Type 316 at 74 dpa was 2.0 for all types of clusters observed [39]. The latter results were based on analysis of a large number of clusters, and because the number of clusters observed in this study was much smaller, it is possible the difference between the

two dose levels examined in this study would diminish by the observation of a larger number of Ni/Si clusters.

The cluster dimensions observed in the present study (2-8 nm in diameter with most being 4-5 nm) were similar to those reported in [39]. The number density of these features varied from $0.7 \cdot 10^{23}$ to $1.2 \cdot 10^{23} \text{ m}^{-3}$ with no systematic difference between the two dose levels examined. Chou et al. found that the number density of the clusters increased with dose from $1.8 \cdot 10^{22} \text{ m}^{-3}$ to $1.8 \cdot 10^{23} \text{ m}^{-3}$ for doses in the range 3.6 to 13 dpa [40], while the number density of all clusters in the Type 316 analyzed by Fujii and Fukuya [39] was $7.7 \cdot 10^{23} \text{ m}^{-3}$. The latter value is clearly higher than observed in this study. It is noted that the bulk Si content of the Type 316 examined in this study was 0.43 wt. %, while it was 44% higher (0.62 wt. %) in the material in [39]. The difference in bulk Si content might to some extent explain the lower number density of cluster observed in this study. However, as concluded in [40], the composition of the Ni/Si clusters also depends on irradiation parameters such as fluence, flux and temperature; the irradiation temperature of the Type 316 at 74 dpa was 305 °C, whereas it was 315 and 324 °C for the materials of this study. In addition, different methods for evaluating cluster size and density might also have contributed to the differences observed; the maximum separation method was used for size in this study as well as the one by Fujii and Fukuya [39], while the number density in this study was quantified using iso-concentration surfaces.

As expected, radiation induced segregation was observed in the two irradiated conditions examined. Grain boundary enrichment of Ni and Si and depletion of Mo and Cr was observed by TEM, and segregation of these elements was confirmed in the APT analysis for the 100 dpa condition. The latter technique also detected enrichment of boron adjacent to the grain boundary. These observations are in general consistent with other studies, both in terms of the elements segregated and the magnitude of segregation [26-29, 39].

There was no difference in the Frank loop density and size distribution between the two dose levels examined in this study. This is consistent with other studies that show that the Frank Loop density [31, 41, 42] and microstructure [24, 31, 41-43] reach steady state after a few dpa (<1-10). However, compared to other data [42, 43], the Frank loop density is on the low side, while the average loop diameter agrees well with literature data [32].

As reported in Section 5.5, cavities were observed in the irradiated conditions. It was found that the number density of cavities increased with dose, but that their size remained unchanged. This is consistent with observations made by others on irradiated cold worked Type 316 SS from thimble tubes [27, 32, 44, 45]. In all these cases the cavity diameter was less than 2 nm, although Edwards found a small fraction of cavities to extend up to 3 nm in diameter [32]. The cavities observed can be either voids or gas-filled bubbles. Because of the transmutation reactions, and the high dose levels in this study, it is possible that the cavities observed are He (and H?) bubbles. The He and H contents were not measured in this study; however, He was reported to increase from 12 to 486 appm for doses in the range ~1 to 53 dpa [44], while it was 208 appm in a material at 35 dpa [45].

Data on the cavity number density determined in this study are compared with literature data in Figure 63. As expected, very few cavities form at low neutron dose (< 1 dpa). At doses in the range 3 to 73 dpa, the scatter is large among different investigations, and the number density range from $0.6 \cdot 10^{23}$ to $9.4 \cdot 10^{23} \text{ m}^{-3}$. It is also hard to see any general trend in the data. While Edwards et. al observed clearly lower total values compared to the other studies, their cavity density more than doubled from 33 to 70 dpa. This is in contrast

with Fujimoto's data that indicate essentially no change with dose. The cavities are difficult to resolve with the sample in focus, while an under-focused image leads to apparent larger cavity size, and operator-related differences in interpretation of the images might be a cause for the scatter observed in Figure 63. Another cause for the scatter, especially at lower dose, could be differences in the thermal to fast neutron flux ratio; He is generated primarily via reactions with thermal neutrons, while displacement damage is caused by fast neutrons, so different thermal to fast neutron flux ratios will result in different He/dpa rates [44, 46, 47]. Variations in the initial boron content of the materials can also explain some of the variation at low dose [46].

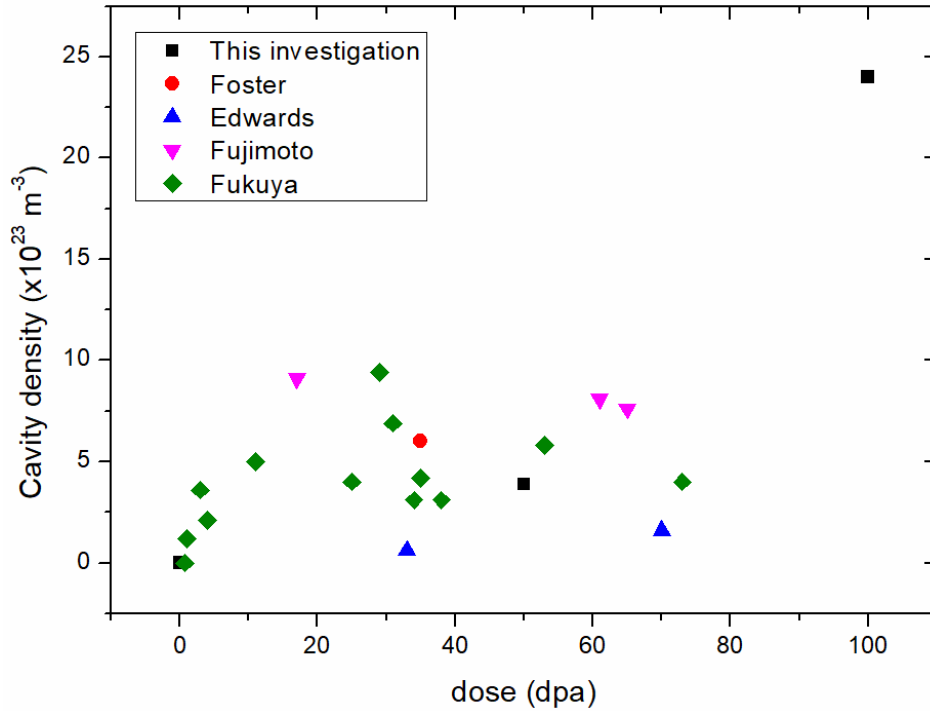


Figure 63 Cavity density as a function of dose for cold worked Type 316 from flux thimble tubes examined in this study compared with literature data [27, 32, 44, 45].

Figure 63 shows that the cavity density measured in this study for the sample at 50 dpa agrees with literature data, while data for the sample at 100 dpa is clearly higher. However, examination of additional samples to confirm the observation at 100 dpa is recommended, since the value is based on a limited sample volume and the uncertainty is comparatively large.

The cavities can either be bubbles or voids, where the former generally is relatively small and gas pressurized, and the latter is either totally or partially vacuum-filled [47]. Bubbles can serve as nuclei for voids, and He tends to accelerate the onset of void swelling and to increase the cavity density. There are two main reactions for the production of He in austenitic stainless steels. The first is the (n, α) reaction with ^{10}B , a reaction that normally saturates quite fast with the rapid burnout of this isotope [46, 47]. A second, and more important contribution to the He production at higher dose, is the two-step reaction sequence, $^{58}\text{Ni}(n, \gamma) ^{59}\text{Ni}(n, \alpha)$. As the reaction sequence involves the buildup of ^{59}Ni as the first step, it is non-linear and accelerates in production rate with increasing exposure. Thus, it is possible the larger cavity density observed at 100 dpa is a result of a higher He production rate caused by the reactions involving Ni isotopes. However, as noted in the

previous paragraph, examination of additional samples to confirm the observation is recommended. In addition, measurement of the He content in the materials would also be of interest.

The volume fraction of the cavities for the samples at 50 and 100 dpa were, respectively, 0.01-0.23% and 0.12-1.09% if cavity radii between 1 and 2 nm are assumed and the densities, including uncertainty, reported in Section 5.5 are used. The range of values for the sample at 100 dpa is clearly above the volume fraction of 0.036% at 35 dpa reported by Foster et al. [45], and the 0.015 to 0.042% observed by Fujii et al. [44] for doses ranging from 3 to 53 dpa. Based on the observations made on material at 35 dpa, it was predicted swelling would not exceed 3% at 100 dpa and an irradiation temperature in the range 300-400 °C [45]. Model predictions by Fujii et al. yielded a much lower amount of swelling (<0.2%) for a thimble tube irradiated to 100 dpa at 290-320 °C [44]. As mentioned in the previous paragraph, confirmatory measurements of the cavity density and He content are recommended. The information can be used to improve the predicting capability of existing models.

7.1. Recommendations for Further Studies

The results of this study have gained valuable insight regarding the effects of neutron irradiation to very high doses on the microstructure and oxidation in primary PWR water of austenitic stainless steel. To confirm some of the results of this study over the full range of dose, and to determine if they are general and not isolated observations, a few areas for further study have been identified:

- Examine additional oxide penetrations to confirm the observations of the present study and to better understand the effects of irradiation on these features;
- Examine additional TEM lamellae to determine if the spots observed in the inner oxide layer are equal to the Ni-rich metallic particles detected by APT;
- Oxide particles in the metal near the oxide were detected by APT in one sample. Additional samples need to be analyzed to confirm this observation;
- Confirm the cavity density measurement of the 100 dpa sample and measure the helium contents of the three dose levels examined in this study;
- Analyze the grain boundary composition of all dose levels by APT.

8. Conclusions

The oxides formed on stainless steel exposed in the core region of a PWR consisted of a duplex layer structure, with an outer porous layer of fine spinel grains and an inner dense layer of epitaxially grown spinel. Three dose levels, 0, 50 and 100 dpa were examined and no significant effect of dose was observed on the oxide microstructure. Small spots were observed in the oxide near the metal oxide interface of the irradiated samples. However, it was not possible to confirm any compositional or structural differences of these features from the surrounding oxide. In addition, the presence of Ni rich metallic particles in the oxide was detected by atom probe tomography.

The TEM lamellae of all three dose levels had one or two oxide penetrations along metal/metal grain boundaries. There were no differences in size or density of this feature among the dose levels examined, although additional examinations would be needed to verify this statement statistically. However, regions elevated in Ni were observed immediately ahead of the oxide penetrations in the irradiated samples.

Clusters or precipitates rich in Ni-Si, presumably γ' (Ni_3Si), sometimes including Mn, Cu and P, were observed in the metal of the irradiated samples. A lower cluster density was observed at grain boundaries. There was no effect of dose on the cluster size and density. The cluster size observed in this study was in agreement with literature data, while the number density was lower. Bulk silicon content, irradiation parameters such as fluence, flux and temperature, as well as differences in data evaluation are factors that can contribute to the differences observed.

The microstructure of the irradiated metal was consistent with observations reported in the open literature. Radiation induced segregation with depletion of Cr and enrichment of Ni and Si was observed in the irradiated conditions.

Cavities were observed in the irradiated samples. The number density of this feature in the sample at 50 dpa agreed with the range reported in the literature, whereas the density at 100 dpa clearly was higher. Additional examinations are suggested to confirm the observation and to determine if any dimensional changes have occurred.

9. References

1. S. M. Bruemmer, New Issues Concerning Radiation-Induced Material Changes and Irradiation-Assisted Stress Corrosion Cracking in Light-Water Reactors. Proc. 10th Int'l. Symp. on Environmental Degradation of Materials in Nuclear Power Systems – Water Reactors, NACE, Houston, TX (2002) (CD ROM).
2. G. S. Was, Recent Developments in Understanding Irradiation Assisted Stress Corrosion Cracking. Proc. 11th Int. Conf. on Environmental Degradation of Materials in Nuclear Power Systems – Water Reactors, American Nuclear Society, La Grange Park, IL, (2003), p. 965, CD-ROM.
3. Anders Jenssen, Lars G. Ljungberg, Irradiation Assisted Stress Corrosion Cracking. Postirradiation CERT Tests of Stainless Steels in a BWR Test Loop, 7th Int'l Symp. on Environmental Degradation of Materials in Nuclear Power Systems - Water Reactors, Breckenridge, CO, August 6-10, 1995.
4. A. Jenssen, R. Pathania, R. Carter, Crack Growth in Irradiated Austenitic Stainless Steels in BWR Environments, Fontevraud 8 - Contribution of Materials Investigations and Operating Experience to LWRs' Safety, Performance and Reliability, Avignon, France, September 14-18, 2014.
5. J. L. Nelson, P. L. Andresen, Review of Current Research and Understanding of Irradiation-Assisted Stress Corrosion Cracking, Proc. 5th Int'l. Symp. on Environmental Degradation of Materials in Nuclear Power Systems – Water Reactors, American Nuclear Society, La Grange Park, IL, (1991), p. 10.
6. Final Review of the Cooperative Irradiation-Assisted Stress Corrosion Cracking Research Program. EPRI, Palo Alto, CA, 2010. 1020986.
7. J. Walmsley, P. Spellward, S. Fisher, A. Jenssen, Microstructural Characterisation of Grain Boundaries in Irradiated Steels, 7th Int'l Symp. on Environmental Degradation of Materials in Nuclear Power Systems - Water Reactors, Breckenridge, CO, August 6-10, 1995.
8. S. M. Bruemmer, L. E. Thomas. High-Resolution Characterization of Stress Corrosion Crack Tips in Stainless Steel Core Internals. Presented at Int'l Symp. on Contribution of Materials Investigation to the Resolution of Problems Encountered in Pressurized Water Reactors, Fontevraud 6, September 2006, SFEN, Paris, France.
9. S. S. Raiman, P. Wang, G. S. Was. The Effect of In-Situ Proton Irradiation on the Corrosion of 316L Stainless Steel. Proc. 16th Int. Conf. on Environmental Degradation of Materials in Nuclear Power Systems – Water Reactors, Asheville, NC, August, 2013.
10. S. S. Raiman, P. Wang, G. S. Was, Irradiation Accelerated Corrosion of Stainless Steel, Fontevraud 8 - Contribution of Materials Investigations and Operating Experience to LWRs' Safety, Performance and Reliability, Avignon, France, September 14-18.

11. S. S. Raiman, G. S. Was. Composition and Morphology of the Oxide Film Formed on 316L Stainless Steel During In-Situ Proton Irradiation in PWR Conditions, 17th Int. Conf. on Environmental Degradation of Materials in Nuclear Power Systems – Water Reactors, August 9-13, 2015, Ottawa, Ontario, Canada.
12. M. Boisson, L. Legras, F. Carrette, O. Wendling, T. Sauvage, A. Bellamy, P. Desgardin, L. Laffont, A. Andrieu, Comparative Study on Short Time Oxidation of Un-Irradiated and Protons Pre-Irradiated 316L Stainless Steel in Simulated PWR Water, 18th Int. Conf. on Environmental Degradation of Materials in Nuclear Power Systems – Water Reactors, Portland, OR, August 13-17, 2017, p. 899.
13. T. Fukumura, K. Fukuya, K. Fujii, T. Miura, Y. Kitsunai, Grain Boundary Oxidation of Neutron Irradiated Stainless Steels in Simulated PWR Water, 18th Int. Conf. on Environmental Degradation of Materials in Nuclear Power Systems – Water Reactors, Portland, OR, August 13-17, 2017, p. 937.
14. T. Shoji. Materials Ageing Degradation Programme in Japan and Proactive Ageing Management in NPP. Presented at the Materials Innovation for Nuclear Optimized Systems (MINOS) Workshop, CEA-INSTN, Saclay, France, December 5-7, 2012.
15. Y.-J. Kim. Analysis of oxide film formed on Type 304 stainless steel in 288 °C water containing oxygen, hydrogen, and hydrogen peroxide. Corrosion – Vol. 55, No. 1 (1999), pp. 81-88.
16. G. Wikmark. Study of the reactions of oxygen and hydrogen peroxide on stainless steel in high temperature water with electrochemical impedance spectroscopy. Proc. 1991 JAIF Int’l Conf. On Water Chemistry in Nuclear Power Plants, Japan Atomic Industrial Forum, Tokyo, 1991, pp. 335-342.
17. P. D. Freyer, T. R. Mager and M. A. Burke, “Hot Cell Crack Initiation Testing of Various Heats of Highly Irradiated 316 Stainless Steel Components Obtained from Three Commercial PWRs”, 13th Int’l Conf. on Environmental Degradation of Materials in Nuclear Power Systems, Whistler, B.C., Canada (August 2007).
18. A. Jenssen, P. Efsing, B. Forssgren, B. Bengtsson and M. Molin. Examination of Highly Irradiated Stainless Steels from BWR and PWR Reactor Pressure Vessel Internals. Proc. Int’l Symp. on Contribution of Materials Investigations to Improve the Safety and Performance of LWRs, Fontevraud 7, Avignon, France, September 2010.
19. A. Jenssen, Jäternäs, D. Examination of a Highly Irradiated Flux Thimble Tube from Ringhals 2, Studsvik Nuclear AB, Sweden: 2010. STUDSVIK/N-10/129 rev. 1.
20. Materials Reliability Program: Characterizations of Type 316 Cold Worked Stainless Steel Highly Irradiated Under PWR Operating Conditions (International IASCC Advisory Committee Phase 3 Program Final Report)

- (MRP-214). EPRI, Palo Alto, CA and the International IASCC Advisory Committee: 2007. 1015332.
21. Private communication from J. Roudén (Ringhals AB) to A. Jenssen (Studsvik Nuclear AB), October 28, 2015.
 22. Rapid Simulation of Irradiation Damage on Austenitic Stainless Steel: Mechanical Testing and Specimen Preparation. EPRI, Palo Alto, CA: 2017. 10004697.
 23. Chen. J. and Fager, C. Understanding the effects of zinc injection, coolant pH and temperature on radioactivity buildup on stainless steels – An advanced structural examination, Studsvik Nuclear AB, Sweden: 2016, STUDSVIK/N-15/203, 2016-01-11.
 24. D. Edwards, E. Simonen, S. Bruemmer, P. Efsing. Microstructural Evolution in Neutron-Irradiated Stainless Steel: Comparison of LWR and Fast-Reactor Irradiations. Proceedings of the 12th International Conference on Environmental Degradation of Materials in Nuclear Power System – Water reactors, Snowbird, UT (August 2005).
 25. K. Fukuya, K. Fujii, H. Nishioka, Y. Kitsunai. Evolution of Microstructure and Microchemistry in Cold-Worked 316 SS under PWR Irradiation. J. Nucl. Sci. Technol. 43(2) (2006) 159-173.
 26. A. Jenssen, L. G. Ljungberg, J. Walmsley, S. Fisher, The Importance of Molybdenum on Irradiation Assisted Stress Corrosion Cracking, Corrosion, Vol. 54, No. 1, January 1998, p. 48.
 27. K. Fujimoto, T. Yonezawa, E. Wachi, Y. Yamaguchi, M. Nakano, R.P. Shogan, J.P. Massoud, T.R. Mager. Effect of the Accelerated Irradiation and Hydrogen/Helium Gas on IASCC Characteristics for Highly Irradiated Austenitic Stainless Steel. Proceedings of the 12th International Conference on Environmental Degradation of Materials in Nuclear Power System – Water reactors, Snowbird, UT (August 2005).
 28. Analytical Transmission Electron Microscopy (ATEM) Characterization of Stress-Corrosion Cracks in LWR-Irradiated Austenitic Stainless Steel Core Components – Revision 2, EPRI, Palo Alto, CA: 2006. 1014511.
 29. The Use of Proton Irradiation to Determine IASCC Mechanisms in Light Water Reactor: Solute Addition Alloys, EPRI, Palo Alto, CA: 2003. 1007440.
 30. W. Karlsen, M. Ivanchenko, J. Pakarinen, T. Karlsen. TEM Examination of the Effect of Post-Irradiation Annealing on 7.7 dpa AISI 304 Stainless Steel, Proc. Int'l Symp. on Contribution of Materials Investigations to Improve the Safety and Performance of LWRs, Fontevraud 8, SFEN, Avignon, France, September 2014.
 31. S. J. Zinkle, P.J. Maziasz, R.E. Stoller. Dose dependence of the microstructural evolution in neutron-irradiated austenitic stainless steel. J. Nucl. Mater. 206 (1993), pp. 266-286.

32. D.J. Edwards, F.A. Garner, S.M. Bruemmer, Pål Efsing. Nano-cavities observed in a 316SS PWR flux thimble tube irradiated to 33 and 70 dpa, *Journal of Nuclear Materials* 384 (2009) 249–255.
33. J.M. Hyde, C.A. English, An Analysis of the Structure of Irradiation Induced Cu-enriched Clusters in Low and High Nickel Welds, *Materials Research Society Symposium*, 2000, pp. R6.6.1-R6.6.12. Boston.
34. K. Fukuya, H. Nishioka, K. Fujii, Y. Kitsunai, Characterization of Surface Oxides Formed on Irradiated Stainless Steels in Simulated PWR Primary Water, *Proc. Int'l Symp. on Contribution of Materials Investigations to Improve the Safety and Performance of LWRs*, Fontevraud 8, SFEN, Avignon, France, September 2014.
35. J. Chen, C. Obitz, H. Arwin and B. Forssgren, Corrosion Kinetics of Nickel-Base Alloys with High Chromium Contents under Simulated BWR Normal Water Chemistry Conditions and High Flow Velocity, 17th International Conference on Environmental Degradation of Materials in Nuclear Power Systems – Water Reactors, August 9-13, 2015, Ottawa, Ontario, Canada.
36. J. Chen, A. Jenssen, F. Lindberg, P. Ekström and P. Efsing, Effect of Neutron Irradiation on the Microstructures of Oxide Films formed on Corroded Austenite Stainless Steel in PWR, *Proc. Int'l Symp. on Contribution of Materials Investigations to Improve the Safety and Performance of LWRs*, Fontevraud 9, SFEN, Avignon, France, September 2018.
37. A. Micski, Examination of a Thimble Tube Irradiated in Ringhals 2 for 23 years, Studsvik Nuclear AB, Sweden: 1999, STUDSVIK/N(H)-99/72, 1999-12-09.
38. U. Engman, Examination of two highly irradiated Flux Thimble Tubes from Ringhals 4, Studsvik Nuclear AB, Sweden: 2014, STUDSVIK/N-14/314, 2014-09-09.
39. K. Fujii, K. Fukuya, Irradiation-Induced Microchemical Changes in Highly Irradiated 316 Stainless Steel, *Journal of Nuclear Materials* 469 (2016), pp. 82-88.
40. P. Chou, N. Soneda, K. Nishida, K. Dohi, E. A. Marquis, Y. Chen, Microstructure and Fracture Toughness of Irradiated Stainless Steel Retrieved from the Field: the Potential Role of Radiation-Induced Clusters, *Proc. Int'l Symp. on Contribution of Materials Investigations to Improve the Safety and Performance of LWRs*, Fontevraud 8, SFEN, Avignon, France, September 2014.
41. C. J. Ulmer, A. T. Motta, Characterization of Faulted Dislocation Loops and Cavities in Ion Irradiated Alloy 800H. *J. Nucl. Mater.* 498 (2018) 458-467.
42. K. Fukuya, Current Understanding of Radiation-Induced Degradation in Light Water Reactor Structural Materials, *Journal of Nuclear Science and Technology*, Volume 50, No. 3, March 2013.

43. D. Edwards, E. Simonen, S. Bruemmer, P. Efsing, Comparison of Microstructural Evolution in LWR and Fast-Reactor Irradiation of AISI 304 and 316 Stainless Steel. Fontevraud 6, September 2006, SFEN, Paris, France.
44. K. Fujii, K. Fukuya, G. Furutani, T. Torimaru, A. Kohyama, Y. Katoh, Swelling in 316 Stainless Steel Irradiated to 53 dpa in a PWR, Proc. 10th international conference on environmental degradation of materials in nuclear power system – Water reactors, The minerals, metal and material society, PA, August 2001.
45. J.P. Foster, D.L. Porter, D.L. Harrod, T.R. Mager, M.G. Burke, 316 stainless steel cavity swelling in a PWR. *J. Nucl. Mater.* 224 (1995) 207-215.
46. F. A. Garner, B. M. Oliver, L. R. Greenwood, D. J. Edwards, S.M. Bruemmer, M. L. Grossbeck, Generation and Retention of Helium and Hydrogen in Austenitic Steels Irradiated in a Variety of LWR and Test Reactor Spectral Environments, Proc. 10th international conference on environmental degradation of materials in nuclear power system – Water reactors, The minerals, metal and material society, PA, August 2001.
47. F.A. Garner. Radiation damage in Austenitic steels. In: Konings R.J.M., (ed.), *Comprehensive Nuclear Materials*, Vol. 4 (2012), pp. 33-95, Amsterdam: Elsevier.

Appendix A – APT Analyses of Grain Boundaries in Material at 100 dpa

Results from analysis of one grain boundary are shown in Section 6.2.2 of the report, whereas data from APT analyses of two other grain boundaries are given here. Grain boundary 1 is shown in Figure A.1, with associated compositional profiles presented in Figure A.2. Figure A.3 shows Grain boundary 2, while Figure A.4 shows the compositional profiles. The elemental profiles related to Co and Cu are probably NiH, as they overlap in the spectrum. The statistics of the data for the two grain boundaries presented here are inferior to the results shown in Section 6.2.2 of the report. This is because smaller parts of the grain boundaries presented in this appendix are covered by the analyses. These grain boundaries are also from locations further away from the oxide.

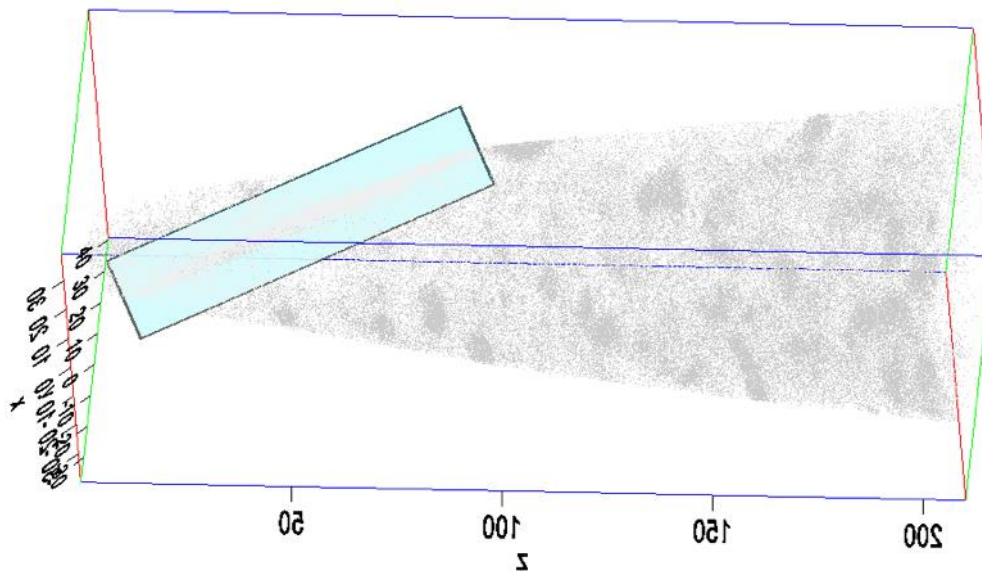


Figure A.1

Grain boundary 1 in material irradiated to 100 dpa. The box marks the volume used for composition profiles. Si atoms are shown in grey.

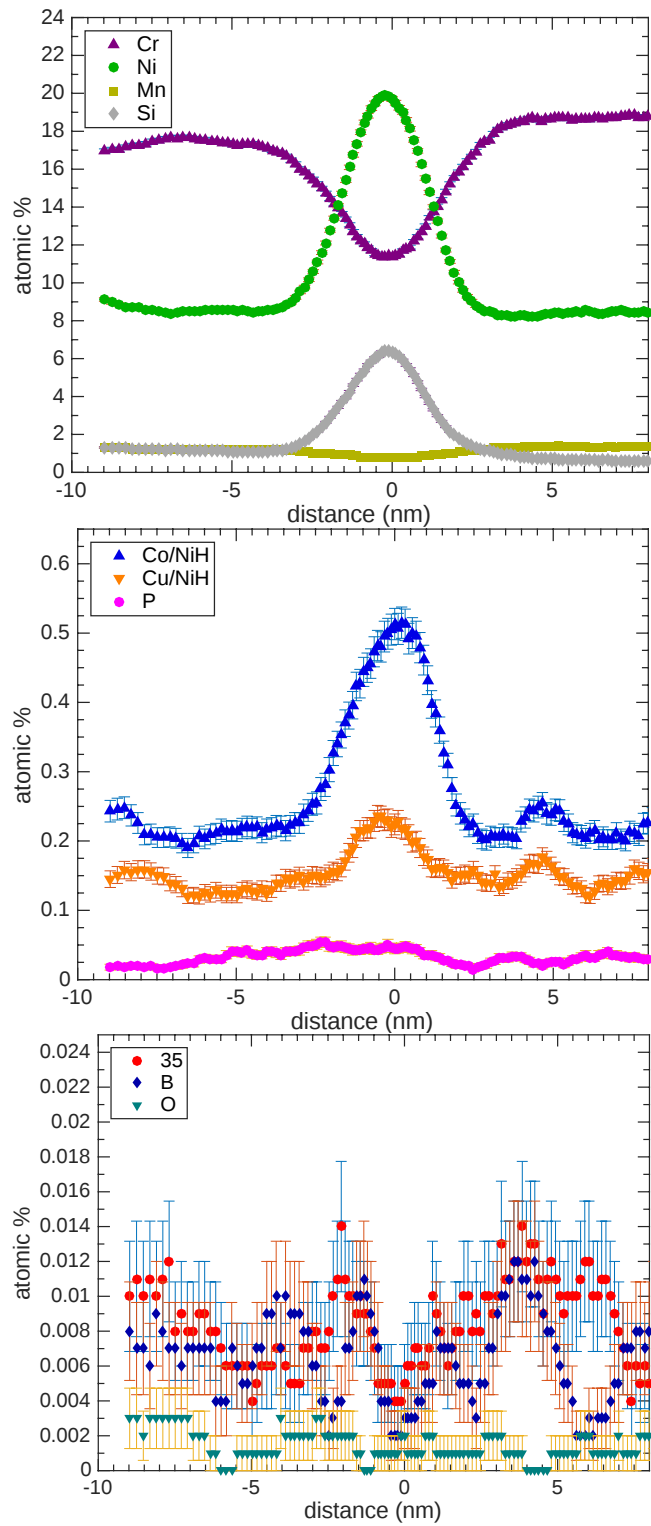


Figure A.2
Compositional profiles of some of the elements in the grain boundary shown in Figure A.1.

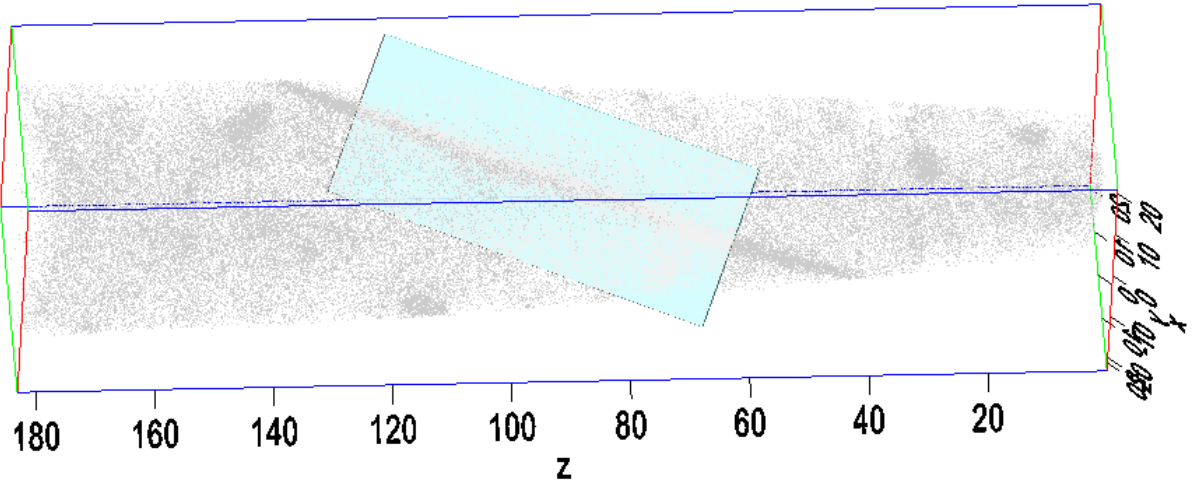


Figure A.3

Grain boundary 2 in material irradiated to 100 dpa. The box marks the volume used for composition profiles. Si atoms are shown in grey.

Figure A.5 shows a selected portion of the spectrum. The peak at 24 matches C_{2+} (red thin line) better than Ti^{++} (blue thin line). At the mass-to-charge ratio of the other Ti^{++} isotopes, there is only background.

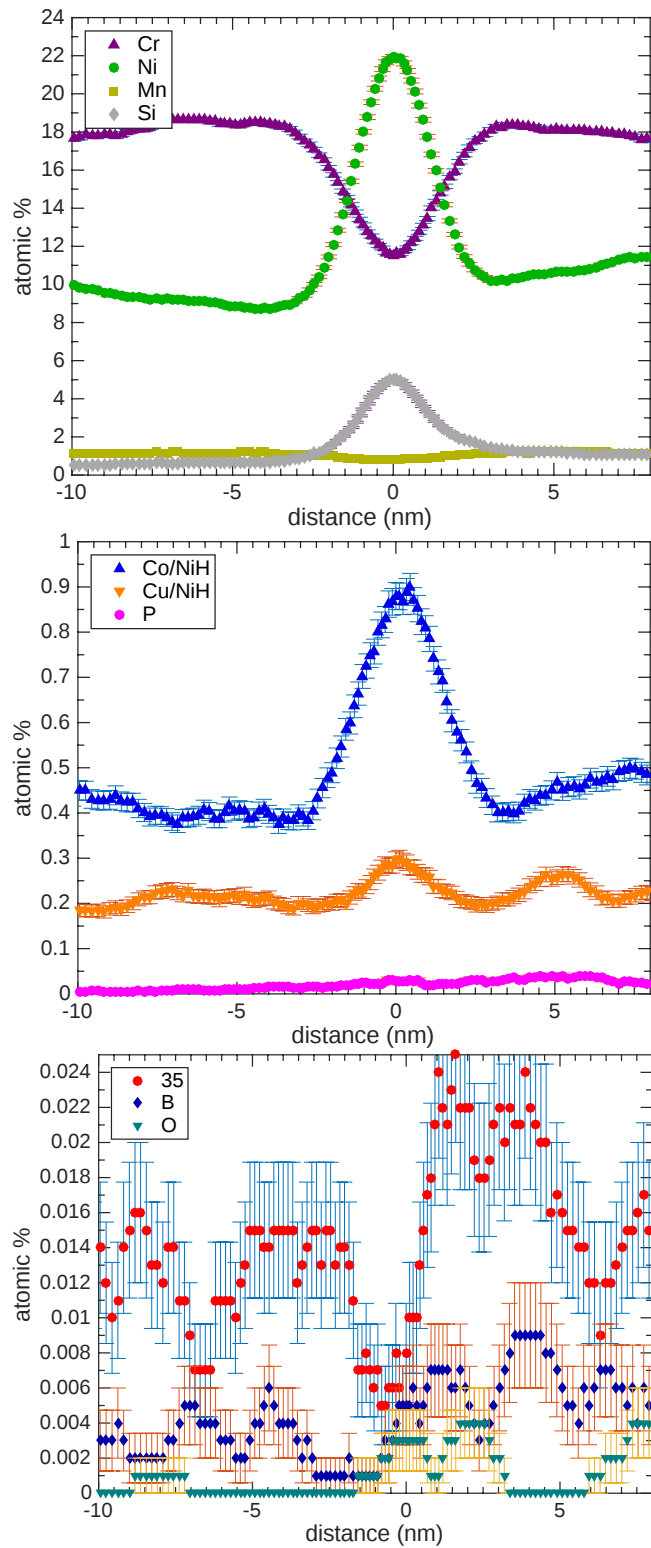


Figure A.4
Compositional profiles of some of the elements in the grain boundary shown in Figure A.3.

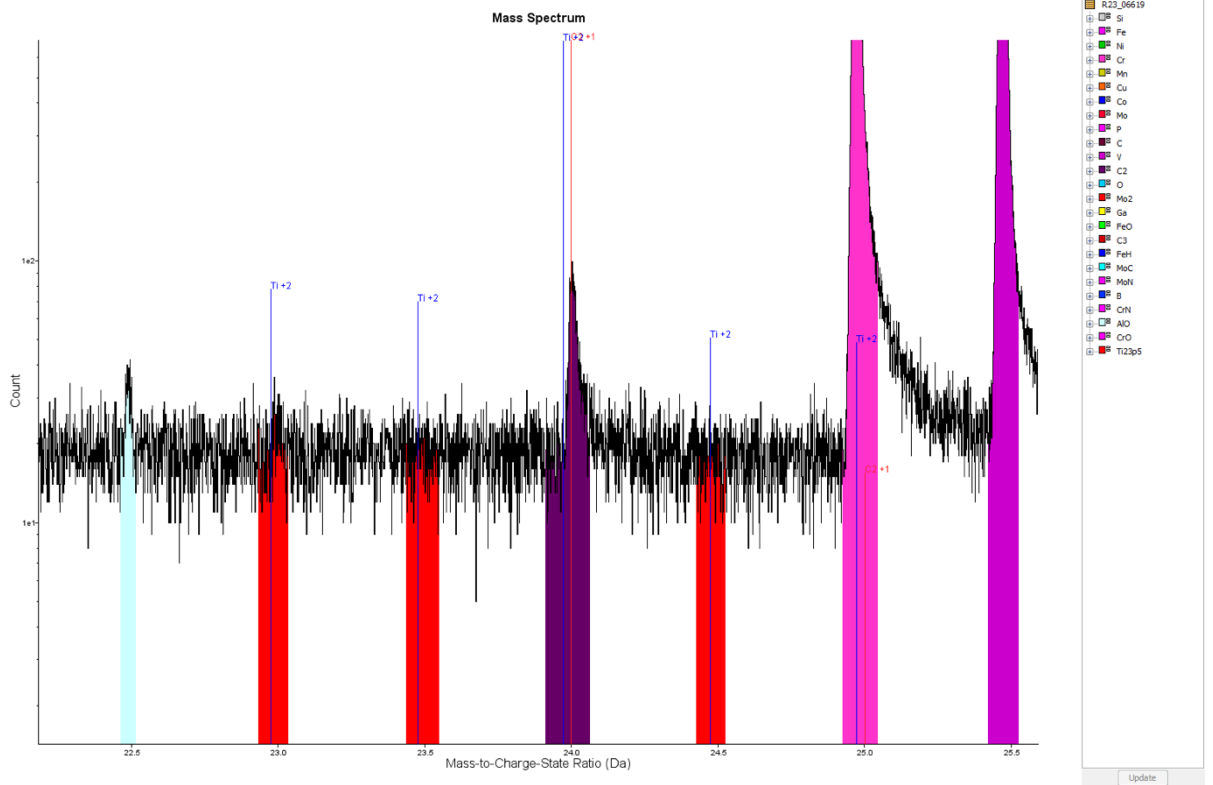


Figure A.5
A selected portion of the spectrum showing the location of the Ti/C₂ peaks.

The Swedish Radiation Safety Authority has a comprehensive responsibility to ensure that society is safe from the effects of radiation. The Authority works from the effects of radiation. The Authority works to achieve radiation safety in a number of areas: nuclear power, medical care as well as commercial products and services. The Authority also works to achieve protection from natural radiation and to increase the level of radiation safety internationally.

The Swedish Radiation Safety Authority works proactively and preventively to protect people and the environment from the harmful effects of radiation, now and in the future. The Authority issues regulations and supervises compliance, while also supporting research, providing training and information, and issuing advice. Often, activities involving radiation require licences issued by the Authority. The Swedish Radiation Safety Authority maintains emergency preparedness around the clock with the aim of limiting the aftermath of radiation accidents and the unintentional spreading of radioactive substances. The Authority participates in international co-operation in order to promote radiation safety and finances projects aiming to raise the level of radiation safety in certain Eastern European countries.

The Authority reports to the Ministry of the Environment and has around 300 employees with competencies in the fields of engineering, natural and behavioral sciences, law, economics and communications. We have received quality, environmental and working environment certification.

Publikationer utgivna av Strålsäkerhetsmyndigheten kan laddas ned via stralsakerhetsmyndigheten.se eller beställas genom att skicka e-post till registrator@ssm.se om du vill ha broschyren i alternativt format, som punktskrift eller daisy.

Strålsäkerhetsmyndigheten
Swedish Radiation Safety Authority
SE-171 16 Stockholm
Phone: 08-799 40 00
Web: ssm.se
E-mail: registrator@ssm.se

©Strålsäkerhetsmyndigheten